3D OPTICAL PROFILOMETRY USING FIBER OPTICS LLOYD′S MIRROR METHOD

by

Gülşen Kösoğlu

B.S., Physics, Marmara University, 2007

M.S., Physics, Marmara University, 2010

Submitted to the Institute for Graduate Studies in
Science and Engineering in partial fulfillment of
the requirements for the degree of
Doctor of Philosophy

Graduate Program in Physics
Boğaziçi University
2017

3D OPTICAL PROFILOMETRY USING FIBER OPTICS LLOYD′S MIRROR METHOD

APPROVED BY:

Prof. Mehmet Naci İNCİ (Thesis Supervisor)	....
Prof. Gülen AKTAŞ	....
Prof. Veysi Erkcan ÖZCAN	....
Assistant Prof. Heba YÜKSEL	....
Assistant Prof. Gülşen AKIN EVİNGÜR	....

DATE OF APPROVAL: 20.10.2017

ACKNOWLEDGEMENTS

I would like to thank my advisor Prof. M. Naci İnci for his guidance and contributions to this research. His kind, instructive and encouraging attitude supported my progress as an experimental physicist. I really appreciate being a part of the Photonics Research Group and express my gratitude to my lab partners; Sema Güvenç, Belkıs Gökbulut, Ekrem Yartaşı ve Arda İnanç, who supported me and my research with full of their knowledge and loves.

In addition to all the instructors who have contributed to my experience and knowledge in many areas, I especially thank Prof. Dr. Uğur Yahşi, the head of the physics department, Marmara University, who confirm the permission for my doctorate and thesis studies in Boğaziçi University.

I would also like to thank my mum and dad for all their love and effort not only for my doctorate but also for all my education life. I would like to thank so much to my twin sister dear Gülten and her husband Okay for all their patience, their curiosity in physics and all their love. Finally many thanks to my friends who have supported and endured many difficulties with me throughout my education life.

ABSTRACT

3D OPTICAL PROFILOMETRY USING FIBER OPTICS LLOYD′S MIRROR METHOD

A fiber optic Lloyd's mirror assembly is investigated to obtain various optical interference patterns for the detection of three-dimensional shapes of rigid bodies. Two types of the fiber optic Lloyds systems are used in this work. The first one consists of a single mode optical fiber and a highly reflecting flat mirror to produce bright and dark strips. The second one is constructed by locating a single mode optical fiber in a v-groove, which is formed by two orthogonal flat mirrors to allow the generation of square type interference patterns for the desired applications. The structured light patterns formed by these two fiber optic Lloyds techniques are projected onto three-dimensional objects. Fringe patterns are deformed due to the object′s surface topographies, which are captured by a digital CCD camera and are processed with the following signal processing techniques to accomplish their three-dimensional surface topographic maps: Fourier Transform Profilometry, Phase Stepping Profilometry, and Continuous Wavelet Transform Profilometry. The method is developed for extracting 3D height distribution of various objects at the micron scale with a resolution of 5 μm by elegantly interrogating the first fiber optic assembly to an optical microscope and a CCD camera. It is demonstrated that the proposed technique is quite suitable and practical to produce a structured light pattern with an adjustable frequency. By increasing the distance between the fiber and the mirror with a micrometer stage in the Lloyd′s mirror assembly, the separation between the two bright fringes is lowered down to the micron scale without using any additional elements as part of the optical projection unit. The phase analysis of the acquired image is carried out by One Dimensional Continuous Wavelet Transform.

ÖZET

FİBER OPTİK LLOYD AYNASI YÖNTEMİNİ KULLANARAK 3-D OPTİK PROFİLOMETRE YAPIMI

Fiber optik Llyod ayna düzeneği, çeşitli optik girişim desenleri elde edilerek katı cisimlerin üç boyutlu şekillerini belirlemek için incelenmiştir. Bu çalışmada iki tür fiber optik Lloyd sistemi kullanılmaktadır. Birincisi, aydınlık-karanlık şeritler üretmek için tek-modlu bir optik fiber ve yüksek oranda yansıtıcı bir düzlem aynadan oluşmaktadır. İkincisi, istenilen uygulamalarda kare girişim deseni oluşumuna olanak sağlamak için, birbirine dik iki aynanın oluşturduğu v-oluk içine tek modlu optik fiberin yerleştirilmesi ile oluşturulur. İki tip fiber optik Lloyd tekniği ile elde edilmiş ışık desenleri üç boyutlu cisimlerin üzerine yansıtılır. Nesnelerin yüzey topografyaları dolayısıyla biçimleri bozulan saçak desenleri dijital bir CCD kamera tarafından yakalanırlar ve üç boyutlu topografik yüzey haritalarını çıkarmak için aşağıdaki sinyal işleme teknikleriyle işlenirler: Fourier Dönüşüm Profilometresi, Faz Adım Profilometresi ve Sürekli Dalgacık Dönüşüm Profilometresi. Bir optik mikroskop ve CCD kameraya hassas bir şekilde dahil edilen birinci optik fiber düzeneği, mikron ölçeğindeki çeşitli nesnelerin 3 boyutlu yükseklik dağılımını 5 μm'lik bir çözünürlükle elde etmek için geliştirildi. Önerilen tekniğin, ayarlanabilir bir frekansta yapılandırılmış ışık deseni üretmek için oldukça elverişli ve pratik olduğu gösterilmiştir. Lloyd aynasına bağlı mikrometreyi ayarlamak suretiyle fiber ve ayna arasındaki mesafeyi artırılarak, iki parlak saçak arasındaki uzaklık, projeksiyon ünitesinde herhangi bir ek parça kullanılmadan mikron ölçeğine indirilebilir. Elde edilen görüntünün faz analizi, Tek Boyutlu Sürekli Dalgacık Dönüşümü ile gerçekleştirilir.

TABLE OF CONTENTS

LIST OF FIGURES

LIST OF SYMBOLS

a_1	Amplitue of the beam
a	Scale factor
b	Translation parameter
c	Multiplication constant
f_0	Grating frequency
f	Distance between fiber end and screen
n	Refractive index
u_0	Carrier frequency
z(x,y)	Height distribution
F	Fourier Transform
$I(x, y)$	Intensity of image
K	Phase factor
N	Number of fringes
P_0	Fringe spacing
R	Resolution of system
δ	Distance between fiber end and mirror surface
θ	Illumination angle
λ	Wavelength of laser light
ϕ(x,y)	Phase value at that pixel
Δ	Path length
Φ	Phase Difference

LIST OF ACRONYMS/ABBREVIATIONS

2D	Two Dimensional
3D	Three Dimensional
BS	Beam Splitter
CWT	Continuous Wavelet Transform
CCD	Charged Coupled Device
DFP	Digital Fringe Projection
DLP	Digital Light Processing
DMD	Digital Micro Mirror Device
FTP	Fourier Transform Profilometry
LCD	Liquid Crystal Display
NA	Numerical Aperture
PSP	Phase Stepping Profilometry
SFIT	Scale Invariant Feature Transform
YAWTB	Yet Another Wavelet Toolbox

1. INTRODUCTION

A structured light pattern, which is based on interference phenomenon, occurs due the wave nature of the photons. Making use of the fringe projection in the 3D optical profilometry is one of the leading applications of the interference of light waves. This powerful properity of light is employed in various applications in many diverse fields such as industrial manufacturing and surface quality-control [1–3], human body monitoring [4], intra dental applications [5, 6], micro design of mechanical devices [7], micro fluidics [8], face recognition [9], non-invasive examination of surface profile measurements [10] etc. Nowadays, taking the advantage of the advanced CCD cameras, suitable light sources together with an efficient hardware, one can easily achieve leading methods for 3D surface topographic measurements with a fairly high resolution. A reliable, robust, noise-free and high-quality fringe projection enables much sensitive and high resolution 3D profile of target objects. There are many kind of optical surface profilometers, which use fringe projection technique such as single-mode fiber optic directional couplers [11–13], multi-core fibers [14], uniaxial system combined with a single imaging fiber [15], fringe pattern projected via DMD (digital micro mirror device) [16] etc.

Eventhough, most of the fringe projection methods provide very high precision, some of the techniques are restricted by their own system parameters. Consequently, many optical arrangements suffer from their own drawbacks, which limit the robustness, stability and the resolution of the fringe patterns. The importance of a well-designed fringe projection method is that it can reduce inevitable sources of errors that may reduce the efficiency of the fiber optic systems in the first step. Mentioned systems may be affected easily by some instabilities in the ambient temperature, vibrations, air turbulence etc. These factors can have unwanted shifts in the constructed light pattern, causing blurry areas or poor fringe visibilities. For example, vibrations with small amplitudes may easily change the position of the arms of a fiber directional coupler and may also introduce an unwanted phase difference between the light beams propagating in the cores of a multicore optical fiber. In other words, shrinkage or expansion in the couplers' arms or in the fiber cores due to temperature or vibration fluctuations is an inevitable problem for optical directional couplers and multicore fiber-based profilometric applications. As a consequence, nondiscrete and low-quality fringes decrease the resolution of the system, which subsequently increases the error in the results. Additional measures such as interrogating polarization controllers and piezo elements are needed for a directional coupler to eliminate these disturbing factors and to fix the projected fringe pattern during the image capturing process. A multicore fiber may not require any special polarization controllers or other equipment for precise alignment of the fiber cores; however, a fixed core-to-core separation limits the practicality of such a device.

A fringe projection method, which is reliable, cost-effective and easily adjusted for different scale size of the target objects, is required for an efficient and successful construction of a 3D optical profilometry. In this context, our research focus on the generation and optimization of a fringe pattern method that can meet all these requirements. A setup with mentioned features will provide convenience to the user to investigate optical surface topography of various samples, without too much effort in adjusting the whole configuration of the setup.

In this thesis, a novel fringe projection technique is introduced, which is named as fiber optics Lloyd′s mirror assembly, together with its applications to the 3D optical surface profilometry for various objects from micron to millimeter scale. Fiber optic Lloyd′s mirror fringe projection system is almost immune to any temperature fluctuations and vibrations. It is a well-described and easy technique for obtaining high-quality interference fringes. It is much more practical and more cost-effective when compared to other fringe projection systems. It also obtains various structured light patterns such as bright-dark strips through the adjustment of a single-mode optical fiber and an ordinary flat mirror. Bright-dark squares are obtained using a single-mode optical fiber with an orthogonally oriented double-mirror assembly. The author anticipates that using a fiber optic Lloyd′s mirror assembly makes the interferometric system even more compact, more stable, and much simpler than using the structured light pattern systems previously employed in optical surface topography applications.

Three very-well known methods of the optical profilometry studies are implemented here in our work. For the first time the fiber optical Lloyd′s mirror assembly is combined with these techniques and for each method discrete setups are built. The entire work is divided into three main application sections and the following subheadings first introduce Lloyd′s mirror assembly and then its three applications of the optical profilometry. Fourier Transform Profilometry (FTP), Phase Stepping Profilometry (PSP) and Continuous Wavelet Transform Profilometry (CWT) methods are aforementioned surface topography analysis techniques introduced for optical profilometry applications and they are used to extract the phase map of the deformed fringes. In all techniques, surface profiles are measured and compared with the real height distributions.

The 3D optical profilometry using fiber optic Lloyd′s mirror fringe interference is proposed in this thesis and the interference from the Lloyd′s mirror is explained in detail. In all three setups, this mirror assembly is used and experimental setup sketches show that the relative position of the mirror and the fiber due to the optical table axis may be different in each setup. An additional reference image is taken for every object image because of the obligation of the removal of the carrier frequency term from the total phase. Before each measurement, in every discrete setup, system calibration is done. Apart from others, this calibration is achieved for CWT technique by capturing a set of fringe pattern projected on the plane screen and then, the phase to height convertion is done. The real dimensions of the objects are measured precisely before the experiments. For Fourier transform (FT) and Continuous wavelet transform (CWT) methods, object and reference images are captured one by one, while in Phase stepping (PSP) fringes are shifted on the target object five times. After all shifting is achieved three sequential frames are chosen for processing. Different preprocessing methods are applied to captured images in each method due to the requirement of the images and the chosen unwrapping algorithm. Since the basic course of the technique is quite similar, a short list of general methodology is summarized as follows:

- The number of fringes projected on the whole surface of the target object are adjusted. The fringe width is taken small enough to enhance the distortions of the fringes due to the surface topography.

- Good quality frames of the deformed fringes are captured by a CCD camera. The sparkles and dark areas on the deformed fringe patterns always cause errors in phase unwrapping. The best way to minimize the problems in the phase extraction is to capture object images without any glare or shadows on the whole frame.

- Successful implementation of the three algorithms (FTP, PSP and CWT) are achieved. Suitable phase unwrapping algorithm for each method is carried out. A different phase unwrapping algorithm is used for each method and the relevant information about the unwrapping algorithms is introduced in each chapter individually.

- A phase (in radians) to height (in meters) conversion is done to extract a true 3D surface map of the objects. Such conversion is done theoretically by the FTP and PSP algorithms and is implemented experimentally by the CWT method.

Our research objectives can be listed as follows:

- The primary objective of the research is to achieve a reliable and robust fringe projection system and experiment its applicability by combining it with different optical profilometry techniques.

- It is important to know what kind of and what size of target objects can be measured using the optical profilometric system. So it is important to check various topography of samples in different sizes.

- The visibility limit of the fringes is important for a true description of the fringe projection so we aim to examine the visibility and the resolution of the projected patterns.

The experimental results show us that the suggested fringe projection technique can be a promising method for optical profilometry and surface topography applications. Fiber optic Lloyd′s mirror proves itself in nano and micro-lithography applications as a comparable option for surface patterning. Now, we aim to present its applicability and compatibility as 3D optical profilometry techniques. The layout of the thesis is given below:

- Chapter 2 is a *Review* part that covers a broad list of the applications of the optical and digital fringe projection techniques and a short introduction about the theory of interference of light beams and generation of the fringes.

- Chapter 3, *The Theory of the Lloyd′s Mirrors*, covers the theory of the Lloyd′s mirror and our fiber optics Lloyd′s, including one and two mirror configurations. The general information about the phase unwrapping and phase extraction methods are given in here. Finally, the carrier removal method is explained in detail.

- Chapter 4 is about the *FTP* method and it explains the theory, experimental setup and results of the Fourier Transform Optical Profilometry using Lloyd′s mirrors.

- Chapter 5 is about the *PSP* technique and it explains the theory, experimental setup and results of the Phase Stepping Optical Profilometry using Lloyd′s mirrors.

- Chapter 6 is about the *CWT* technique and it explains the theory, experimental setup and results of the Continuous Wavelet Transform Optical Profilometry using Lloyd′s mirrors.

- Chapter 7 is the *Conclusion* and it summarizes all the work done in this research and offers a global discussion of this fringe projection technique applied in optical profilometry with an emphasis on its advantages and limitations. Potential directions of further investigations and predicted developments are also discussed.

2. REVIEW

2.1. Applications of the Fringe Projection

Many diverse disciplines use fringe projection techniques as a valuable and reliable methodology in their research. Dimensions of the projection area of the fringe pattern may depend on the aim of the research and it can vary from nanometers or micrometers to the range of a few meters. Besides a vast number of applications of fringe projection methods, which are gathered under optical surface topography, lots of research papers in other fields present various application methods for fringe projection techniques. A list of research papers is introduced here to cover optical and digital fringe projection methods and its aim is to give an overall view of the applicability and the importance of fringe projection methods for various research fields. Fringe projection methods find themselves a large number of application areas in biomedical and health science such as 3D oral intra dental measurements [17–19], human body shape measurements and quick diagnosis and monitoring of scoliosis [20,21], face recognition techniques [22, 23],cosmetology applications and human skin topography [24,25] etc. Fringe projection based topography applications are done with a high precision in recent years and the technique shows its great potential in the field of the biological tissues and bioscience [26]. Besides biomedical research, micro and nano device application procedures also benefit from fringe projection methods for measurements of the precise topography of MEMS (micro-electromechanical systems) and chip design [27]. Fringe projection techniques do not just measure the topography of the target surface, they are also being considered as a means to form and shape a surface in nano and micro-scale using nano-lithographic techniques [28–30]. Surface topography measurements do not study only static and stable target surfaces, but also simultaneous measurements of replacement of rigid objects can be done easily using fringe projection methods and the 3-D surface topography of these targets can be constructed very fast and precisely [31, 32]. Using fringe projection on dynamic or static surfaces support 3-D topography measurements for machine design and vision such as the industrial inspection, and prototyping [33,34]. Optical topographic methods based on the fringe projection can easily be implemented in the research of free surface dynamics of liquids. A similar setup to rigid body shape measurements can be constructed by projecting fringes onto a vortex shape in a liquid [35] and further studies show that fringe projection techniques enable single-shot global measurements of free-surface deformations of the water waves [36]. As it is mentioned above, fringe projection techniques used in surface topography measurements are not restricted by dimensions. Thanks to the most applications that the fringes are projected by digital projectors, even 1.1 × 1.8 m^2 actual projection surfaces are possible for measuring free-surface variations in time [37].

2.2. 3D Optical Imaging Techniques

All the fringe projection applications which have been introduced in the above section are listed due to their applicabilities and the aim of the research in interest. Our main consideration is about the three dimensional optical profilometry of targeted objects, therefore we can restrict the fringe projection applications into 3D shape measurement techniques. Fringe projection methods are one of the leading branches of 3D imaging methods. Because of the remarkable variety of 3D optical techniques, their classification is not unique. Sansoni *et al.* presented a table of classification of 3D imaging techniques in Figure 2.1 [38]. In the following part, some of these techniques are chosen and are briefly explained one by one by including recent research papers.

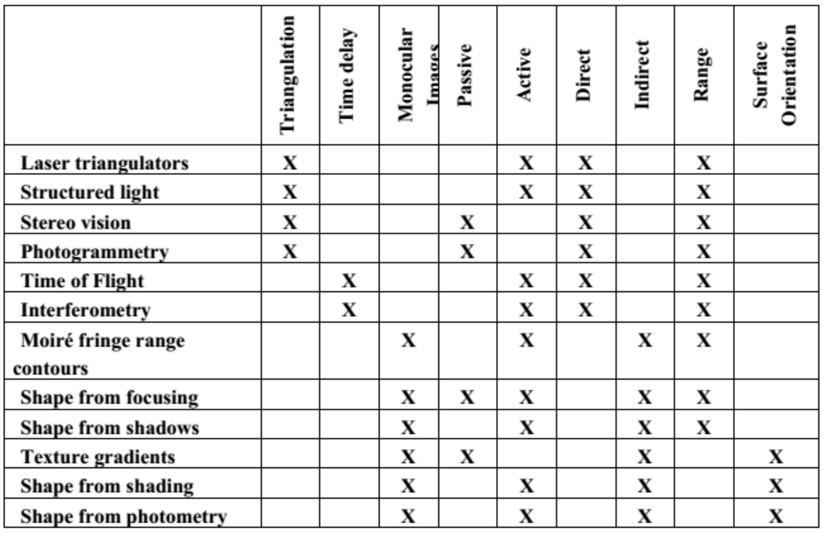

	Triangulation	Time delay	Monocular Images	Passive	Active	Direct	Indirect	Range	Surface Orientation
Laser triangulators	X				X	X		X	
Structured light	X				X	X		X	
Stereo vision	X			X		X		X	
Photogrammetry	X			X		X		X	
Time of Flight		X			X	X		X	
Interferometry		X			X	X		X	
Moiré fringe range contours			X		X		X	X	
Shape from focusing			X	X	X		X	X	
Shape from shadows			X		X		X	X	
Texture gradients			X	X			X		X
Shape from shading			X		X		X		X
Shape from photometry			X		X		X		X

Figure 2.1. Classification of 3D Imaging Techniques [38].

Time of flight method depends on the direct measurement of a laser or light pulse's flight time. Measurement is done by measuring a reference pulse which is passed through an optical fiber and then a second pulse which is reflected by the object surface. The variation between these two measurements gives the required information about the topography of the target and then the time data are converted to distance [39]. Point by point surface height description is gained by this method with a typical resolution of a millimeter. Using a laser diode with subpicosecond laser pulses, even submillimeter resolution is achievable.

Laser triangulation method is founded on the measurement of the view angle of a laser beam spot which is projected onto the object surface. The light beam distribution reflected from the object surface is analyzed and a CCD camera detects the pixel. The laser spot's position on the object surface and the position of the laser spot on CCD sensor are related to each other. In Figure 2.2, when the object is moved from position 1' to position 2', then a displacement of *ds* will occur on the CCD camera. Θ is the triangulation angle. Laser triangulation methods are point-based techniques and they are capable of sub-micron scale resolution [40]. Some inevitable effects can influence the measurements and reduce the resolution such as surface reflection, shadowing effects, disturbances of the laser beam at the edges of the target in concern, the diffusion and the absorption of the light beam.

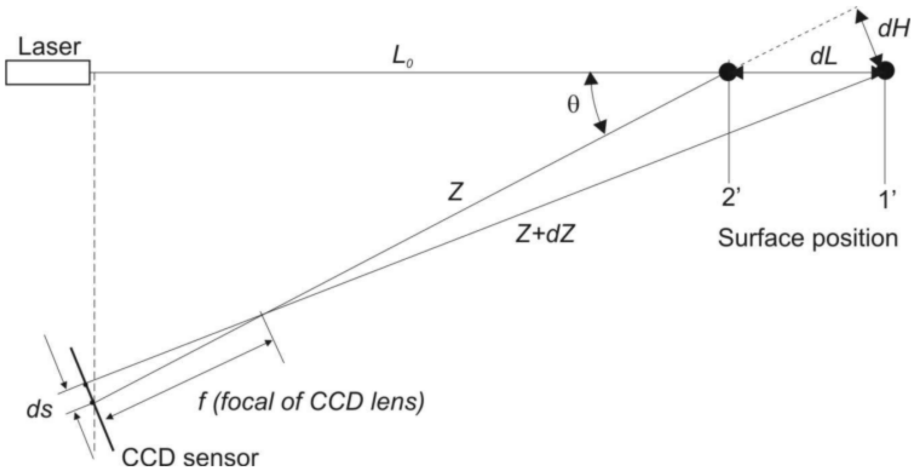

Figure 2.2. Sketch of Laser Triangulation System [40].

Photogrammetry uses a stereo technique to measure 3D shape of objects. The target surface of the object must include some bright retroreflective painted dots. Basic steps of the procedure include accurate camera calibration and orientation, image point measurements, 3D point cloud generation, surface generation and texture mapping. Some commercially available packages are used for complete scene modeling or sensor calibration and orientation. 3D reconstruction depends on the bundle adjustment method and it is analytically calculated using a geometric model, which holds the central perspective and the orientation of the bundles of light rays in a photogrammetric relationship [38, 41, 42]. One of the recent studies about prosthetics and orthotics surface measurements show that the photogrammetry techniques have some leading advantages over conventional laser scanning methods such as lower cost, compact and easy-to-use hardware, satisfactory measurement accuracy, and significantly shorter measurement time. Scale Invariant Feature Transform (SIFT) algorithm transforms image data into scale-invariant coordinates relative to local features and extracts more than 10.000 feature points from a pair of images. The accuracy of the 3D measurement technique is about 0.05 mm with very short measurement time (less than 1 min) [43].

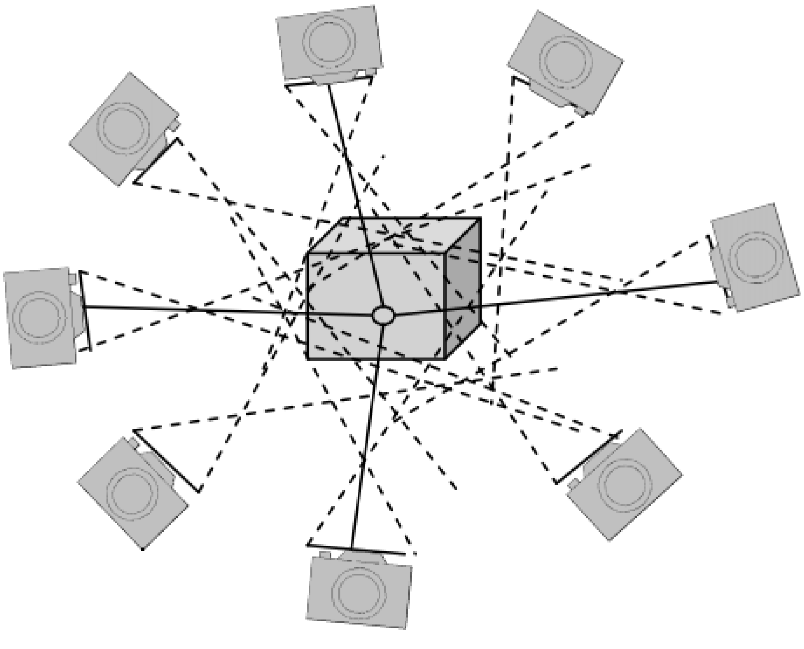

Figure 2.3. Photogrammetry of the picture sequence [43].

Another bright application is demonstrated in a recent study (Liu *et al.*, 2015). In that work, they achieved accurately and efficiently reconstructing a continuous surface from noisy point clouds captured by a 3D surface photogrammetry system (VisionRT). Using human bodies as the target surface, the introduced method can reconstruct successfully all patient topography and fill the regions of where raw point coordinate readings are missing. The reconstructed surface results of the human chest area and its CT scan results are compared and they present very similar mean curvature distributions. The proposed method offers submillimeter reconstruction accuracy under different configurations and presents a promising technique for radiotherapy applications to investigate local structural properties despite the presence of noise and missing measurements [44].

Stereo vision technique includes the following processing steps : image acquisition, camera modeling, feature extractions, correspondence analysis and triangulation. It does not require any specific light sources or special projections. The main principle depends on the capturing of the same frame by two or more cameras from different angles, simultaneously. The technique benefits from its simplicity and low cost, but it has some prominent problems about the identification of the common points of the image pairs. A recent study presents a flexible dynamic measurement method of three-dimensional surface profilometry which is based on multiple vision sensors [45].

Moiré technique evolved itself from low-sensitivity geometric Moiré to powerful and high capability of Moiré interferometry using the developing technology. An evolution of Moiré patterns and interferometry applications can be found in [46]. Basic description of Moiré pattern is that it is produced by two identical straight-line gratings rotated by a small angle relative to each other. If the gratings are not straight line gratings, the outcome lines are not equally spaced fringes [47]. Figure 2.4 shows some produced Moiré patterns and its variation due to tilting angle.

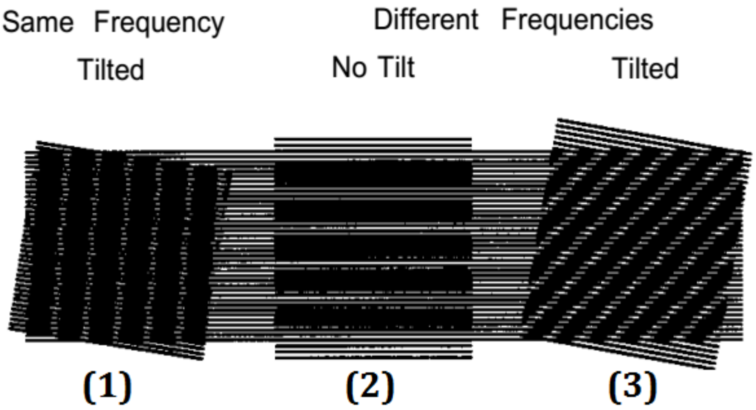

Figure 2.4. Moiré patterns caused by two straight-line gratings with (1) the same pitch tilted with respect to one another, (2) different frequencies and no tilt, and (3) different frequencies tilted with respect to one another [47].

The Moiré interferometry is based on two-beam interference. Two beams of light which are mutually coherent illuminate a diffraction grating which is produced on a flat surface of a specimen. The light beams are diffracted from this surface and the first diffraction order of one and minus one produce an interference, which is captured by a camera. Two-beam Moiré interferometer is sketched in Figure 2.5. The working principle of Moiré interferometer is defined as follows: First of all, the system is arranged to make the number of fringes zero (the fringe pattern is so-called null field) and then a load is applied, specimen deforms and hence the surface grating is deformed. By this method, the information about the deformation of displacement on a flat surface of a specimen can be gained. A review study explains two-, three- and four- beam Moiré interferometers in detail in Ref. [48]. Various methods are developed such as the snapshot or the multiple image Moiré systems for reducing environmental perturbations, increasing image acquisition speed, and utilizing phase shift methods to analyze the fringe pattern. Phase shifting Moiré method has capability of measuring 1 mm to 50 cm measurement range with resolution of 1/10 to 1/100 of a fringe [42, 49].

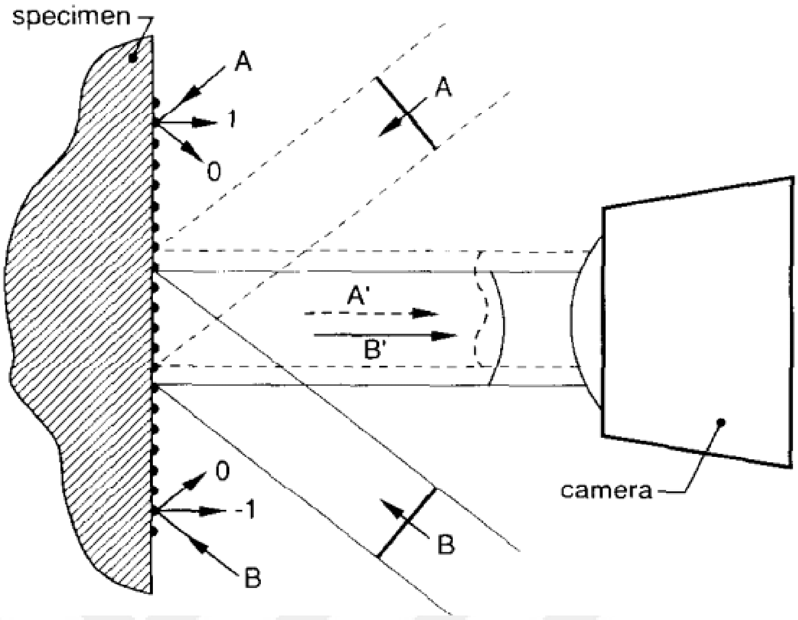

Figure 2.5. Basic Moiré Interferometry [49].

Interferometric methods require such an optical arrangement that two or more light beams, which are derived from the same light source, travel along different paths and construct an interference. The light sensor detects or a CCD camera captures this interference pattern, which carries the object height description in it. Interferometric methods can be classified according to the number of the wavelengths working in the system such as single, double or multi-wavelength systems. Due to the number of the light beams, systems have specific measurement ranges and their own mechanisms. For two-beam interference, one beam is called as the reference and the other one is called the reflected beam from a target surface so that an optical path difference is occurred between each other. ϕ_1 and ϕ_2 are defined as the phases of the two beams and their amplitudes are a_1 and a_2 at a given point, respectively. $\Phi = \phi_1 - \phi_2$ is the difference of the phase due to the optical path difference. This phase difference is directly related to the displacement field at the target surface and it is determined by the optical configuration of the setup. The Michelson, the Mach–Zehnder, the Sagnac and the Fizeau are best known two-beam interferometers while the Fabry–Perot is a leading multi-beam interferometer. Paragraphs below explain some leading interferometry methods in short and give some examples from the recent studies in the literature.

In Michelson Interferometry, the light beam is split and then is recombined again at the beamsplitter(BS). A diagram of the setup is given in Figure 2.7. After a light beam is split by a beam splitter into two parts, these beams follow different paths. After traveling different paths at different times, these two beams are brought together and interfere with each other. In Figure 2.7 beam splitter (50:50) splits light into mutually coherent two beams and one of these is transmitted onto the mirror M1 while the other part is reflected by the fixed mirror M2. Compensating plate is used to equalize the optical paths of the two beams. A mutual image of M2 mirror appears as M2′ because of the reflection at the beam splitter and the interference of the beams can be observed on the screen. The separation between M1 and M2′ and the nature of the light source adjust the interference pattern [50].

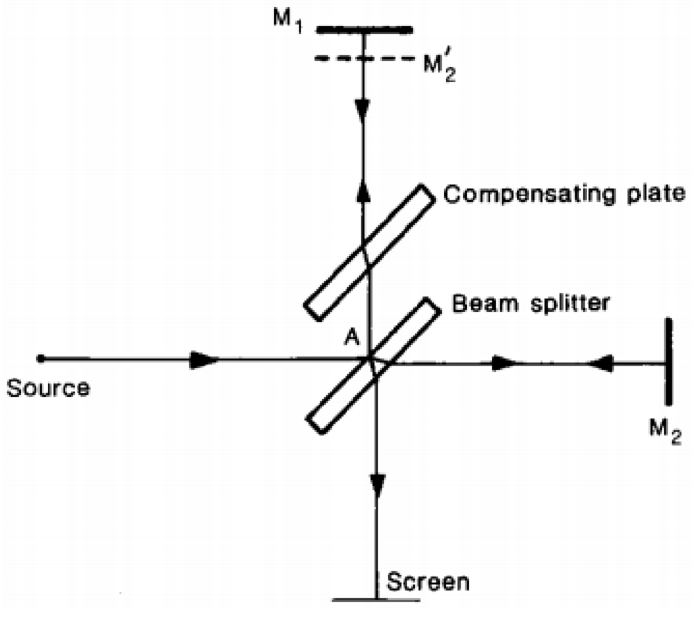

Figure 2.6. The Michelson Interferometry [50].

In recent studies, researchers aim to combine different surface profilometry techniques to enhance the resolution of the setup while decreasing the total cost of the optical system. Lai and Hsu demonstrated the Michelson Interferometry system combined with the Mach-Zehnder Interferometry. Total system has a wide-field imaging in millimeter range while an axial resolution within ± 5nm without any special preparation of the sample or any protection of it. Setup consists of a piezo-electric transducer as an optical delay component on the reference arm of the Michelson interferometry. A two-axis translational stage is synchronized with the piezo electric transducer for 2D lateral scanning and the sample is attached to the stage. The surface height of a point is extracted by subtraction of the phases of the two interference signals, which are detected by two photodetectors. The mathematical derivation of the phase and the further details can be found in Ref. [51]. Figure 2.7 illustrates the composite interferometer where dark gray-colored arms are referred to the Mach-Zehnder interferometer while light-gray-colored arms belong to the Michelson interferometer.

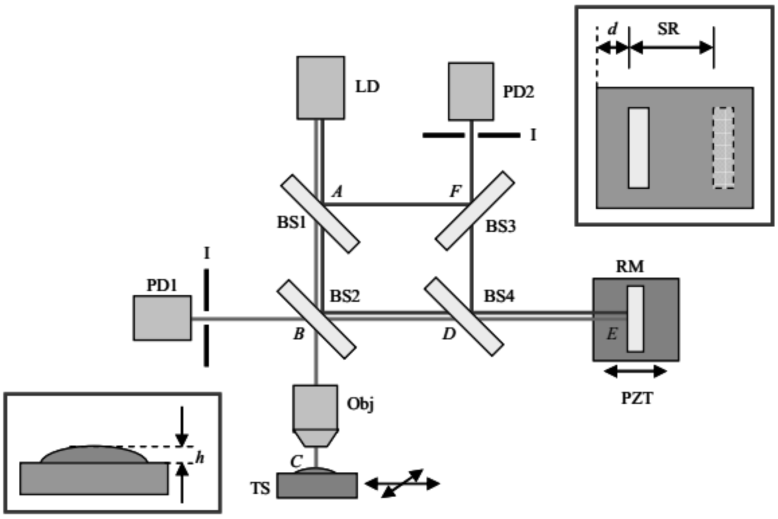

Figure 2.7. Schematic of the Composite Interferometer [51].

The Mach-Zehnder Interferometer uses a beam splitter to split the light beam into two beams and then a second beam splitter recombines them together. The spacing of the fringes is adjusted by changing the angle between the beams emerging from the interferometer. One of the valuable features of the Mach-Zehnder interferometer is that the two paths of the light are separated widely and are transversed only one time. Also the regions of localization of fringes on the test object can be arranged in a way that an extended source of high intensity can be used [50].

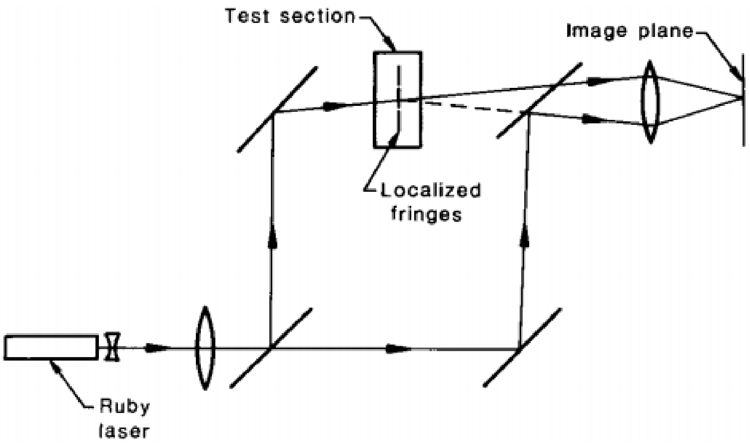

Figure 2.8. Schematic of the Mach-Zehnder Interferometry [50].

Sagnac Interferometer consists of two beams, which follow the same path in the opposite directions. Common path interferometers are less problematic about the external vibrations and the air currents, that is, they can support a much stable fringe pattern. Owing to the similar optical paths in the Sagnac interferometer, a white light source can produce an interference pattern easily. The Sagnac interferometer types are illustrated in Figure 2.9. The interferometer may have an even number of reflections in each path (see Figure 2.9a) or an odd number of reflections in each path (see Figure 2.9b). One important point is that the Sagnac interferometer with the odd number of reflections can not be called as a common- path of interferometer because these kind of wavefronts are laterally inverted to each other on some parts of the optical path. Fiber Sagnac interferometers are generally used for rotational sensing applications. A surface profile application of a phase shifting laser diode Sagnac interferometry is introduced in Ref. [52]. Between p and s polarized beams, an unbalanced optical path is introduced to achieve phase-shifting. The study compares Sagnac interferometry with Twyman-Green interferometry to confirm the robustness of the optical setup.

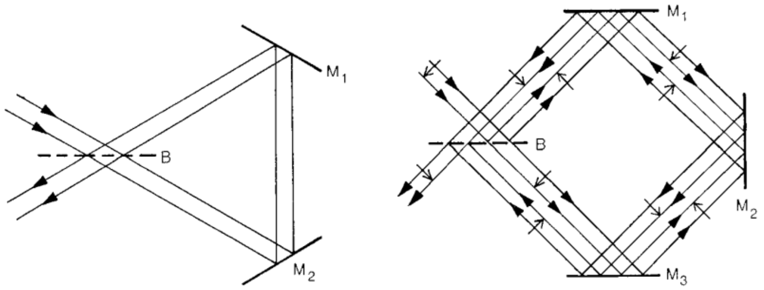

(a) (b)

Figure 2.9. Two general forms of Sagnac Interferometry [50].

The Fizeau Interferometer uses an air gap between reference and the target flats so the light reflected from these two flats construct interference pattern. Fizeau interferometer is commonly used for testing surface shapes, flatness and parallelism of optical components. A commercial laser phase-shifting Fizeau interferometer with a tunable laser system is given in Figure 2.11. The schematic shows the reference flats and the target object. Four different frequency patterns are generated by the reflections from four surfaces, which are named as transmission at S_1, plate front surface S_2, plate back surface S_3, and reference surface S_4. Finally, each fringe pattern is analyzed by a software program and then the surface information from the optical flat is gained with an uncertanity in the measurement of 15 nm [53]. A multi-beam Fizeau-Tolansky interferometry setup is illustrated in Ref. [54] which is based on an automatic fringe thinning process and measures a calibrated step height of (27.00 ± 3.00 nm).

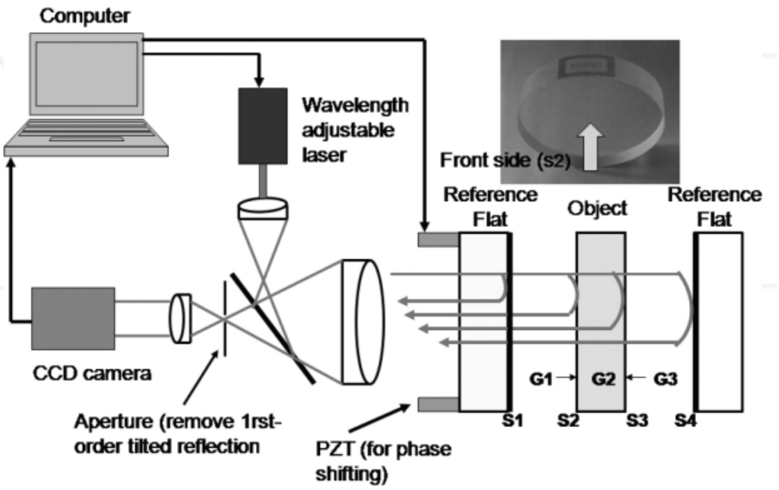

Figure 2.10. A commercial laser Fizeau Interferometry [53].

Two parallel slightly wedged mirrors with highly reflective (R> 0.95) semi transparent surfaces are placed opposing in the Fabry-Perot Interferometer. The outer surfaces are curved to make small angles with the inner surfaces. These two surfaces are separated by a distance d and filled with a medium with reflective index n. It is called the Fabry-Perot ethalon if the spacing between surfaces are fixed and in this case, each wavelength produces a system of rings centered on the normal to the surfaces. Confocal-Fabry-Perot interferometry is achieved using two spherical mirrors whose separation is equal to their radius of curvature r. Confocal Fabry-Perot interferometers exceed the limitation that is related to the size of the input and output apertures while the plane mirror configurations have to face with it. Figure 2.11 shows a confocal Fabry-Perot interferometry where an input beam transverses four times between mirrors before it emerges from its original path. A uniform field is achieved because the optical path difference does not depend on the angle of the incidence. A recent study introduces an innovative laser profilometer using a Fabry-Perot etalon and an objective [55]. The experimental setup has a sensitivity, vertical resolution, and stability of 1.62 μm, 2.2 nm, and 6.6 nm, respectively.

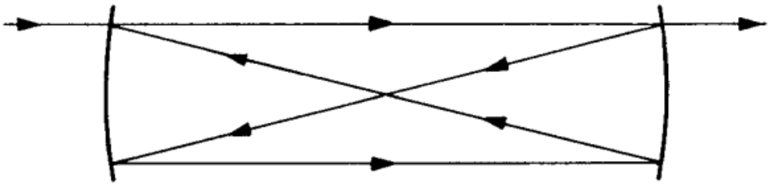

Figure 2.11. The Confocal Fabry-Perot Interferometry [50].

The most basic fringe projection system consists of a projection unit, an image acquisition unit and a processing or analysis unit. In general terms, the fringe projection technique depends on the phase information, which is extracted from the deformation of the projected fringes on the target surface. Due to the surface profile of the target (it may be rigid or soft or even liquid surface), the phase map of the deformation can be calculated by the fringe analysis. Studies about the fringe projection techniques generally focus on two main subtitles about the source of the projected light beam. These are fiber optic fringe projection and digital fringe projection (DFP).

Digital fringe projection (projected coded light) attracts the researcher because of its advantages over other fringe projection methods. Its key ability is to adjust fringe patterns easily with a high precision in software. Fringes are formed digitally so the intensity of each pixel changes due to the digitally coded pattern and then this pattern is projected on the target surface. A video camera (an imaging sensor) captures 2D image of the scene under structured light illumination. The method studies the variation between the scene of the structured light pattern that illuminates a planar surface and the scene of the deformed light pattern due to the object surface. The surface of a non-planar object's surface distorts the projected pattern and this deformation carries 3D height information in it.

Generally, these fringe projection sources can be Liquid Crystal Display (LCD) or Digital Light Processing (DLP) with a standard 24 bit bitmap image. Digitally formed fringes have in fact discrete-like intensity distribution and the resolution of the captured frame can vary from $600\times$ 800 up to 1600 $\times$ 1200 pixel resolution. Sequential binary-coded patterns, gray-level coding patterns, continuously varying color-coding, stripe indexing color coding, stripe indexing gray level coding, color coded patterns are most prominent techniques. More details about generation, projection and derivation of height description from digitally coded patterns can be found in a tutorial by Geng *et al.* [56]. Their work presents a well and comprehensive classification framework of the structured light 3D imaging techniques. However, compared to the laser based optical fringe projection techniques, the discrete nature of the digitally formed fringe patterns face with a theoretical limitation on the accuracy of the setup. The fringe pattern is pixelated and each pixel has a fixed intensity value. Baker *et. al.* studied the accuracy limitations which are based on digital projections in 3D optical profilometry applications. Additionally, they introduced that spatial distance can be considered as the major factor for determining the accuracy of the optical setup. They proclaimed that the distortion of spatial distance in x-direction is the only concern to be able to calculate the height description of an object at any one point. Also, they introduced a frequency minimum for the fringe pattern so that no neighboring pixels are of identical intensity and much smoother and non-discrete fringe patterns are formed [57]. Many applications of the digital projectors with various kinds of the structured light patterns are studied in the literature such as triangular pattern [58], saw-tooth fringe pattern [59, 60], optimal intensity modulation [61] etc. Digitally coded patterns will not be considered in this thesis but further details will be given in fringe projection part to clarify fringe generation process.

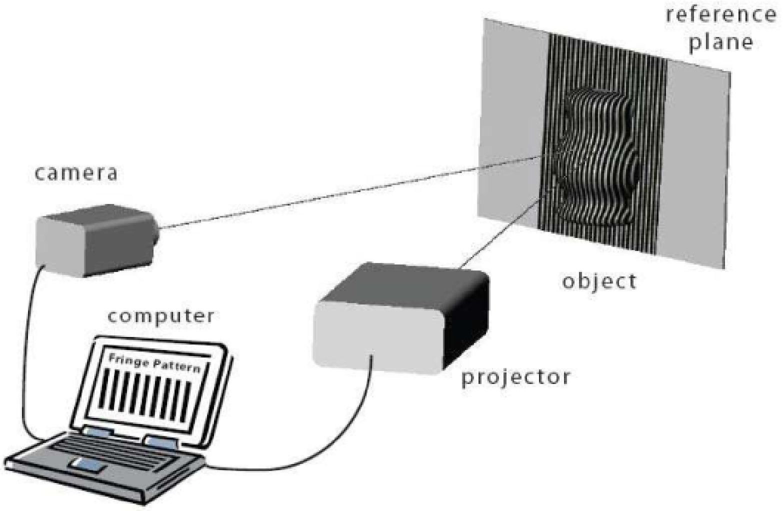

Figure 2.12. Basic sketch of digital fringe projection setup [62].

DLP projectors achieve various forms of fringes for projection because of easy and computer-based control of generated patterns. But due to the electronic noise of the projectors and non-linear relationship between the brightness and the bias, some inevitable errors happen. Additionally, if the fringe resolution does not vary sinusoidally, it leads to errors in the measurements. Using fiber optic fringe projection methods increases the density of the fringes, detects much smaller phase variation and improves system accuracy. The whole fringe generation part of the setup can be smaller in size, the system can have strong anti-interference ability to electromagnetic radiation and benefit from remote placement of the laser sources.

Fiber optic fringe projection methods are mostly based on employing laser sources coupled into optical fibers. The fiber may be single, two or multi-core according to the chosen application procedure and then an interference is achieved. Various methods or techniques such as optic couplers, two or multi-beam interference, multicore fibers etc. are used to generate an interference pattern. Unlike digital fringe projection methods, fringe frequency is adjusted by some specific optical apparatus and all methods have some advantages or weaknesses compared to digital fringe projectors.

Multi-core fibers carry more than one core, and these fibers are manufactured in a form that the core separation is fixed, symmetric and cores are placed inside the same cladding. Early applications had an even number of cores, recent studies permit various numbers and different sizes of the cores inside one cladding. Karahan *et al.*, 2004 proposed a four-core optical fiber for fringe pattern generation and by the interference of the four wavefronts emitted from each core, the fringe pattern is projected on the object surface. Four core generate a square shape fringe pattern and the rigid object is measured with an rms error of 0.4 mm [63].

Although all fringe projection methods used in optical surface topography are valuable and have very high precision, they all suffer more or less from some external factors and are restricted by some inevitable reasons. Fiber optic couplers and multi-core fibers are very-well known optical fringe projection techniques and many research papers mention topography applications of these methods [12, 63–65]. However, when an optical coupler or a multicore fiber is used alone, external disturbing factors can inadvertently cause misalignment of the fibers, which may demolish the stability of the interferograms. Another point to note that vibration and thermal effects can easily change the relative positions of both arms of the fiber coupler as well as fiber optic core separations, which cause phase changes between optical path lengths leading to a shift in the whole structured light pattern giving unreliable results of the surface topography. In addition, blurred and non-discrete fringes due to external factors may increase the error in phase extraction process and these effects consequently result in a decrease in the resolution of the constructed surface topography. Consequently, extreme sensitivity to ambient temperature, wind, pressure, and all other disturbing factors in the environment put a limit on such systems in real applications. For instance, multicore fiber finds itself a large application field in the field of the optical sensing including surface topography. However, fixed core separations and high manufacturing costs of a multicore fiber limit the ultimate borders of the interferometry in practical applications, in addition of the pattern being vulnerable to environmental disturbances.

2.3. Fringe Generation

This part covers the mathemathical language of the interference. Before we move on to our own technique, a short description of the interference is introduced in this section. Interference can occur when two or more light beams overlap in space. The resultant light patterns intensity is given by;

$$\begin{aligned} I = |u|^2 &= |u_1 + u_2|^2 = U_1^2 + U_2^2 + 2U_1U_2cos(\phi_1 - \phi_2) \\ &= I_1 + I_2 + 2\sqrt{I_1I_2}cos\triangle\phi \end{aligned} \tag{2.1}$$

where $\triangle\phi = \phi_1 - \phi_2$ and the term $2\sqrt{I_1I_2}cos\triangle\phi$, is called the interference term. The beams interfere destructively if the two waves are out of phase i.e.($cos\triangle\phi = -1$) and the intensity I reaches its minima:

$$\triangle\phi = (2n+1)\pi \quad for \quad n = 0, 1, 2, ... \tag{2.2}$$

When the waves are in phase i.e. ($cos\triangle\phi = 1$), then, a constructive interference occurs, giving;

$$\triangle\phi = 2n\pi \quad for \quad n = 0, 1, 2, ... \tag{2.3}$$

So the intensity I reaches its maxima. Two beam with equal intensities result in;

$$I = 2I_0[1 + cos\triangle\phi] \tag{2.4}$$

which is the fringe interference intensity for ordinary two plane waves. The description of the Lloyd's mirror interference will be explained in the next chapter on Fiber Optic Lloyd′s Setup with Equation 3.1. The interference pattern of the Lloyd′s mirror is quite similar to that of the Young′s double-slit experiment. The only difference is that an additional π to the phase difference is introduced due to the phase shift on reflection, which arises due to the difference between indices of refraction of the two media. This extra shift by an amount π results in an exact opposite situation in Equation 3.2 for

Lloyd′s fringes compared to Equation 2.2, so the first fringe will not be zero but has the highest intensity. That would normally bring an extra π term inside every intensity description for the later chapters, for example in Equation 4.12 for FTP, Equation 5.1 for PSP and finally for Equation 6.1 in CWT sections. To simplify the extraction of the phase terms from the intensity equations, this extra π is not included. The phase of the interference fringes is a total of carrier frequency term, the modulation term and π term. Absence of π does not constitute a problem in our calculations because in all sections we use reference subtraction to extract the carrier frequency term from the total phase. This is achieved using an extra frame which belongs to undeformed fringes, then subtracting the phase of this pattern from the phase of the deformed pattern. During this process, the extra π is also subtracted from the total phase and finally we achieve only modulated phase information.

3. THE THEORY OF THE LLOYD′S MIRRORS

3.1. Introduction

Lloyd′s mirror method was first introduced in 1834 by Humphrey Lloyd [66] and it is an interesting example of two-source interference, which is similar but distinctively different from two-slit interference. This interference is formed by two mutually coherent point sources; that is, by the real fiber optic source and its image in the flat mirror. If the difference of the paths traversed by these lights amount only to a small multiple of the length of an undulation, the two lights will form fringes. The light reflected from the surface of the mirror causes a π phase shift upon reflection and results in the fringe pattern to invert. That reveals itself on the center fringe pattern, while the Young′s center fringe is bright after interference, Lloyd′s center fringe (first fringe) is dark.

Lloyd′s mirror implementation in nano-patterning and optical interference lithography become popular in recent years. Placing opposite two alike mirrors [67], developing a tunable Lloyd–mirror interferometer with two degrees of freedom [68], building a two–axis Lloyd′s mirror interferometer with 2D diffraction gratings placed on different axes [69], using a 90° v–block apparatus for mirror configuration [70] and patterning non–circle peaks with double exposure using a rotating sample holder [30] enable different nano–pattern features. All listed experiments, and even more, prove that the Lloyd′s mirror configuration for laser interference lithography applications successfully achieve various types of nanopatterning structures up to 1000 nm pattern periods.

3.2. Fiber Optics Lloyd′s Setup

There are two principal methods for producing coherent sources for interferometry. One uses the division of wavefront, as in the Young′s double slit experiment. The second divides the amplitude between two arms, as in the Michelson interferometer. The Lloyd′s Mirror approach uses wavefront division at a mirror to produce two-source interference patterns.

A single mirror Lloyd′s interferometer is basically a fringe pattern source, which is constructed by one optical fiber and a mirror where the optic fiber is placed very close to the surface of the mirror. The optical fiber, which is named as the source, emits coherent light into a cone and a portion of that light follows a path that goes directly to the screen while the other part of it reflects from the mirror at a large angle. The reflected part of light also reaches the screen and this light beam is called the virtual source. If the light beams (light sources) of the two paths are in phase then a bright fringe appears, else the light is out of phase and a dark fringe is formed establishing its wave nature. Figure 3.1 presents the Lloyd′s mirror interference. The interference fringes are formed on the screen and f is the distance between the optic fiber tip and the target screen. The short separation between the optical fiber and the virtual fiber is given as δ and it is assumed to the small. This separation is twice the distance between the fiber tip and the mirror surface.

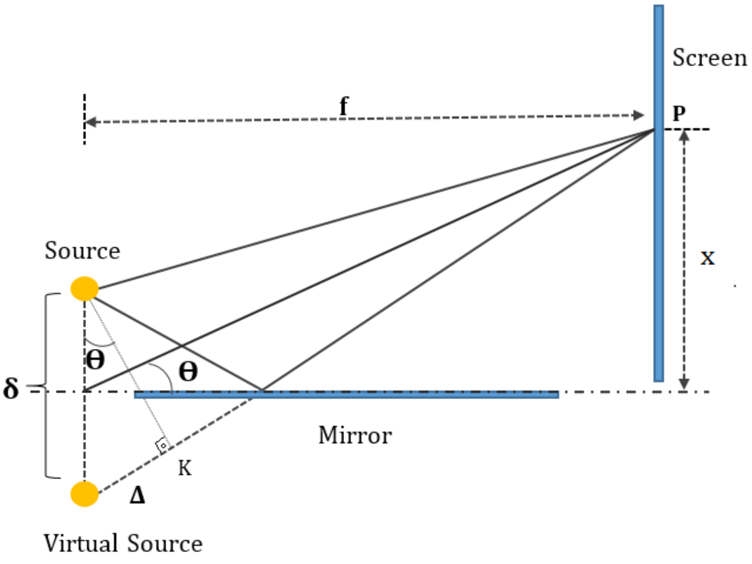

Figure 3.1. Single mirror Lloyd′s setup (not to scale)

The wavefronts from each source are superimposed and the interference of beams at a chosen point on the screen can be constructive or destructive. The distance of this point to the center line is given as x and the total interference of light beams forms a fringe pattern on the screen. The phase difference of the two waves at point P gives the intensity of that point and the relation between the phase and the path length difference can be extracted by geometry. Path length difference is denoted by Δ and it is defined as the distance between the virtual source fiber end and the point K. Using small angle approximation and triangles, it can be derived that θ is equal to $\frac{x}{f}$ and also $\frac{\Delta}{\delta}$. Hence, the theory of Lloyd$'$s assembly is quite similar to the Young$'$s double slit interference. The major difference is related to the light beam reflection from the mirror surface, which results an extra phase shift π;

$$\phi = k\Delta - \pi = \frac{2\pi}{\lambda}\delta sin\theta{-}\pi \tag{3.1}$$

where k is wave number, so ϕ can be written as;

$$\phi = \frac{2\pi}{\lambda}\delta\frac{x}{f}{-}\pi \tag{3.2}$$

we can extract the bright fringe position x from the formula;

$$x = (\frac{\phi}{2\pi} + \frac{1}{2})\lambda\frac{f}{\delta} = (m + \frac{1}{2})\lambda\frac{f}{\delta} \tag{3.3}$$

So bright fringe position for any integer “m”value can be calculated. The interference of the real and the virtual light sources form a fringe pattern on the target screen and the intensity of the light beams are assumed to be similar. It should not be avoided that one of the beams is reflected directly from the mirror surface, so its intensity will be a function of the reflectivity of the chosen mirror. The loss of visibility of a regular mirror is not much and we assume the beam$'$ intensities are similar.

3.3. One and Two Mirror Lloyd$'$s Assembly

During the whole study, various fringe patterns are produced and projected on the target surfaces. The main construction of the fringes and implementation of them into optical profilometry are quite similar and in each chapter, detailed description and the configuration of the optical setups are introduced. In a general framework, single and double mirror Lloyd$'$s interferometers will be explained in this section and a few chosen fringe patterns are given to show the easy adjustment of spatial frequency of the fringe pattern.

A single mirror Lloyd′s fringe pattern assembly is similar to the above description in Figure 3.1. The projection alignment of the fringes can be changed by the help of the positioning of the mirror-fiber set on the optic table. Modifying the system to double mirror Lloyd′s assembly is done by placing the optic fiber at the intersecting edge of two perpendicularly positioned mirrors. Because the mirrors are perpendicular, the virtual image of real fiber will appear in both of the mirrors and then the system can be considered to have four different sources labeled as S1, S2, S3 and S4 in Figure 3.2.

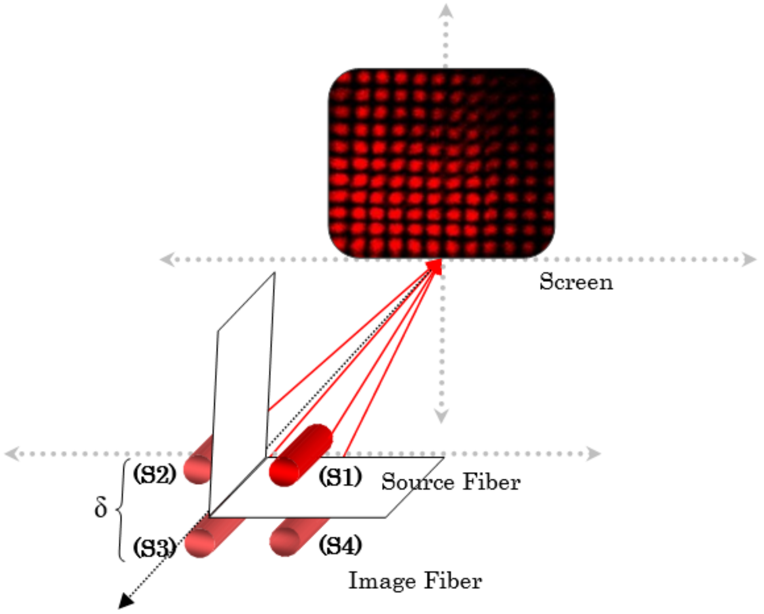

Figure 3.2. Double mirror Lloyd′s setup and projected fringe pattern.

Every virtual source is placed at the same distance from the origin and the source separation between each other is given as δ. Such a single mode optical fiber source and its three virtual images in the flat mirrors act like four monochromatic wave sources whose superposition produce a squared–fringe pattern at the far–field. The pattern shape depends on the angle between the mirrors and changing the angle results in extensions of the constructed square shaped fringe pattern. Detailed information and various shapes of constructed fringe photos will be given in the experimental part. The fringe spacing directly depends on the distance between the source fiber and its images. Increasing core separation δ, decreases fringe width so we can produce finer and finer features in the interference pattern. A combined image of single and double Lloyd′s mirror fringes is given in Figure 4.7.

After all the setup is set, the distance between mirror and the fiber can be adjusted and so various forms of fringe patterns can be achieved with little effort. Below fringe patterns are constructed with our Lloyd′s fringe projection technique with different frequency values. These are the real images of the patterns without any filtering. Profile intensity spots are obtained by cropping thin slices out of these frames at specified positions. Figure 3.4 gives the intensity versus spatial distance for each different frequency along the same path. Larger fringes are much brighter so the intensity of the highest frequency is a little bit waned.

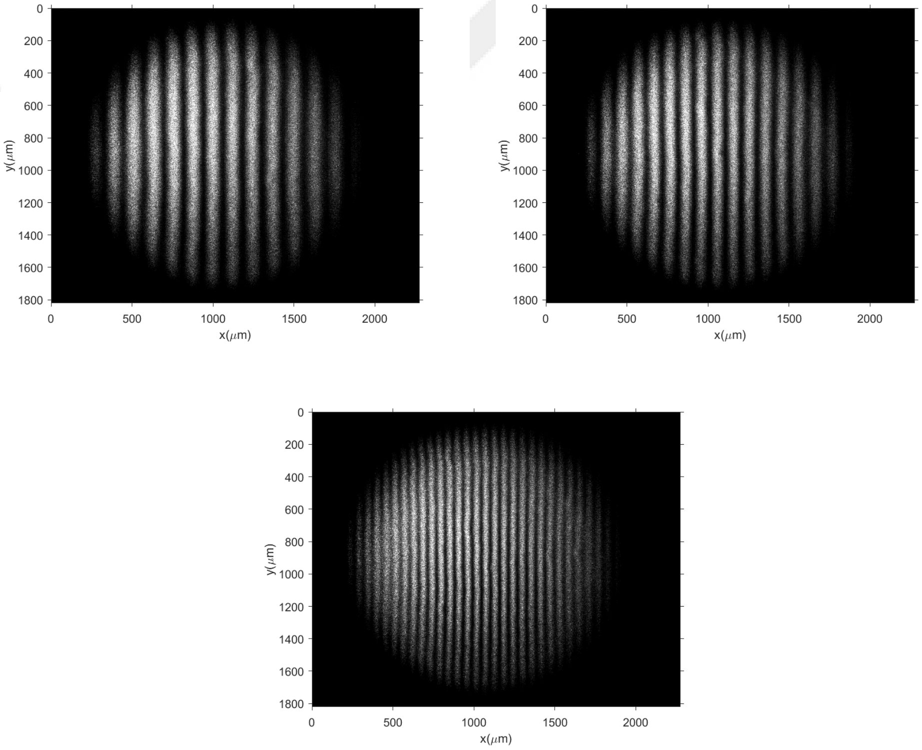

Figure 3.3. Fiber optics Lloyd′s fringe patterns with different fringe frequencies.

The frequency of the fringes are adjusted easily by moving the fiber tip further or closer to the mirror surface. The frequency values of above fringe patterns are given in Figure 3.4 with frequency values of 8.0 mm^{-1}, 10.0 mm^{-1} and 17.6 mm^{-1}, respectively.

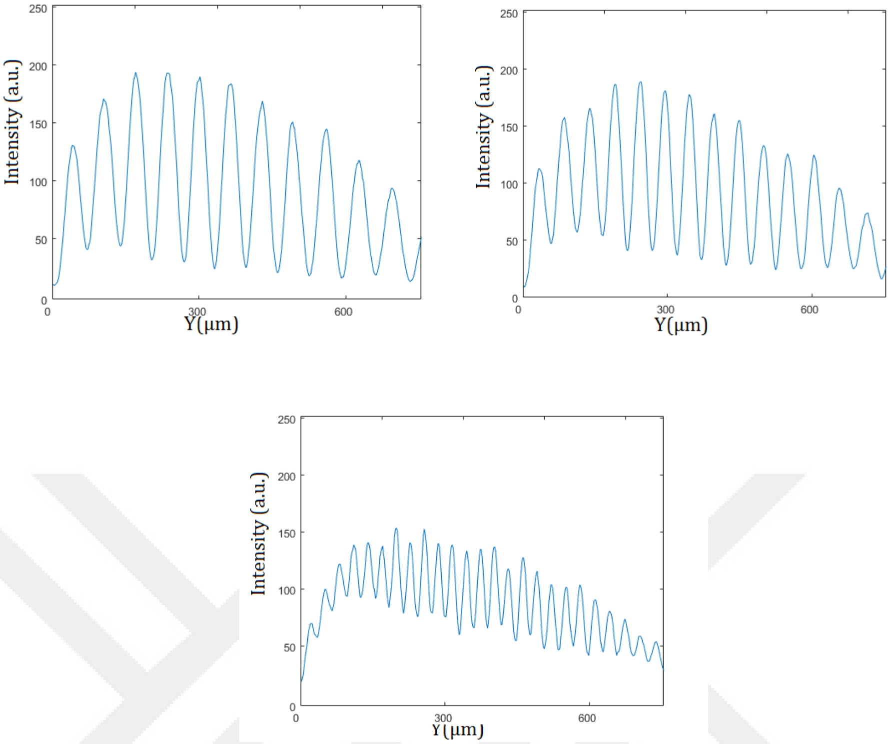

Figure 3.4. Fringe frequencies for the patterns in Figure 3.3.

There are numerous ways to construct an interference pattern optically. Beside fiber optic based fringe patterns, another prominent option is using a digitally-coded fringe pattern. Below figures belong to a digitally formed fringe pattern projected on a triangular shaped object. Figure 3.5 represents the distorted fringe pattern and its three color-channel components.

Digital coding supports a large variety of fringe patterns to the user and the construction of the fringe pattern can be even easier compared to the optical methods. But Binary Coding also brings along some restrictions or limits, which are not a subject-matter for optical fringe projection techniques. The restrictions of the digitally formed fringe patterns will not be given in detail in this study. Further details can be found in [57, 71–73].

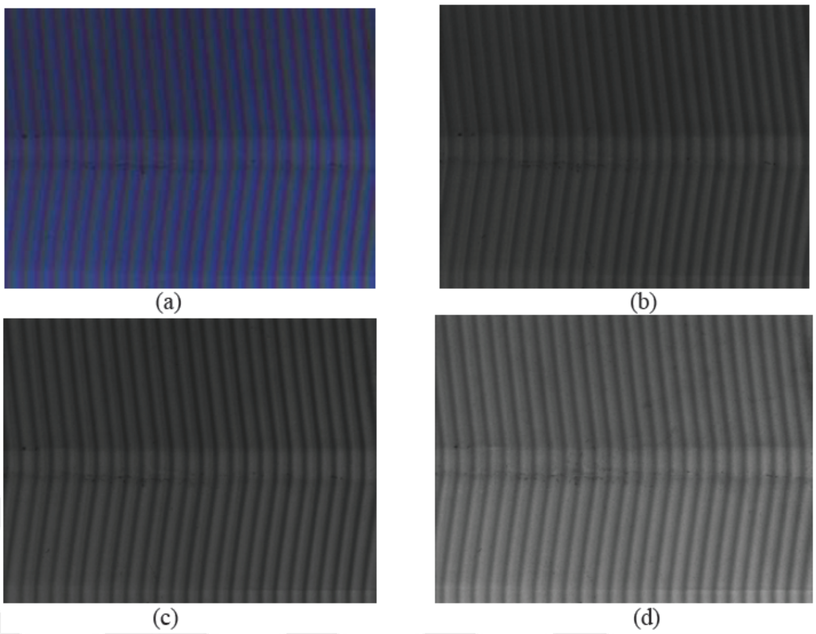

Figure 3.5. Captured distorted fringe pattern. (a) Color-encoded distorted fringe pattern; (b) Gray distorted fringe pattern of Red channel; (c) Gray distorted fringe pattern of Green channel; (d) Gray distorted fringe pattern of Blue channel [74].

3.4. Phase Unwrapping and Phase Extraction

Phase unwrapping and phase extraction is a very important step for a successive surface height description in optical profilometry methods. Before we move on to particular techniques we use with our Lloyd's mirror fringe patterns, we need to discuss two issues that are handled commonly in each of the technique. The intensity distribution of the deformed fringe pattern carries the phase modulation term. The deformation information of the fringe pattern due to the surface topography of the target object can be extracted from this phase modulation matrix. In further paragraphs, how this phase information is turned into surface height description is explained for each of the given optical profilometry techniques, separately. The Equation 5.7 gives the phase information and it is a wrapped phase with 2π phase jumps. This discontinuous phase needs to be unwrapped. In Figure 3.6 the wrapped and in Figure 3.7 unwrapped phase matrix are shown for Phase Stepping Profilometry, respectively.

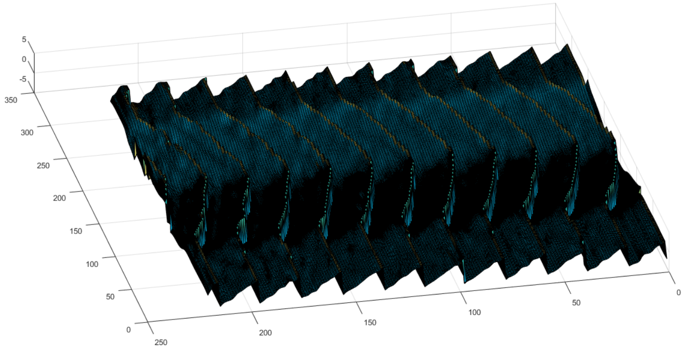

Figure 3.6. Wrapped phase map of a triangular object for PSP

Figure 3.6 clearly shows that the phase deformation is related to the surface variations of the triangular object. The phase is saw-tooth like because of the tangent function takes values in the range of $-\pi$ and π, and when the phase value is changed by 2π every time, a discontinuity occurs. Phase unwrapping process removes these 2π steps and forms a continuous and smooth phase map. Noise in the phase data may result in false identification of such phase jumps. If the amplitude of the noise approaches to 2π, the real phase jumps become unclear. That problem may be reduced by filtering the image and smoothing the sinusoidal fringe pattern but it must be kept in mind that the filtering always causes some loss of information. The researcher should be careful about the peaks and the valleys of the target object because at such points the fringe lines may be broken or shifted. The dark places that the fringe lines are crossed over are another troublesome points for phase unwrapping. The researcher must choose the most suitable phase unwrapping algorithm for the deformed fringe pattern. Additional information about phase unwrapping techniques can be found in [75].

In our study, an anisotropic diffusion mask is implemented on fringe patterns in phase stepping process. This mask removes discrete white and dark spots on the frames and helps to get rid of the problems relative to these points during phase unwrapping process. Then, a phase unwrapping algorithm is utilized.

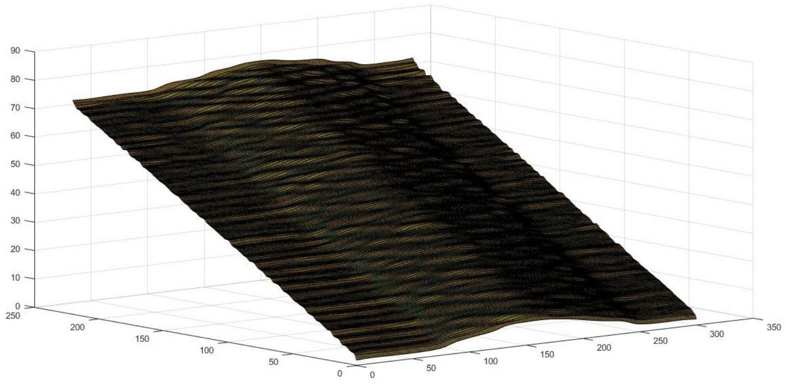

Figure 3.7. Unwrapped phase map of a triangular object for PSP

In Continuous wavelet transform method, the captured frames are pre-processed by a denoising filter. So the fringes are much smooter and the noise is reduced.

3.5. Carrier Removal Method

All of our experiments use a nonlinear carrier removal technique for reducing the carrier frequency component in the total phase. The tilt on the Figure 3.7 is removed by substracting the reference phase from the object phase. Assume a fringe pattern where the fringes are exactly parallel to y-axis so the fringe modulation is a very well defined sin wave. Intensity is defined by amplitude (A_0) multiplied with a $sin(\alpha x)$ term. Because the pattern is exact, the phase value is equal to $\Phi(x, y) = \alpha x$. This equation is a linear but if there is a phase modulation which is related to the phase deformation, then, an extra term will be put into the equation: $\Phi(x, y) = \alpha x + \Delta\phi(x, y)$ and only this extra term carries the object height description. First term introduces the constant tilt on the phase maps and it needs to be removed from the phase maps. Subtracting the two frames from each other removes the tilt and extracts the object topography. This is our final step for image processing and then the phase map is multiplied with a constant to form exact height description of the real object.

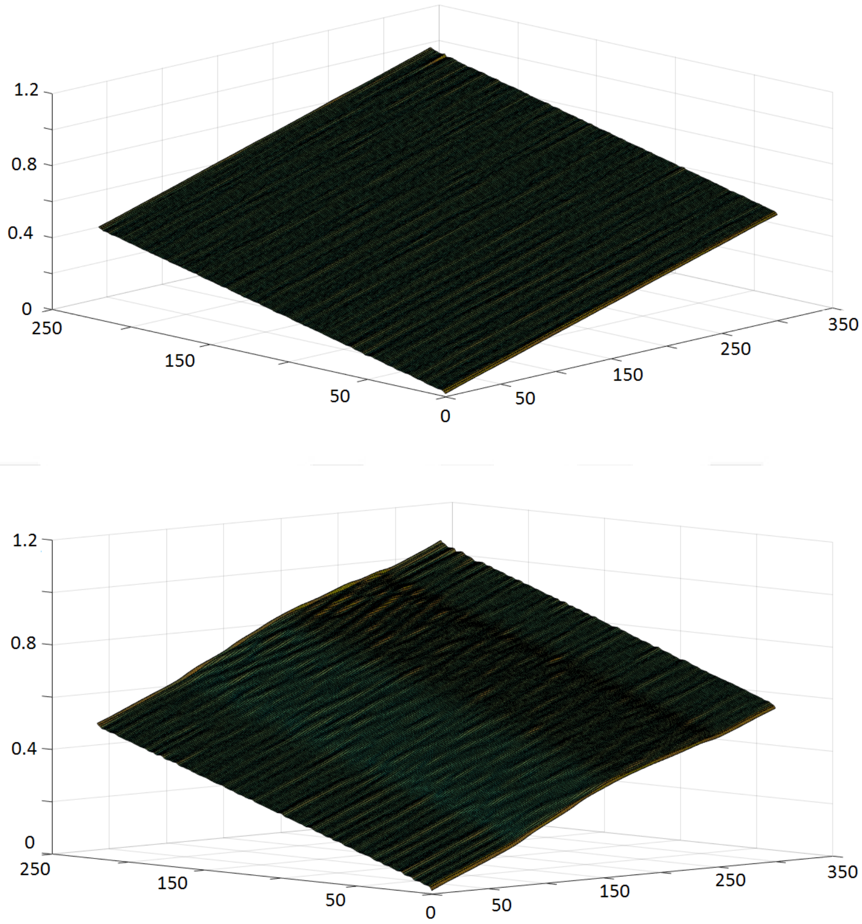

Figure 3.8. Tilted phases of reference and object frames.

4. FOURIER TRANSFORM OPTICAL PROFILOMETRY METHOD

4.1. Introduction

The first technique we implement is named Fourier Transform Profilometry (FTP) (or Fourier Fringe Analysis (FFA)) and it is one of the most powerful methods of non-invasive optical surface profilometry applications. Very-well known first application of Fourier transform method in optical profilometry was done by Takeda *et al.* [76, 77] and since then tremendous amount of research papers have presented various surface topography applications of the technique. Takeda′s Fourier fringe analysis technique was one dimensional and able to analyze one thin slice of the image at a time. Right after Takeda, the technique was extended in to two dimensions and further developed until today [78–80].

In this section, a fiber optic Lloyd′s mirror method is introduced to obtain a structured light pattern and its application to Fourier transform optical surface profilometry. Two separate type of fringes are projected on target object surfaces : single and double mirror Lloyd′s fringe patterns. The intensity distribution of the projected pattern are studied for both mirror configurations and then Fourier Transform Method will be implemented and finally, the formulation of surface height description is derived.

4.2. Fringe Analysis for Lloyd′s Single-Mirror Assembly

Fourier transform analysis basicly depends on Fourier transform of an intensity distribution of the diffraction pattern. Our fringe pattern is sinusoidal so the calculations of the frequency spectrum can be done as like a sinusoidal grating. Figure 4.2 shows diffraction spectra of light from a square wave grating and sinusoidal grating. K.J. Gȧsvik [75] explains the description of diffraction patterns and defines the grating frequency by f_0 and intensity distributions in focal points by arrows. The sinusoidal grating contains the frequencies $\pm f_0$ and 0. Besides, the square wave grating which is presented in Figure 4.2(a) is in fact a sum of sinusoidal gratings of frequencies which are integer multiples of the basic frequency f_0 or it can be called a Fourier series.

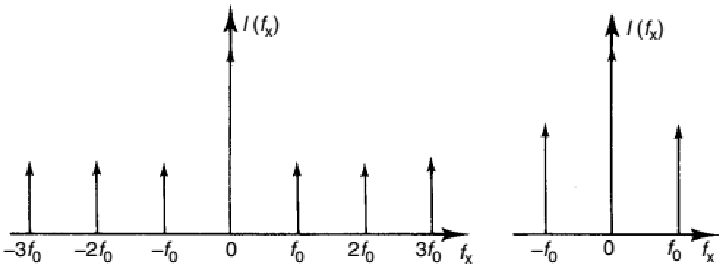

Figure 4.1. Diffraction patterns of (a) square wave and (b) sinosoidal gratings [75].

In Fourier optics, the field $u(x_f)$ in the x_f plane for a single slit can be transferred to Fourier domain using a transmittance function $t(x)$. Considering a light wave given by $u_i(x, y)$ projected on an object surface with a transmittance function $t(x, y)$ the field just behind the object is $u(x, y) = t(x, y)u_i(x, y)$ and the field in the x_f plane is given as ;

$$u(x_f, y_f) = \frac{K}{i\lambda z}\mathcal{F}\{u(x, y)\} \tag{4.1}$$

K is called as the phase factor and λ is the wavelength of the field. This equation gives the Fourier transform of u(x,y) based on Fraunhofer approximation so for a true approximation, the object must be settled far away from the observation plane. If you observe the diffraction pattern from the focal plane of a lens, you may achieve this condition. The intensity of the diffraction pattern is square of the field $I(x, y) = |u(x, y)|^2$. The sinusoidal grating has a frequency spectrum (in 1D) of

$$t(x) = 1 + \cos 2\pi f_0 x \tag{4.2}$$

Using the tranmittance equation, we can derive the field function such as

$$u(x_f) = \int_{-\infty}^{\infty} (1 + \cos 2\pi f_0 x)e^{-i\pi f_x x} dx \tag{4.3}$$

$$u(x_f) = \delta(f_x) + \frac{1}{2}\delta(f_x - f_0) + \frac{1}{2}\delta(f_x + f_0) \tag{4.4}$$

Integrating Equation 4.3 emphasizes that the three delta functions in Equation 4.4 present the three arrows you meet in frequency spectra of the diffraction pattern in Figure 4.2. Now, assume that this sinusoidal grating undergoes a change with a slowly varying function, then this grating is said to be phase-modulated. This phase-modulation broadens the side orders because of this introduced slowly-varying function. Then, the result shows itself on the grating spectrum such as;

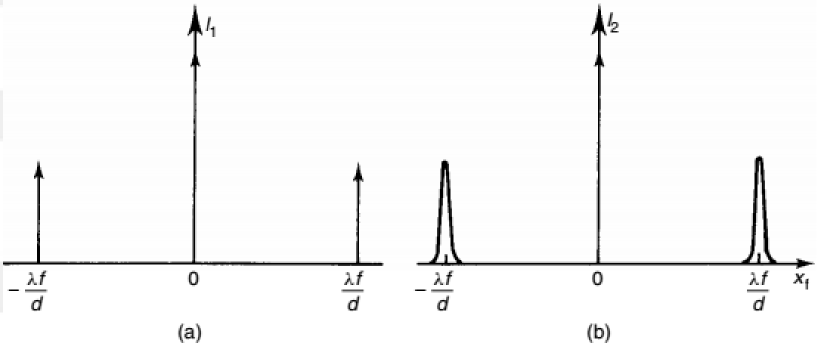

Figure 4.2. (a)Spectrum of a sinusoidal grating and (b) its phase-modulated version [75].

The intensity distribution of the source fringe pattern projected on the target surface is deformed due to the shape and the height of the object. So this deformation causes a modulation on the spectrum and it can be called as phase modulation. An extra parameter "ϕ" is added inside the cosine term in the intensity equation to refer this modulation and the general form of the intensity profile can be defined in Equation 4.5 as

$$I(x, y) = A(x, y) + B(x, y)\cos(2\pi u_0 x + \phi(x, y)) \tag{4.5}$$

The complex form of this equation is given by

$$I(x, y) = A(x, y) + C(x, y)\exp(i(2\pi u_0 x)) + C(x, y)^* \exp(-i(2\pi u_0 x)) \tag{4.6}$$

$$C(x,y) = \frac{1}{2}B(x,y)\exp(i\phi(x,y)) \tag{4.7}$$

$$C(x,y)^{*} = \frac{1}{2}B(x,y)\exp(-i\phi(x,y)) \tag{4.8}$$

$$u_0 = \frac{\delta}{\lambda f}\cos\theta \tag{4.9}$$

One should be careful about the term δ in Equation 4.9. It is not relative to any delta function, in fact it is the definition of distance between the two point sources that are introduced before. To be more relative for our study, a two-point sources interference is calculated instead of a grating pattern that is explained above. The experimental setup of fringe generation and projection will be explained later on and note that, these two point sources are in fact a real optical fiber and its image inside a mirror. Adhering to our experimental setup, the constants in Equation 4.9 are referred such as ϕ is the phase information, δ is the separation between the sources, λ is the wavelength of the light source. Fourier transform of Equation 4.6 is

$$I(u,v) = A(u,v) + C(u-u_0,v) + C^{*}(u+u_0,v) \tag{4.10}$$

The Fourier spectra of $A(x,y)$ and $C(x,y)$ terms in Equation 4.6 are given as $A(u,v)$ and $C(u,v)$ in Equation 4.10 respectively. The carrier frequency is given in u_0 and it is defined as the separation of $C(u-u_0,v)$ and $C^{*}(u+u_0,v)$ with $A(u,v)$. $A(u,v)$ is named as the background information and does not contain any valuable information about the surface profile and the object. The main consideration here is the C side lobes because they have all the required information and one of them is chosen for calculations of object-height distribution. These lobes carry the phase modulation. Filtering one of these side lobes in its spatial frequency domain and then, applying an inverse Fourier transform, the 3D surface topography of the object is obtained. To achieve, the background information A and one of the C terms are filtered by band pass filtering and reduced part of the data is transferred to the origin by the carrier frequency

u_0. Figure 4.3 shows the C peaks position after transformation. A 2D Hanning window is used for this filtering process. Hanning window is applied for filtering the noise from the height information especially if discontinuities and speckles exist on the modulated signal [81].

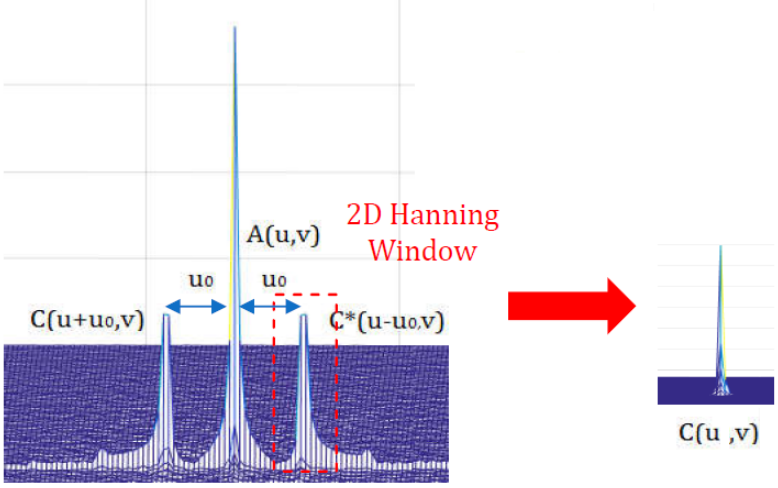

Figure 4.3. Fourier spectra intensity distribution of the fringe pattern, the filtered and centered data peak [82].

After the inverse Fourier transform, a complex function $C(x, y)$ is obtained from the phase information and it is extracted as;

$$\phi(x, y) = \arctan \frac{Im[C(x, y)]}{Re[C(x, y)]} \tag{4.11}$$

Here Im(C(x, y)) and Re(C(x, y)) refer to the imaginary and real parts of the $C(x, y)$ function. Result of Equation 4.11 is a wrapped phase distribution and it has discontinuities with 2π phase jump because of the nature of arctangent function. The phase is wrapped between $-\pi$ to π and it is inevitable to make it unwrapped for a successful phase distribution. We used a phase unwrapping algorithm to make the phase continuous and explain its details in Phase Extraction and Phase Unwrapping part. Now, considering our intensity distribution of fringes across the surface we have an intensity Equation 4.12. This intensity equation carries the modulation phase inside because of the deformed fringe patterns on the object surface. In Equation 4.12, θ is defined as the illumination angle, λ is the wavelength of our laser source, f is the distance between the optic fiber end and object surface, I_0 is the intensity value of one fiber and δ is the separation between fiber tips. Here, $z(x, y)$ term is the height description of the each point on the surface.

$$I(x,y) = 2I_0[1 + \cos(2\pi\frac{\delta}{\lambda f}(x\cos\theta - z(x,y)\sin\theta)] \tag{4.12}$$

The first term inside cosine in Equation 4.12 is carrier frequency term. If the fringes are projected on a plane surface (without target object), then the phase belongs to carrier frequency can be gained from this term. After the object is placed on the plane surface, the total phase will be a superimpose of the phase caused by the carrier frequency and the modulation phase. The second term inside cosine is crucial because it carries object height information and using a suitable filtering algorithm extracts the modulation phase from the total phase distribution. Filtering and centering of C side lobe help to extract the modulation data from the intensity matrix. Finally, the object height description is given in Equation 4.13

$$z(x,y) = \frac{\lambda f}{2\pi\delta\sin\theta}\phi(x,y) \tag{4.13}$$

Surface height of the object is directly varies with the modulation phase via a constant including optical geometry related parameters.

4.3. Fringe Analysis for Lloyd′s Double-Mirror Assembly

Double Mirror Lloyd′s assemblyhas been introduced in Lloyd′s Setup section. The pattern is constructed from four point sources (in fact one fiber and its images in the flat mirrors) which are labeled as S1, S2, S3, and S4, as shown in Figure 3.2. Figure 4.4 illustrates the Fourier spectrum peaks of the double-mirror interference pattern. The maximum peak at the origin is erased so as to show the other phase peaks clearly. The pairing of sources (1-2) and (3-4) produces one vertical interferogram, which has an intensity distribution in the D sidelobe. The pairing of sources (2-3) and (1-4) gives a horizontal interferogram with an intensity distribution in the C sidelobe. Two sets of different diagonal interferograms, whose intensity distributions in the spatial frequency domain are in sidelobes E and F, are formed by the pairing of sources (1-3) and (2-4). The final generated pattern superimposes these six interferograms.

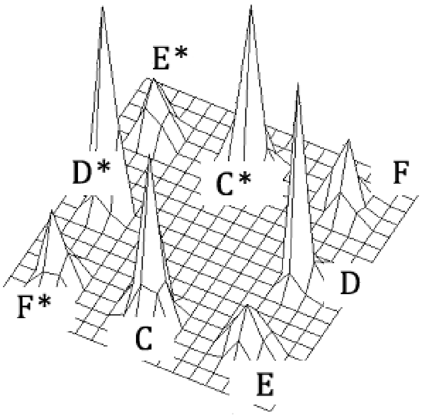

Figure 4.4. 2-D Fourier spectrum of the non-deformed fringe pattern without the zero frequency term [82].

The mathematical description of the intensity distribution for the four-point optical sources is given as

$$\begin{aligned} I(x,y) = 2I_0[2 + 2\cos(2\pi\frac{\delta}{\lambda f}(x\cos\theta - z(x,y)\sin\theta) \\ +2cos(2\pi\frac{\delta}{\lambda f}y) \\ +cos(2\pi\frac{\delta}{\lambda f}(x\cos\theta - z(x,y)\sin\theta + y) \\ +cos(2\pi\frac{\delta}{\lambda f}(x\cos\theta - z(x,y)\sin\theta - y)] \end{aligned} \tag{4.14}$$

For Fourier analysis, above equation can be written in complex form such as

$$\begin{aligned} I(x,y) = A(x,y) + C(x,y)\exp[i2\pi u_0 x] \\ +C^*(x,y)\exp[-i2\pi u_0 x] \\ +D(x,y)\exp[i2\pi u_0^{'} y] \\ +D^*(x,y)\exp[-i2\pi u_0^{'} y] \\ +E(x,y)\exp[i2\pi(u_0 x + u_0^{'} y)] \\ +E^*(x,y)\exp[-i2\pi(u_0 x + u_0^{'} y)] \\ +F(x,y)\exp[i2\pi(u_0 x - u_0^{'} y)] \\ +F^*(x,y)\exp[-i2\pi(u_0 x - u_0^{'} y)] \end{aligned} \tag{4.15}$$

where $u_0^{'} = \frac{\delta}{\lambda f}$. Fourier transform of the recorded intensity distribution

$$\begin{aligned} I(u,v) = A(u,v) + C(u-u_0,v) + C^*(u+u_0,v) \\ +D(u,v-u_0^{'}) + D^*(u,v+u_0^{'}) \\ +E(u-u_0,v-u_0^{'}) + E^*(u+u_0,v+u_0^{'}) \\ +F(u-u_0,v+u_0^{'}) + F^*(u+u_0,v-u_0^{'}) \end{aligned} \tag{4.16}$$

All terms in Equation 4.16 are the Fourier transforms of the corresponding terms in Equation 4.15, respectively. The derivation of the intensity distribution of four-point source can be found in [14]. The process after this transformation is quite similar to the fringe analysis that we introduced before. The sidelobe $C(u-u_0,v)$, which contains the phase data, is isolated and then transferred to the origin. The remaining parts are unnecessary and eliminated by bandpass filtering. The surface topography of the target object is gained after the inverse Fourier transform is applied to the data. The phase unwrapping algorithm is used to make the phase information continuous in the event there are discontinuities present.

4.4. Experimental Setup of Fourier Transform Profilometry (FTP)

The Lloyd′s mirror experimental setup is shown in Figure 4.5. A 35 mW HeNe laser source with a wavelength of 632.8 nm is launched into a single-mode optical fiber. At the other end, the jacket of the fiber is removed, and the bare fiber is carefully placed on the mirror. A piece of a clean silicon wafer is used as a regular mirror. Using a mirror with a very narrow glass thickness is especially important in the double-mirror assembly to avoid the formation of inner images inside the mirrors when two glass mirrors are used, so a piece of silicon wafer can easily cover that requirement. These inner images distort the fringe pattern projected on the screen. In addition, the reflectance from the polished side of the wafer is high enough to construct the visible fringe pattern on the object surface.

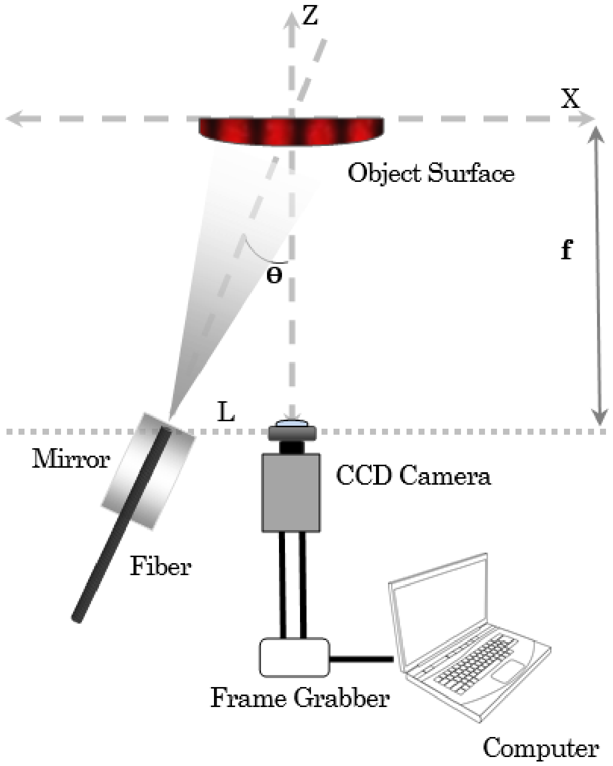

Figure 4.5. Sketch of Lloyd′s Mirror experimental setup [82].

The optical configuration shown in Figure 4.5 is selected due to its simplicity, reliability, and ease of use [83]. In the experimental setup, the optical axis of the CCD camera is positioned perpendicularly to the screen. A lens of 25 mm focal length is attached to the CCD camera to take better-quality images. The optical fiber is placed on the mirror, and the illumination angle θ is fixed at approximately 4-5° so as to maximize the magnitude of the reflected light toward the camera and to reduce the shadowing effects. The distance between the camera and the object surface is fixed around 245 cm. In the single Lloyd′s mirror assembly, the direction of the interference pattern depends on the experimenter′s choice. When the mirror is placed parallel to the surface of the optical table, the fringe pattern is constructed horizontally on the target object; on the other hand, the interference pattern is generated vertically on the screen when the mirror is placed perpendicular to the optical table. Fringes constructed by either single− or double−mirror assemblies are then projected from the interferometer onto the object without the need for large collimating optics. We use a frame grabber card to receive and digitize the signal obtained from the CCD camera, which is then transferred to the computer. The positions of the optical fiber and its images are presented in Figure 4.6. The fiber is fixed parallel to the mirror(s) surface(s) to have discrete fringe spacing. For the double-mirror assembly, the fiber is carefully placed in the v-groove, which is formed by two mirrors adjusted orthogonally with each other, as shown in Figure (b).

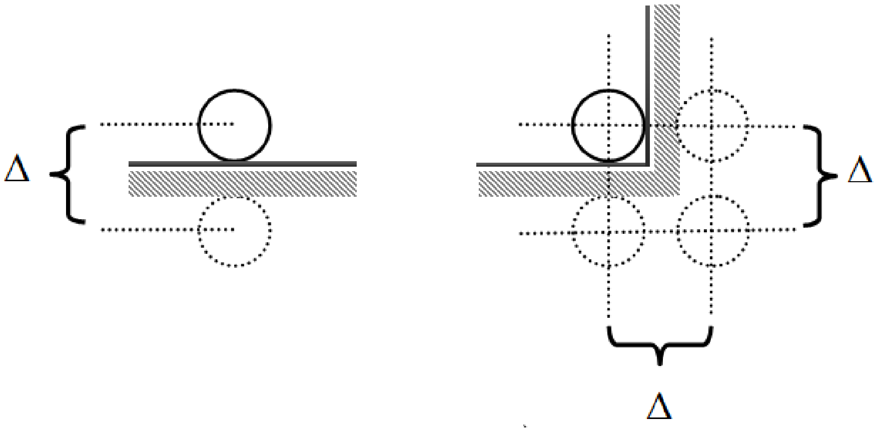

Figure 4.6. Positions of the optical fiber and Lloyd′s mirrors. (a) Fiber with single mirror. (b) Fiber with double mirrors. [82].

Square-shaped fringes are obtained through the interference of four wavefronts. In the double-mirror assembly, the tilting angle between these two mirrors is simply measured with a goniometer, and the angle is adjusted approximately 91°. Additionally, this angle can be changed by tilting the mirrors to form different constructive interference patterns. The size and the shape of these interference dots will vary due to the tilting angle between two mirrors. For a perfectly square bright and dark pattern design, the mirrors are carefully aligned to make them absolutely perpendicular with each other. The core-to-core distance between the fiber and one of its images is approximately 110 μm. After obtaining the images of the fiber Lloyd′s mirror assemblies, the Fourier transform technique given in the above section is implemented for processing the images.

4.5. Results

Figure 4.7 presents single mirror (a) and double mirror (b) Lloyd′s fringes. The fringe patterns are projected on the plane surface and both of the pattern frames are cut in the same size. The intensity of the fringes fades from the center to the far edges because of the optic fiber positioning the maximum intensity area on the plane surface is the point right across the optic fiber tip. This fading is not a restriction for our calculations because the algorithm that is used for phase extraction only considers phase modulation.

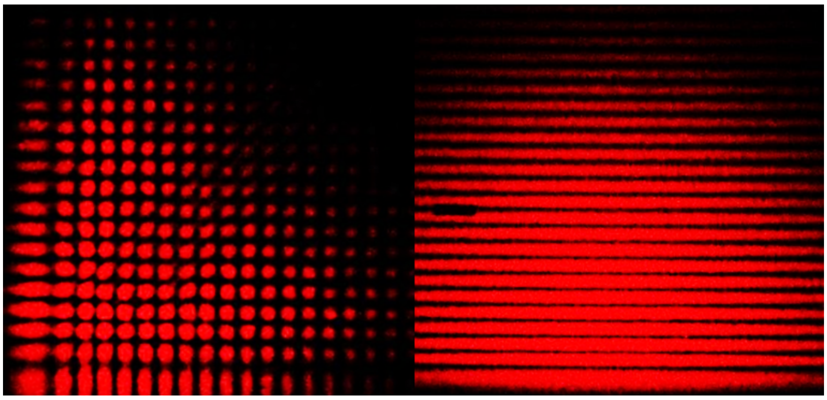

Figure 4.7. Positions of the optical fiber and Lloyd′s mirrors. (a) Fiber with single mirror. (b) Fiber with double mirrors. [82].

The periodicity of the projected fringes are very fine and the bright and dark fringes are easy to distinguish. Double mirror fringe pattern is a superimposing of two single mirror fringe patterns. In other words, it is easy to visualize that left pattern is constructed by interlaced of two right patterns which one of them is 90° degrees tilted. The intensity value of the each bright fringe in the single mirror fringe pattern is given in pixel in the following figure. We call the highest intensity fringes as sub central fringes because they are formed very close to the point where fiber′s tip is directed. Because of the Gaussian distribution of the laser light, some fringe′s intensity is very close to each other in this range. The fringe pattern also indicates that the frequency of the fringe is constant and it does not affect by external factors.

Fringe pattern intensity matrixes for double and single mirror are given in Figure 4.8. Both interference patterns distribute the laser light in a similar way. FTP method requires no fringe order assignments or fringe center determination and does not require interpolation between fringes because it gives height distribution at every pixel over the entire fields.

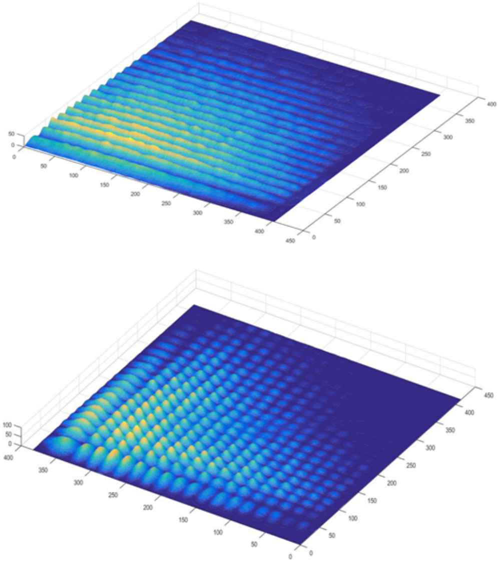

Figure 4.8. Intensity distribution of the fringe patterns for single mirror and double mirror Lloyd′s assembly.

A test object is carefully selected for ease of comparison of its real surface profile with our experimental results. The test object used is a 19 cm × 15 cm piece of white paper. The paper is placed on the screen in a proper way to form a cambered figure. The approximate height of the camber is measured as 3.62 cm.

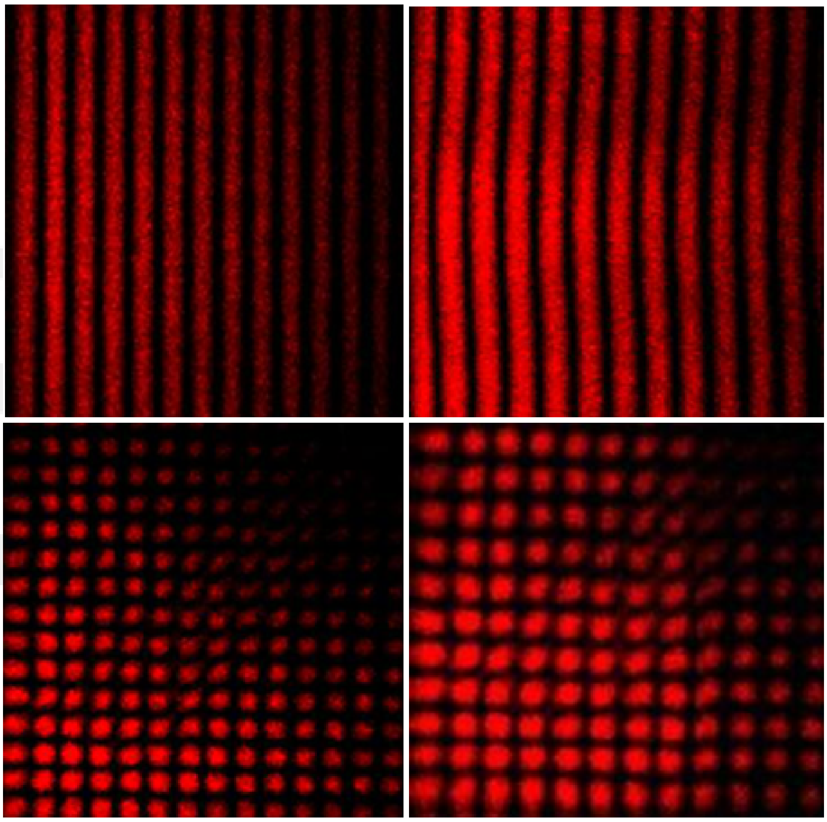

Figure 4.9. Images of nondeformed fringe patterns (left) and deformed fringe patterns (right)

Figure 4.9 represents the single– and double–mirror fringe patterns and their respective deformed fringes. The fringe patterns are generated using the configurations explained above. In the single–mirror assembly, the fringes are projected horizontally onto the object surface. In the double–mirror assembly, the desired fringe pattern is formed by the superimposition of vertical and horizontal interference patterns, which consists of square–shaped fringes. Considering the size of the object and the area that the object overspreads on the screen, the decrease in the intensity of the interference pattern in the chosen area did not cause any significant errors on the reconstructed image. In Figure 4.10 , the reconstructed cambered paper is shown for the single

Lloyd′s mirror. The height of the reconstructed object is calculated as approximately 3.83 cm for the single Lloyd′s mirror assembly. The height of the reconstructed surface is approximately 3.90 cm for the double-mirror assembly. Also, the reconstructed object surface is uniform and smooth for both assemblies.

In Figure 4.11 the real object and reconstructed object dimensions for the single- and double-mirror assemblies are compared. The calculated error between these two setups is less than 3%.

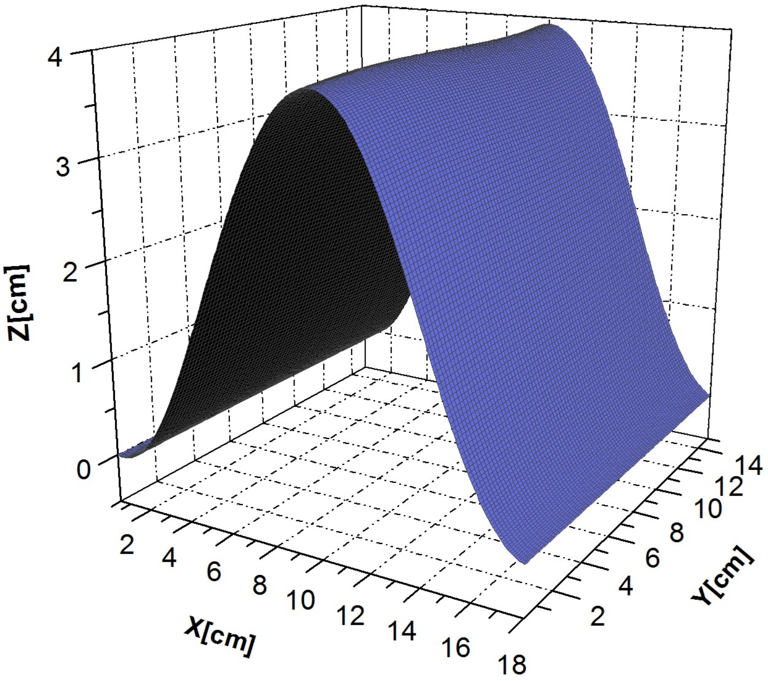

Figure 4.10. Reconstructed surface of the object for the single Lloyd′s mirror assembly

The error between the peaks of the results of the single-mirror assembly and the surface profile of the real object is less than 6% of the object depth. This implies that the reconstructed dimensions of the cross section of the images are quite similar to the real object dimensions.

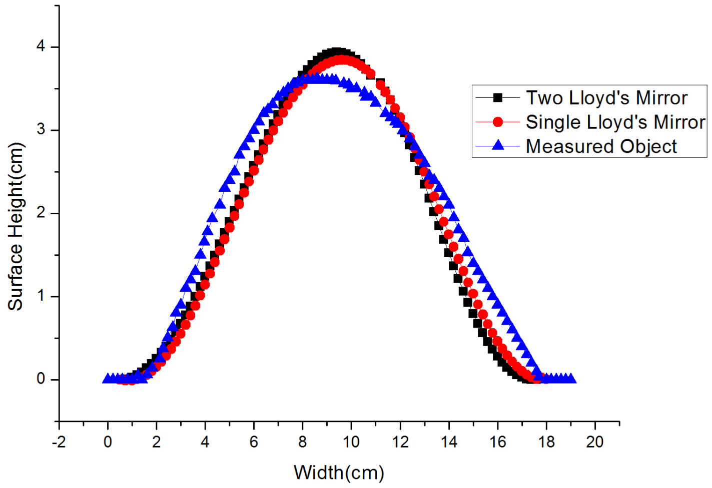

Figure 4.11. Comparison of reconstructed and real object cross sections.

4.6. Calculations

Every fringe projection system has a unique resolution, the number of fringes that are produced by the optical system determines the sensitivity and the projection area of projected fringes. Our calculation is based on single mode optical fiber with a fixed angle of illumination. This angle κ depends on the numerical aperture of the optic fiber and the refractive index of the medium of the optical system (which is air in our case). NA is the numerical aperture of the optical fiber and its relation with illumination angle κ is;

$$\kappa = \arcsin(\mathrm{NA}) \tag{4.17}$$

In literature κ is given as 0.14 generally for a single mode optical fiber. So the number of fringes in the projected fringe pattern can be calculated by the following equation;

$$N \leq \frac{\delta\kappa\sqrt{2}}{\lambda} \tag{4.18}$$

δ is assumed to be 110 μm and λ is 632.8 nm, so the calculated fringe number is approximately ;

$$N \leq 24.3 \tag{4.19}$$

which is in accordance with our results. The number of fringes that are projected on the plane surface is counted and it is around 24 from the maximum intensity fringe to the most faded one. Fringe spacing is given as;

$$P_0 = \frac{\lambda f}{\delta} = 14mm \tag{4.20}$$

System resolution R is a ratio of fringe spacing and viewing angle. The captured image of the fringe pattern is converted to gray scale and the difference between the maximum and the minimum of gray levels of the pattern is extracted from the intensity matrix. The difference of gray level is 82 between the peak and the valleys of the fringe pattern. Using this constant and viewing angle θ;

$$R = \frac{P_0}{82 \cdot \sin(5^\circ)} = 0.1958mm \tag{4.21}$$

4.7. Discussion

When our Lloyd′s mirror setup is compared with optical profilometers employing fiber optic couplers, our experimental setup is shown to be more effective and robust. It does not require any careful alignment or rotation of the fiber ends for maintaining the polarization, which is a crucial parameter for achieving better-quality interferograms. Therefore, our setup is immune to a decrease in the resolution of the system due to poor fringe visibility. When our Lloyd′s setup is compared with interferometers with multicore optical fibers or fiber couplers, our experimental setup provides a much simpler and quicker way of alignment to obtain the deformed fringe patterns for image processing. In addition, the core separation is fixed in a multicore optical fiber, which makes constant fringe spacing, whereas the fringe spacing easily can be adjusted in our setup through displacing the fiber from the mirror. In this study, it is proved that the Lloyd′s mirror technique can be used to generate surface profiles of large objects. External factors greatly affect the outcomes of multicore fiber systems and profilometers with optical couplers. They are highly sensitive to ambient temperature. Thermal fluctuations may change the orientation of the fiber ends, and fiber shrinkage and expansion may affect the distance between the cores and the distance of the fiber ends with respect to each other. This results in change in the interference pattern, which may cause loss of fringe pattern and decrease in the resolution of the system. On the other hand, Lloyd′s technique is almost immune to external temperatures since the interference is constituted by the fiber and its image formed by the mirror. In addition, the effects of differences between material characteristics such as fiber thermal properties are eliminated using Lloyd′s technique. External vibrations, tilting, or bending of the fiber, where this fiber structure is path-length dependent, can affect the interference formed by multicore fibers and fiber couplers and may introduce failures in the interference pattern. Furthermore, the fiber optic Lloyd′s assembly proposed in this work overcomes the issue of fiber nonidealities such as different core radii, refractive index profiles, and cylindrical geometry, which may affect the coupling and power transfer between cores [84]. Lloyd′s mirror assemblies do not include any high-cost equipment such as optical fiber coupler, alignment tools, or lenses. A regular single-core fiber can be used for the process without the need for highcost manufacturing associated with multicore fibers.

Multicore optical fibers make a fringe projection system compact and stable [14]. Our fringe projection system using Lloyd′s mirror produces a high-quality fringe pattern with better practicality and compactness. The surface topography of the target object is obtained through phase modulation of the fringe pattern. The FTP technique is employed to process line- and square-shaped interference patterns.

It is demonstrated that Lloyd′s technique with both single and double mirrors can be used in Fourier transform profilometry. The double-mirror setup enables us to process more sophisticated surface profiles because of the superimposition of vertical and horizontal interference patterns. Changing the tilting angle of the double mirrors may give more than one type of fringe pattern, which may provide specific FTP processes for specific applications.

Sources of errors in the single- and double-mirror setups are quite similar. Mainly, the degree of flatness of the mirror is an important factor since better flatness reduces undesired reflections. The tilting angle of the two mirrors has crucial importance in forming the squared-shaped constructive interference pattern. If the mirrors are not perfectly orthogonal to each other, and the fiber is not precisely positioned equally to each of the two mirrors, the fringe spacing may not be discrete enough. Hence, the single-mirror setup is a better approach for the construction of discrete fringe spacing. This is one of the reasons behind the slight difference between the results of the surface profile measurements of single and double Lloyd′s mirror setups. However, this error ratio is considerably small, below 3 % so the two techniques nicely coincide. The main source of error, which accounts for the difference in the results between Lloyd′s mirror systems when compared with the real object profile, comes from the limited accuracy of using a vernier caliper to measure the surface profile of the real object. However, the error ratio between the single mirror and the real object profile is still below 6%. In addition, using mirrors with good reflectivity decreases the error ratio, since it generates the interference pattern with a high fringe contrast, which improves image quality. The angle between the camera axis and fiber axis is adjusted below 5° to prevent signal fades due to shadows on the object, which cause phase unwrapping problems. However, such a choice of small viewing angle may be a source of error since it jeopardizes the resolution of the system.

The only challenges of the fiber optic Lloyd′s mirrors methods might be the need for significant care in handling and placing the stripped ends of fibers and the need to carefully adjust the angle between the two perpendicular mirrors in the double-mirror assembly. Since the assembly is set up once, and everything is clamped down once and for all at the beginning of the experiments, no further adjustments are required during the experiments. The system remains robust and immune to environmental changes. Apart from this, it is a fact that there is a fading portion of the fringe pattern that is inherent to Lloyd′s mirror configuration. However, a high degree of symmetry is obtained over a relatively large area of the structured light pattern, which allowed us to accurately process images in single- and double mirror configurations.

4.8. Conclusion

This experimental setup demonstrates for the first time the use of Fourier transform profilometry (FTP) by a fiber optic Lloyd′s mirror assembly in constructing good-quality interference patterns at a relatively low cost. These patterns are less sensitive to external disturbing factors such as ambient temperature and vibrations. Our preliminary results from the reconstructed surface topography, using single and double-mirror assemblies, give a small error, which implies that our proposed technique for FTP is promising. Pattern improvement may be possible by using high-quality mirrors with good reflectivity and better flatness. Finally, since the proposed technique is flexible and easy to configure, it enables us to develop unique setups for other specific applications and 3D shapes of more complicated objects.

5. PHASE STEPPING OPTICAL PROFILOMETRY METHOD

5.1. Introduction

Our second technique is called as Phase–stepping (or Phase–shifting) Interferometry (PSP) and it considers analysis of multiple frames of deformed fringe pattern with a controlled phase shift between whole frames. All types of phase stepping interferometers include an image capturing unit (that can be a CCD camera, a photodiode or a detector), a phase generation step where a fixed amount of phase difference is achieved either continuously (phase-shifting) or in discrete steps (phase–stepping), then an image analysis algorithm which analyzes all the frames that are captured from discrete steps and extract the phase data among all.

Phase shifting (or stepping) techniques can be very diverse and a big portion of the research in phase shifting profilometry techniques depend on multiple steps (3, 4, 5 or more) phase shifting with fixed phase amount [85]. An unknown amount of phase shift in multiple stepping is another used technique [86]. Digital light projectors (DLP) are mostly used as fringe projectors in PSP techniques, while researchers also implement wavelength –tunable diode lasers [87]. Phase stepping technique can also be combined with common path Fizeau interferometer and take measurements in real time [88]. Implementing multiple wavelengths in the optical system and simultaneously phase shifting is done by Fan *et al.* [89] with a high precision. A similar but not identical study considers with one color fringe pattern encoded with two sinusoidal patterns and one rectangular pulse pattern those are projected by a DLP project and recorded by a CCD camera [90].

In this work, a fiber optic Lloyd′s mirror method [82] is employed for the first time to obtain a structured light pattern in a phase stepping optical profilometry technique for three dimensional noninvasive shape measurements. This work is an extension of previous work (in chapter 4) where the Lloyd′s mirror technique is used by Fourier transform optical profilometry (FTP). One of the main advantages of the FTP algorithm is that it only needs one frame of the deformed interferogram to process the surface height of the target object. It works quite well without the need of any referencing frame and contains only minor errors. However, the FTP still has some drawbacks, especially the sharp discontinuities and shadow areas that contribute to increased error. The FTP also has some difficulties in measuring nonfullfilled scenes. In comparison, the phase stepping algorithm (PSP), which is another alternative powerful technique among the image processing algorithms, does not suffer from nonfullfilled scenes [83]. The main error sources for the PSP are the external vibrations and the variations in the ambient temperature. The Lloyd′s mirror technique introduced in this work eliminates these errors. Processing the structured light pattern obtained from the Lloyd′s technique supplies a powerful method, which is almost immune to the thermal fluctuations and environmental vibrations. The method demonstrated in this work provides more practical and precise results at lower costs when compared to the other fringe projection methods.

5.2. Fringe Analysis for the Three-Step Phase Stepping Fiber Optic Lloyd′s Mirror Configuration

The projected fringe pattern is produced by a fiber optic Lloyd′s interferometer. A mirror and an optical fiber are used to form a grid–like light pattern on a target surface. This pattern is the result of the constructive and destructive interference of the photons emitted from a coherent monochromatic point source held near the surface of an ordinary mirror or a flat reflecting surface. The mirror–fiber assembly corresponds to a two–beam interferometer and is similar to that of the Young′s double–slit experiment. As illustrated in Figure 3.1, the light beam emitting directly from the optical fiber is referred to as the real point source. The image in the mirror is referred to as the virtual source. Both the real and virtual point sources produce a structured light pattern. The fringe interference is explained in Fringe Analysis for Lloyd′s Single-Mirror Assembly part in detail. When working with small objects or objects with fine details, the number of fringes projected on the object becomes an important parameter. To address this, one may adjust δ in order to accommodate the desired number of fringes with a certain fringe separation on the topography in concern. This allows it to be easily employed in phase stepping profilometry. As seen in Figure 5.1, the fiber optic Lloyd′s mirror assembly is placed on a movable mechanical stage. This allows moving the whole system in one direction to produce the consecutive interferograms for processing in the phase-shifting algorithm. The mechanical stage includes a fine adjustment to shift the light pattern precisely. This satisfies the requirement to maintain an exact phase difference between each consecutive frame. The number of frames depends on the chosen phase shifting algorithm. The constructed fringe pattern illuminates the object′s surface and moves on the surface with certain phase steps while a CCD camera captures each deformed pattern. The captured images are then processed to gain the required phase information. The wrapped phase information is unwrapped using a suitable unwrapping algorithm. Finally, the surface height distribution of the target object is acquired.

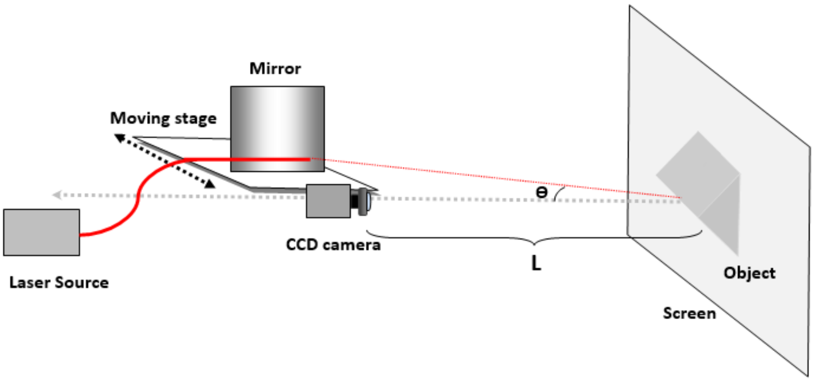

Figure 5.1. Sketch of the Lloyd′s mirror phase stepping profilometry experimental setup.

In the experiments, a three–step phase stepping algorithm is used and three successive images are taken. The deformed fringe pattern is compared to that of the undeformed (reference frame) one to build a phase matrix. The surface profile of the object is calculated from this phase map.

Multi–step phase shifting (or stepping) algorithms consider more than one light source and the derivation of the intensity distribution of the light pattern will depend on the number of light sources. Here, a general derivation will be given for intensity distribution (and further information about two and more light sources) can be gained from the thesis study of (Lewis, 1993) [91].

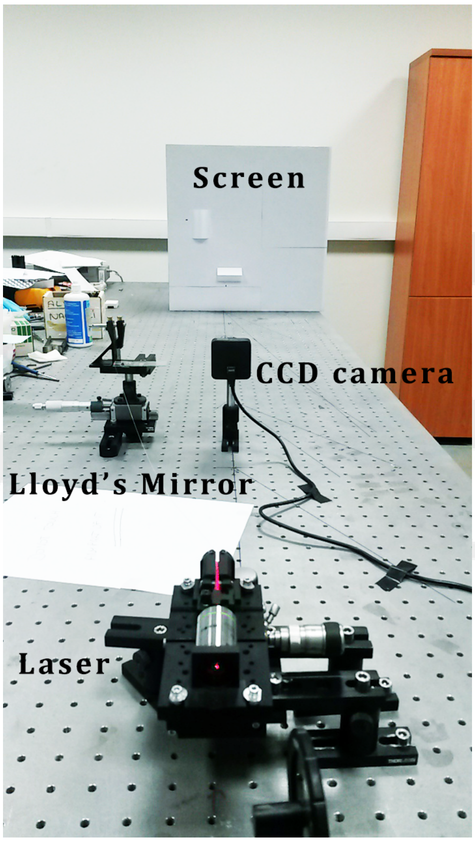

Figure 5.2. Lloyd′s mirror PSP experimental setup on optic table.

The fiber optic Lloyd′s mirror experimental setup photo is in Figure 5.2. CCD camera is placed in front of the plane screen to minimize the shadings and mirror and the fiber is positioned right across the camera with a very small angle to the camera axis. Micrometer stage is placed under the mirror & optic fiber set so the whole part can be moved altogether.

Figure 5.3 belongs to the optic fiber and the mirror. Here, the real positioning of the mirror is perpendicular to the optic axis so the fringes projected on plane screen will form perpendicular to the optic table axis.

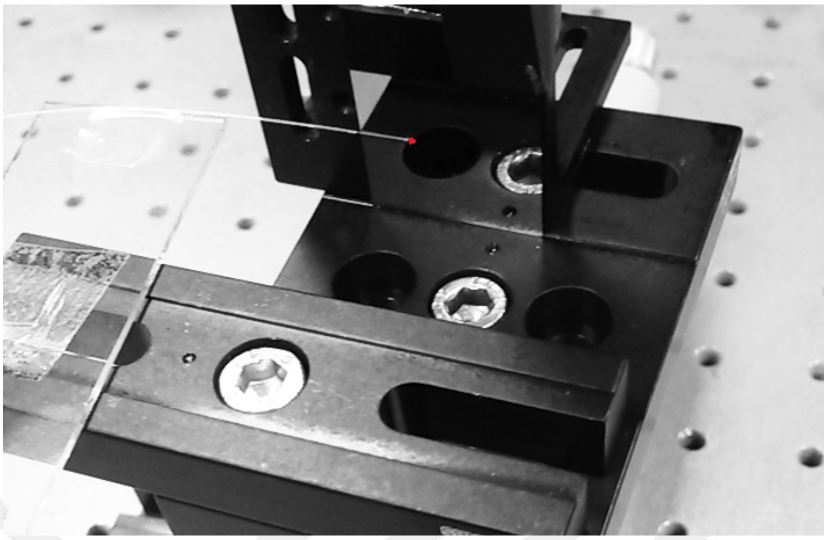

Figure 5.3. Mirror and optic fiber positions.

Intensities of the real fiber and its virtual image are assumed to be equal and both sources are mutually coherent. The mathematical description of the intensity distribution of the fringes, which are projected on the screen, is given as

$$I(x,y) = 2I_0[1+\cos(A(x\cos\theta - z(x,y)\sin\theta)] \tag{5.1}$$

where A is ;

$$A = 2\pi\frac{\delta}{\lambda L} \tag{5.2}$$

where A is a constant, δ is the separation distance between the real and virtual fiber cores, λ is the laser wavelength,L is the displacement between the optical fiber tip and the object$'$s surface. (x,y) describe the chosen pixel, from which the height distribution z(x,y) is calculated in the phase stepping algorithm. This pattern is projected onto the object surface with an angle θ, which may change slightly during the phase shifting process. It is noted though that such a slight change in the angle is very small and can be ignored during the phase mapping calculations. I_0 is the light intensity of a single core. The transfer functions for the intensity distributions of the interferometric frame patterns with a precise phase shift of $\pi/2$ are given with the following equations:

$$\begin{aligned} I_1 &= 2I_0(1+\cos(Ax\cos\theta - Az\sin\theta)) \\ I_2 &= 2I_0(1+\cos(Ax\cos\theta - Az\sin\theta + \frac{\pi}{2})) \\ I_3 &= 2I_0(1+\cos(Ax\cos\theta - Az\sin\theta + \pi)) \end{aligned} \tag{5.3}$$

These intensity equations can be written also in the form of;

$$\begin{aligned} I_1 &= 2I_0(1+\cos(Ax\cos\theta - Az\sin\theta)) \\ I_2 &= 2I_0(1-\sin(Ax\cos\theta - Az\sin\theta)) \\ I_3 &= 2I_0(1-\cos(Ax\cos\theta - Az\sin\theta)) \end{aligned} \tag{5.4}$$

Then taking the difference of the subsequent intensity values;

$$\frac{I_2 - I_3}{I_2 - I_1} = \frac{\cos(Ax\cos\theta - Az\sin\theta) - \sin(Ax\cos\theta - Az\sin\theta)}{-\sin(Ax\cos\theta - Az\sin\theta) - \cos(Ax\cos\theta - Az\sin\theta)} \tag{5.5}$$

Now $\sin(x)+\cos(x) = \sqrt{2}\cos(x-\pi/4)$ and $\sin(x)-\cos(x) = \sqrt{2}\sin(x-\pi/4)$ are used (for further information check [92]). Intensity function can be written ;

$$\begin{aligned} \frac{I_2 - I_3}{I_2 - I_1} &= \frac{\sin(Ax\cos\theta - Az\sin\theta - \pi/4)}{\cos(Ax\cos\theta - Az\sin\theta - \pi/4)} \\ &= \tan(Ax\cos\theta - Az\sin\theta - \pi/4) \end{aligned} \tag{5.6}$$

Here the additional term $\pi/4$ can be removed because during phase shifting we do not need the starting phase amount. It is erased and the z value can be derived from the above equation such as;

$$\phi(x,y) = \arctan(\frac{I_2 - I_3}{I_2 - I_1}) = A(x\cos\theta - z(x,y)\sin\theta). \tag{5.7}$$

Using Equation 5.7, the depth map of the target object is obtained from the following expression:

$$z(x,y) = \frac{Ax\cos\theta - \phi(x,y)}{A\sin\theta} \tag{5.8}$$

5.3. Experimental Setup for Phase Stepping Profilometry(PSP)

The experimental setup used for the phase stepping profilometry is shown in Figure 5.2. A 15 mW He–Ne laser source with a wavelength of 632.8 nm is launched into a single-mode optical fiber. The cleaved distal end of the single–mode optical fiber is carefully placed on an ordinary flat mirror to form a perpendicular fringe pattern on the far field. The fiber optic Lloyd′s interferometric assembly is placed on a movable translational stage with a mounted micrometer. This allows moving the whole fiber–mirror assembly back and forth using the mounted micrometer. In the experiments, a piece of clean and unscratched silicon wafer is selected for use as a regular mirror. Even though the reflection is not as high as a regular mirror, this selection was preferred since it provides good flatness. A CCD camera is used to capture the light intensity of the fringe pattern. The CCD camera is directly placed in front of the screen while the moving stage is placed coplanar with the CCD camera with an angle θ to the camera axis. The angle between the optical fiber tip and the camera axis is referred to as the illumination angle (θ). This angle is adjusted to be approximately 8° to maximize the magnitude of the reflected light toward the camera and to reduce the shadowing effects. The distance between the CCD camera and the object surface is fixed to be around 120 cm. The stage′s position is changed via adjusting the micrometer by a required amount. This allows the fringes to be shifted on the screen in accordance with a chosen reference point. After capturing the first image, the second and third images are taken by introducing a $\pi/2$ phase shift.

The purpose of our work is to demonstrate Lloyd′s assembly in phase stepping since it is capable to overcome thermal and vibrational fluctuations. It should be noted that manual adjustments of an ordinary mechanical microstage cannot ensure exact $\pi/2$ phase shifts between the interference patterns, thus introducing unavoidable errors in the constructed phase map. We attempted to get the least error in shifts by ensuring in MATLAB that the difference between the first nonshifted image and the 2π phase–shifted image is minimal. One way to overcome or minimize phase errors in the phase shift is to make use of the three–step phase shifting methods described by Wang *et al.* and Deng *et al.* [93, 94]. The fiber and mirror are kept fixed to each other during the fringe shifting process to maintain a robust distance between them. The distance between the fiber core and the virtual image core is approximately 130 μm. Finally, the camera is connected to a PC via a USB port and the captured images from the CCD camera are processed using MATLAB software. The direction of the required fringe pattern is flexible and left up to the experimenter′s choice. The Lloyd′s mirror can provide horizontal or vertical fringe patterns by holding the fiber–mirror assembly horizontal or vertical. The fiber optic Lloyd′s assembly is kept vertical to provide a vertical fringe pattern. One may rotate the whole assembly to get a desired fringe pattern at the far field, such as horizontal, vertical, or tilted fringe patterns. Further information about the fiber optic Lloyd′s mirror setup can be found in [14].

5.4. Results

Several objects with different shapes and profiles are studied and a few of them are presented here. Some objects are built from white cardboard and some others are made from Styrofoam. White objects are chosen in order to maximize the reflection of the light from the surface. The first object is a triangular prism and the deformed and undeformed fringe patterns of the triangular prism are given in Figure 5.4. As a preprocessing step, the images are converted from RGB to gray scale and a Gaussian filtering followed by a denoising filter are applied to the images. Real object photo and captured deformed fringe pattern photo are given in Figure 5.4.

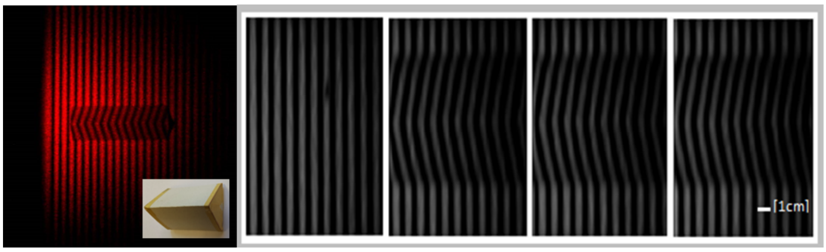

Figure 5.4. Undeformed and deformed consecutive fringe patterns for triangular prism.

The handmade cardboard triangular prism is measured by calipers and has the dimensions 41.15 mm × 57.1 mm × 50.2 mm, height, width, length, respectively. The reconstructed triangular prism is given in Figure 5.5. The reconstructed object dimensions for the height and width are 40.06 and 56.83 mm, respectively.

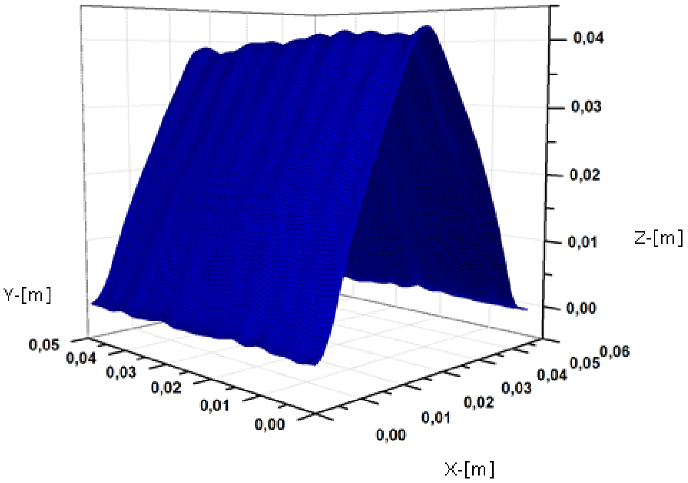

Figure 5.5. Reconstructed triangular prism for Three Step Phase Stepping using the fiber optic Lloyd′s Mirror Assembly.

Our real shape was not a perfect triangular object showing some small variations throughout the surface. For this reason, we could only measure the end face of the triangular object. We have assumed that the real object′s profile map is in the characteristics of the end face (see black curve in Figure 5.6 and is unchanged throughout the whole triangular topography. A comparison of the real and constructed object dimensions of the triangular prism is plotted in Figure 5.6 and the amount of the error differences along the width of the triangle is given in the bottom plot of Figure 5.6. The maximum root–mean–square (rms) error for the whole surface is calculated to be approximately 0.2 mm.

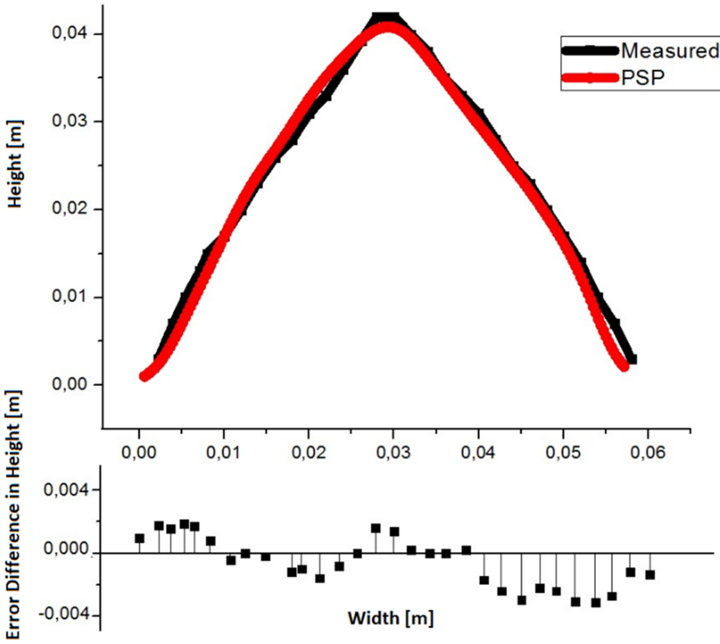

Figure 5.6. Comparison of the constructed and real object cross sections for the triangular prism.

Our second object is a Styrofoam half–sphere. The deformed and reference fringe patterns for the half–sphere are given in Figure 5.7 . Similar preprocessing steps as used in the triangular prism are applied to this object. The maximum height of the half–sphere is approximately 19.05 mm and the diameter is 60.20 mm.

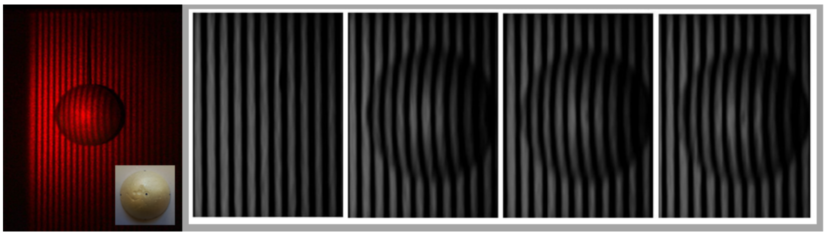

Figure 5.7. Undeformed and deformed consecutive fringe patterns for the half–sphere shape.

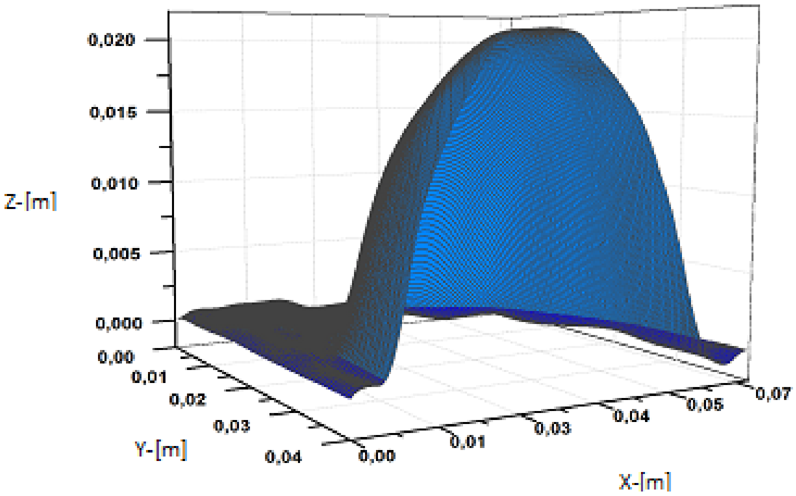

Figure 5.8. Reconstructed half–sphere cross section for Three Step Phase Stepping using Lloyd′s Mirror Assembly.

The reconstructed half–sphere is depicted in Figure 5.8 . To additionally illustrate this, the cross section of the half–sphere is depicted in Figure 5.9. The constructed object height is 19.7 mm and the diameter is 55.7 mm. The maximum rms error for the whole surface is calculated to be approximately 0.4 mm. A comparison of the real and constructed dimensions of the half–sphere is depicted in Figure 5.9. Here the Styrofoam halfsphere is carefully measured by a caliper on several points and a half–sphere is plotted to compare it with the reconstructed image profile.

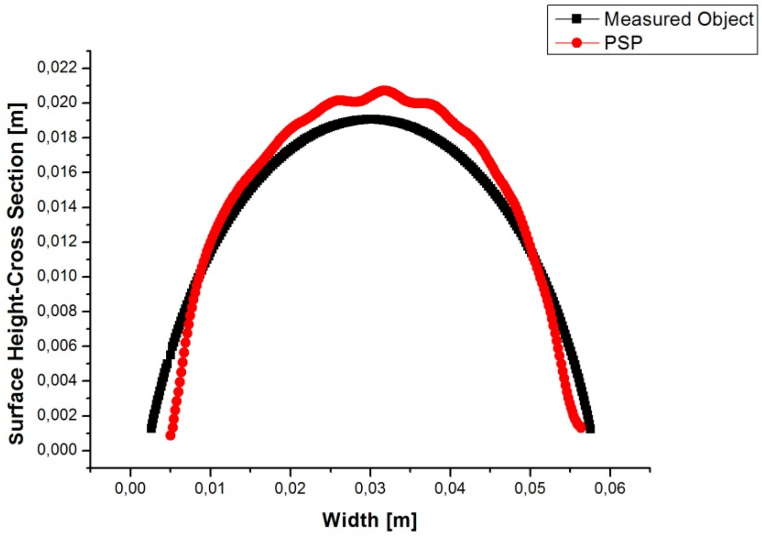

Figure 5.9. Comparison of the reconstructed and the real half–spherical object cross sections. The rms error is calculated for the whole surface as 0.4 mm.

The PSP method is also applied to several irregular–shaped objects. Here, star–shaped and heart–shaped Styrofoam objects reconstructed and plotted in 3D with a constant base. The maximum height of the star–shaped object is around 14.15 mm and the heart–shaped object′s height is approximately 17.40 mm. The shapes of the reconstructed objects redepicted in Figure 5.10. The constructed maximum height for the star–shaped object is 14.17 mm and for the heart–shaped object the maximum height value is 16.72 mm.

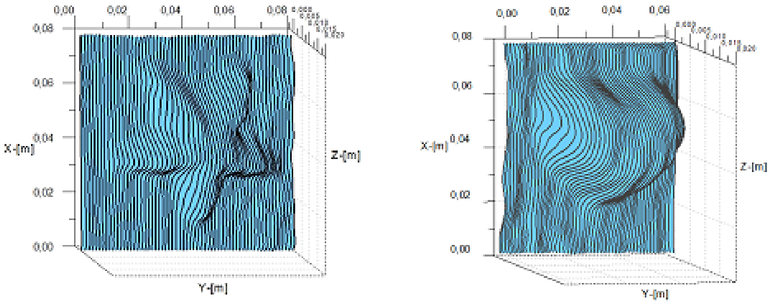

Figure 5.10. Different object surfaces constructed in PSP algorithm using Lloyd′s mirror assembly.

5.5. Calculations

The calculations done in Chapter 4 are repeated for PSP fringe patterns. Here δ is taken as 130μm and using Equation 5.10 the number of fringes in PSP setup is calculated as

$$N \leq \frac{\delta\kappa\sqrt{2}}{\lambda} \tag{5.9}$$

$$N \leq 40.6 \tag{5.10}$$

That is verified by enumerating visible fringes from the highest intensity one to the faded one. The constants, L is 120 cm and δ is 130 μm;

$$P_0 = \frac{\lambda L}{\delta} = 5.84mm \tag{5.11}$$

Fringe spacing is much smaller than previous fringe pattern because the plane screen is much closer to the CCD camera this time. After the captured image of the fringe pattern is converted to gray scale and the difference between the maximum and the minimum of gray levels of the pattern is extracted from the intensity matrix. The difference of gray level is 88 between the peak and the valleys of the fringe pattern. We used the same camera with the FTP procedure but this time the screen is much closer so using this constant and viewing angle θ

$$R = \frac{P_0}{88 \cdot \sin(8°)} = 0.48mm \tag{5.12}$$

5.6. Discussion

This section demonstrates that aforementioned technique can be extended to the phase shifting method for the optical profilometry application. The shifting operation can be handled by a micrometer, which is mounted to a stage that carries the fiber–mirror assembly. The fringe shifting process does not require any PC controlled 3D translation stages, which reduces the cost of the optical setup. Since the single–mode optical fiber is glued to the mirror, the assembly becomes very robust allowing the fiber mirror separation not to be affected while the system is translated back and forth. The undistorted and well–defined fringe pattern indicates the solidity of the experimental setup. The fiber optic Lloyd′s technique introduced in this work proves itself superior to other nondigitized fringe pattern techniques intended to construct, project, and shift the interference fringes. Although multicore fibers and optical fiber couplers are commonly used techniques in generating the structured light patterns, such setups are vulnerable to shrinkage and/or expansion of the fiber material itself due to environmental thermal fluctuations. These external factors introduce significant path length differences between cores in a multimode fiber or between the two arms of a directional coupler, which is enough to distort the fringe pattern and introduce significant errors in measuring the surface topography of an object. In comparison, this new fiber optic Lloyd′s mirror technique is immune to such external factors since the interference pattern is obtained by a single–mode optical fiber with its virtual image at a flat mirror. Additionally, the fiber optic Lloyd′s mirror technique is not affected by the bending of the fiber optic cable, with added ability to overcome problems associated with the characteristics of the optical fiber. These problems include nonidealities in core radius, refractive index profile, or cylindrical geometry throughout the addressing fiber. All these factors are critically important and need to be carefully addressed when employing a fiber optic coupler or a multicore optical fiber to achieve good coupling and equal optical power distribution between the cores for a stable interference pattern. Another advantage of the fiber optic Lloyd′s mirror technique is that the separation between the fiber and mirror may be adjusted to arrange an optical pattern that accommodates the need of the experimenter.

The new setup is flexible and can easily produce slimmer or thicker fringe patterns by adjusting the separation δ in Figure 5.1. In this work, a vertical fringe pattern is used and a PSP algorithm preprocess step is run. This is performed concurrently while various filters are applied to the frames to minimize the error in the measurements.

PSP is a temporal technique, which requires the intensity information of a precise pixel in each consecutive frame to be intact [see Equation 5.4]. If there is an undesired shifting between the frames, the information changes and this results in a significant error in the constructed surface matrix. On that account, the Lloyd′s technique fulfills the requirements of the phase shifting optical surface topography applications very well. Although the fiber optic Lloyd′s mirror method presents a basic and a highly accurate measurement of the surface profile of objects, some limitations must be considered before starting image processing. In the Lloyd′s assembly, the projected fringe separation is robust, but the intensity of the constructed fringes decreases a bit while moving off from the first constructed fringe. At the very far end of the fringe pattern, light and dark fringes cannot be distinguished anymore and that will cause an error during image processing. Fortunately, nonuniform intensity distribution did not affect the phase map during image processing since the contrast of the fringes projected on the whole surface of our sample is quite good. For larger objects, this issue can be resolved using a more powerful laser source, that is to say a much higher–intensity fringe pattern. The other main source of error emanates from the mistakes generated during the image capturing process. The fringes projected on the object are deformed due to the object′s height profile. Due to the nature of the discreetness of the interference pattern, any large shadowed regions on the object′s topography can result in malfunction with the unwrapping algorithm. Therefore, the target objects must be placed on the screen properly, or, alternatively, the fiber mirror assembly must be rotated sufficiently to reduce the shadowing problems accordingly. The ripples on the constructed object profiles may be reduced by employing more powerful filtering applications. In this study, a 2D phase unwrapping algorithm is successfully employed for most of the profiles. It is noted though that the phase unwrapping algorithm is not capable of overcoming all the unwanted problems at the very dark and deep regions. Improved unwrapping algorithms developed in future studies may help to increase the success at these regions. In this part of the work, rms error measurements could be determined for regular geometric shapes, such as a triangle and a hemisphere, as shown in Figure 5.4 and 5.7, respectively. Such rms calculations could not be performed for irregular shapes shown in Figure 5.10 since the topographies are very much complicated and it is almost impossible to get reliable and accurate true surface topography measurements using an ordinary ruler or caliper.

5.7. Conclusion

A phase stepping optical profilometry is achieved for the first time using a fiber optic Lloyd′s mirror assembly. Compared to other fringe projection techniques, this experimental setup is superior to existing techniques due to its low cost, practicality, accuracy, and robustness as it is clarified in Fourier transform application. The constructed light pattern is less sensitive to external factors, such as ambient vibrations and thermal fluctuations, which cause deterioration during sequential image capturing. Our preliminary results prove that the Lloyd′s technique is successfully applicable to phase shifting optical profilometry. A high quality mirror with higher reflectance ratio and flatness may be used to improve the quality of the structured light pattern. The proposed fringe projection technique is both practical and easy to construct and can be a promising method for reconstruction of 3D shape measurements of rigid objects via noninvasive optical profilometry techniques.

6. CONTINUOUS WAVELET TRANSFORM OPTICAL PROFILOMETRY METHOD

6.1. Introduction

The final of our study considers a modification on the experimental setup to be able to scale the fringe pattern in micron–size. The Lloyd's mirror setup is combined with an optical microscope for increasing the resolution and minimizing the projection area. The Continuous Wavelet Transform (CWT) Profilometry method is used for phase extraction and surface topography calculations.

Wavelet transform is a tool that cuts up data or functions or operators into different frequency components, and then studies each component with a resolution matched to its scale [95]. The wavelets provide a tool for time-frequency localization. The continuous wavelet, discrete wavelet, within discrete wavelet, redundant discrete (frames) and orthonormal basis of wavelet are substantial methods. The wavelet transform is a useful tool especially for analyzing non-stationary or transient signals.

The Continuous Wavelet Transform method provides the signal to be well represented in both time-space and frequency domains because of dilation and translation characteristics of the daughter wavelets. Compared to Fourier analysis, Wavelet Transform method is more suited in actual measurements to phase information retrieval from a non–stationary signal [96]. Fourier analysis method is a global signal analysis tool so it can not perform local analysis and is affected by spectrum overlapping problems. A solution of this problem is using a window function to analyze the local signal, however, making this choice automatically is another challenge. Wavelet analysis method brings a solution to this problem and can extract the phase map from only one single frame [97, 98]. Wavelet transform method does not suffer from the spectrum overlapping problems, thus, offers higher accuracy.

M. Farge explains the Wavelet Transform method in [99] and the study gives a detailed definition of the wavelet function and indicates it to be called the “wavelet”. The analyzing function should be admissible, that is, its average should be zero for an integrable function. All analyzing wavelets should have a constant number of oscillations due to similarity properties. The wavelet transform gives very good spatial resolution in the small scales and very good scale resolution in the large scales. Windowed Fourier transform has lack of similarity condition because of its decomposition is based on a family of trigonometric functions exhibiting increasingly many oscillations (trigonometric functions oscillate forever) in a window of constant size (the Hanning Window is explained in FTP Chapter). In that case, the size of the window limits the spatial resolution in the small scales and the range of the large scales.

If we consider a function that is smooth everywhere except a few points with singularity the problem becomes much tougher. The positions of the singularities are related to the phase of all the Fourier coefficients. Therefore there is no way to localize the singularities in Fourier space. f(x) is nonregular with singularities and then the essential information is lost, which means, f(x) is regular everywhere except at a few singular points. Thus if this is an experimental error that needs to be erased from the raw data, filtering is not possible because it has already affected all Fourier coefficients [99]. However, wavelet transform keeps the locality of the signal and allows the local reconstruction of a signal.

One more superiority of the wavelet techniques is the number of available wavelet functions. The most appropriate one can be chosen for the signal in concern. Depending on what signal features are aimed to be detected, the user can feel free to select a wavelet that suits best. This can not be an option for Fourier analysis which is restricted to only one feature morphology (that is the sinusoid). Haar wavelet, Meyer wavelet, Morlet wavelet and Daubechies wavelet are some well-known wavelet functions.

In this study, the phase map of the deformed fringes is extracted by 1D CWT technique using Morlet Wavelet as a mother wavelet. After the phase is extracted, a phase unwrapping algorithm is applied to make the phase continuous. The details about the phase unwrapping and its importance are explained in the section Phase Unwrapping and Phase Extraction.

There are two methods used in carrier phase subtraction: Linear and non-linear carrier removal methods. In the thesis study of Inanc in 2017, it is explained how to apply both methods [100]. Linear carrier removal depends on a plane fitting to the undeformed part of the fringe pattern and then subtraction this calculated plane from the phase map, while non-linear carrier removal is done by capturing the fringe pattern that is projected on a reference surface. Then, the phase of reference frame is subtracted from the deformed fringe pattern phase map and only phase deformation is extracted. In above mentioned study, both methods are explained in detail and in our study, non-linear carrier removal method is applied for a true phase map of deformation. Finally, the phase map is multiplied by a constant that is derived from a calibration procedure to get the real surface height distribution of the object. Our first rigid target is a micro-channel on silicon wafer with an ion–beam cut in the middle. Then our second object is a set of hydroxyapatite discs which are used in biological applications as a substrate for bacterial growth and biofilm formation. We investigate their surface structure and compare various disks using height calibration process. All the calibration methods and error analysis are given in details in the results section.

6.2. Fringe Analysis for Continuous Wavelet Transform

The intensity distribution of the fringe pattern is given as;

$$g(x,y) = A(x,y) + B(x,y)\cos[2\pi f_0 x + \phi(x,y)] \tag{6.1}$$

Here, A(x,y) is the background illumination and B(x,y) is the amplitude of the modulation. The sinusoidal frequency is given as f_0 and the object$'$s phase distribution is $\phi(x,y)$.

The frame is a two-dimensional matrix and the wavelet transform will be carried out line by line along the chosen direction of y for the fringe image $g(x,y)$. We implement continuous wavelet transform method and the integration of the transform is given by

$$W(a,b) = \int_{-\infty}^{+\infty} I(x)\psi^{*}_{a,b}(x)dx \tag{6.2}$$

Since the captured frame will be analysed line by line, $I(x)$ represents a line of the fringe image $g(x,y)$, and $\psi(x)$ is the mother wavelet that will be introduced below. The constants $a(>0)$ and $b(\text{real})$ are scale parameter and shift parameter, respectively.

$$\psi_{a,b}(x) = \frac{1}{\sqrt{a}}\psi(\frac{x-b}{a}) \tag{6.3}$$

$\psi_{a,b}(x)$ function is vertically magnified by a constant $\frac{1}{\sqrt{a}}$ and is expanded with a horizontally. W(a,b) is in fact represents the strenght of correlation between $\psi_{a,b}(x)$ and $I(x)$. $\psi^{*}_{a,b}(x)$, which is the complex conjugate of ψ. The choice of mother wavelet is important for the process, besides the description of the function as a wavelet must ensure those criteria. These criteria are listed in the study of Addison et. all (2005) [101].

(i)The function must have finite energy as

$$E = \int_{-\infty}^{+\infty} |\psi(t)|^2 dt < \infty. \tag{6.4}$$

(ii)If $\hat{\psi}(f)$ is the Fourier transform of $\psi(t)$, i.e,

$$\hat{\psi}(f) = \int_{-\infty}^{+\infty} \psi(t)e^{-i(2\pi f)t}dt \tag{6.5}$$

then the admissibility condition must hold

$$C_g = \int_{0}^{+\infty} \frac{|\psi(t)|^2}{f} df < \infty. \tag{6.6}$$

The wavelet must has no zero-frequency components or, in other words, it must have a zero mean ($\hat{\psi}(0) = 0$). The Equation 6.6 is called as admissibility condition and the constant C_g varies due to the chosen wavelet.

(iii) For complex or analytic wavelets, the Fourier transform must be real and must vanish for negative frequencies.

$$\hat{\psi}(f < 0) = 0 \tag{6.7}$$

All these steps are for an appropriate choice of a suitable mother wavelet. After picking the most applicable one to the current condition, the Equation 6.2 needs to be solved. The solution can be achieved using fast Fourier Transform algorithm by defining Equation 6.2 in Fourier space. Here, the Parseval Theorem offers in Equation 6.8 that the integration of a function multiplied with another complex conjugate function will be equal to the integration of the multiplication of the Fourier transforms of these two functions. This formulation can be named also Plancherel [102].

$$\int_{-\infty}^{+\infty} f(t)g(t)^* dt = \frac{1}{\sqrt{(2\pi)}} \int_{-\infty}^{+\infty} \bar{f}(w)\bar{g}(w)^* dw \tag{6.8}$$

Fourier Transform of both functions in equation 6.2 are given below

$$I(x) = \int_{-\infty}^{+\infty} \hat{I}(s)e^{i2\pi sx} ds, \quad \psi(x) = \int_{-\infty}^{+\infty} \hat{\psi}(f)e^{i2\pi fx} df \tag{6.9}$$

The variable change is done as and the $\psi(x)$ takes the form of;

$$x \to \frac{x-b}{a} \qquad \& \qquad \frac{f}{a} \to g \tag{6.10}$$

$$\begin{aligned}\psi(\frac{x-b}{a}) &= \int_{-\infty}^{+\infty} \hat{\psi}(f)e^{i2\pi f(\frac{x-b}{a})}df \\ &= \int_{-\infty}^{+\infty} \hat{\psi}(f)e^{i2\pi f\frac{x}{a}}e^{-i2\pi f\frac{b}{a}}df \\ &= \int_{-\infty}^{+\infty} \hat{\psi}(ag)e^{i2\pi xg}e^{-i2\pi gb}adg\end{aligned} \tag{6.11}$$

Finally the Equation 6.11 and the Fourier of I(x) is put into the Equation 6.2, which yields

$$W(a,b) = \frac{1}{\sqrt{a}}\int_{-\infty}^{+\infty} dx\int_{-\infty}^{+\infty} \hat{I}(s)e^{i2\pi sx}ds\int_{-\infty}^{+\infty} \hat{\psi}^*(ag)e^{-i2\pi xg}e^{i2\pi gb}adg \tag{6.12}$$

Solving Equation 6.13 for x variable results in a delta function

$$\begin{aligned}W(a,b) &= \sqrt{a}\int_{-\infty}^{+\infty}\int_{-\infty}^{+\infty} \hat{I}(s)\hat{\psi}^*(ag)e^{i2\pi gb}dsdg\delta(s-g) \\ &= \sqrt{a}\int_{-\infty}^{+\infty} \hat{\psi}^*(ag)e^{i2\pi gb}dg\int_{-\infty}^{+\infty} \hat{I}(s)\delta(s-g)ds\end{aligned} \tag{6.13}$$

This equation can be written also in the form of

$$\begin{aligned}W(a,b) &= \sqrt{a}\int_{-\infty}^{+\infty} \hat{\psi}^*(ag)e^{i2\pi gb}dg\hat{I}(g) \\ &= \int_{-\infty}^{+\infty} \hat{I}(g)\hat{\psi}^*(g)_{a,b}dg\end{aligned} \tag{6.14}$$

The complex conjugate function in above equation is $\hat{\psi}_{a,b}(g) = \sqrt{a}\hat{\psi}^*(ag)e^{i2\pi gb}$.

The solution of 1D CWT equation gives the complex array with the coordinates a and b for every row of the intensity matrix. Then, the modulus and the phase of this complex array W(a,b) is extracted for every row of the image. That step is important for the phase extraction of the 2D signal. The calculated modulus and the phase are

$$M_w(a,b) = |W(a,b)| = \sqrt{[Re(W(a,b))]^2 + [Im(W(a,b))]^2} \tag{6.15}$$

$$P_w(a,b) = \arg(W(a,b)) = \arctan(\frac{Im(W(a,b))}{Re(W(a,b))} \quad (6.16)$$

6.2.1. The Morlet Wavelet

The Morlet wavelet is the most popular complex wavelet that is preferred in practice. General form of the Morlet wavelet is given by [101].

$$\psi(x) = \frac{1}{\sqrt[4]{\pi}}(e^{iw_0x} - e^{i\frac{w_0^2}{2}})e^{-\frac{x^2}{2}} \quad (6.17)$$

w_0 is the central frequency of the mother wavelet. In Equation 6.17, the second term is the correction term which corrects the non-zero mean of the complex sinusoid the of first term. If the central frequency is taken greater than 5, then this term can be neglected. We picked up the central frequency term 6 in our calculations.

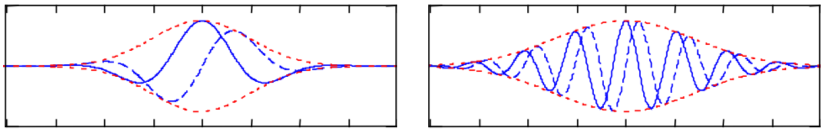

Figure 6.1. The Morlet wavelet functions with $w_0 = 2.0$ and $w_0 = 12$, respectively [101].

As it is indicated in Equation 6.8, both the Morlet wavelet and the Intensity function's Fourier transforms need to be calculated. If we put Equation 6.17 in Equation 6.9 the ψ (x) function is derived. In MATLAB code, the Fourier of the intensity function $I(x)$ in Equation 6.9 is calculated using the *cwt1d.m* function which is a special file belonging to the YAWTB directory (Yet Another Wavelet Toolbox) [103]. Then direct ridge maximum method is used for the phase calculations.

6.2.2. Direct Ridge Maximum Method for Phase Extraction

The modulus array in Equation 6.15 is introduced to be the amplitude of the complex array W(a,b). Gdeisat *et al.* (2009) studied 1D continuous wavelet transform for spatial and temporal carrier fringe pattern demodulation and in their study, Morlet wavelet is used as the mother wavelet for 1D-CWT [104]. Figure 6.2(b) shows the modulus of the array in gray scale. White areas in the image indicates large values while the dark ones indicate small values in the transform. Translation (shift) parameter b and scale factor a are given in horizontal and vertical axis, respectively. The extracted phase array from Equation 6.16 is given in greyscale in Figure 6.2(c).

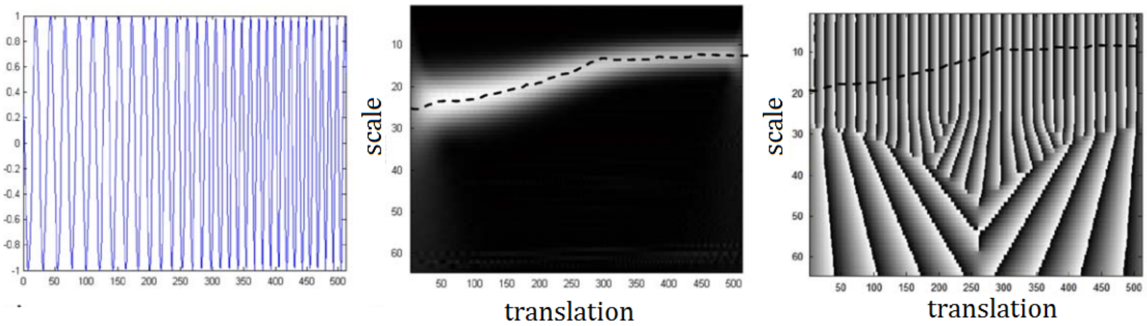

Figure 6.2. Intensity of (a) a fringe pattern, (b) its modulus and (c) phase arrays [104].

Direct ridge maximum detection algorithm is used for calculations of the phase for each row. First, the maximum value of the modulus for each column for all the b values in Figure 6.2b is determined then the corresponding phase at these points are chosen from Figure 6.2c. The dotted lines in (b) and (c) parts show the maximum value of the modulus and the element a_r with the maximum point is called as ridge point. All the maximum points are the ridges of the wavelet. A path is constructed following all the maximum points for every b values and this path is called as ridge array. This procedure makes out the coordinates a and b where the phase of the wavelet and the phase of the signal are similar. The phase of the chosen row of the intensity frame is given

$$P_{wr}(ar(b),b) = arg(W_r(a_r(b),b)) = \arctan(\frac{Im(W_r(a_r(b),b))}{Re(W(a_r(b),b))} \tag{6.18}$$

After calculating the first row, this process is repeated for every row of the intensity matrix of the image. Final phase map is extracted from the whole columns and then a phase unwrapping algorithm is used to unwrap the phase to gain a continuous phase map. This final phase includes $2\pi f_0x+\phi(x,y)$ carrier removal term and the modulation term, respectively. Carrier removal term comes from the nature of the tangent function which is explained in the chapter Phase Unwrapping and Phase Extraction. The carrier removal term needs to be erased for a successful phase matrix.

The flow chart of the CWT method is given in Figure 6.3. The deformed fringe pattern is captured and then the frame is converted to greyscale and every row of the intensity matrix is Fourier transformed. This row matrix is put into 1-D CWT algorithm. The Fourier transform of the row matrix and the Fourier transform of the Morlet wavelet are inserted into the CWT equation and after this step the modulus and the phase arrays are calculated. Determining the maximum of the modulus array gives us the ridge arrays. The corresponding point of these ridge points on the phase array matrix are chosen and this process is repeated for every row of the captured frame. Finally a 2D total phase matrix is built and an unwrapping is applied to form a continuous phase distribution. The carrier removal step ensures that the tilt is removed from the total phase and then only the phase of the deformation is remained. In our final step, the phase map is multiplied with a constant, that is, it is derived from a calibration procedure to get the real surface height distribution of the object.

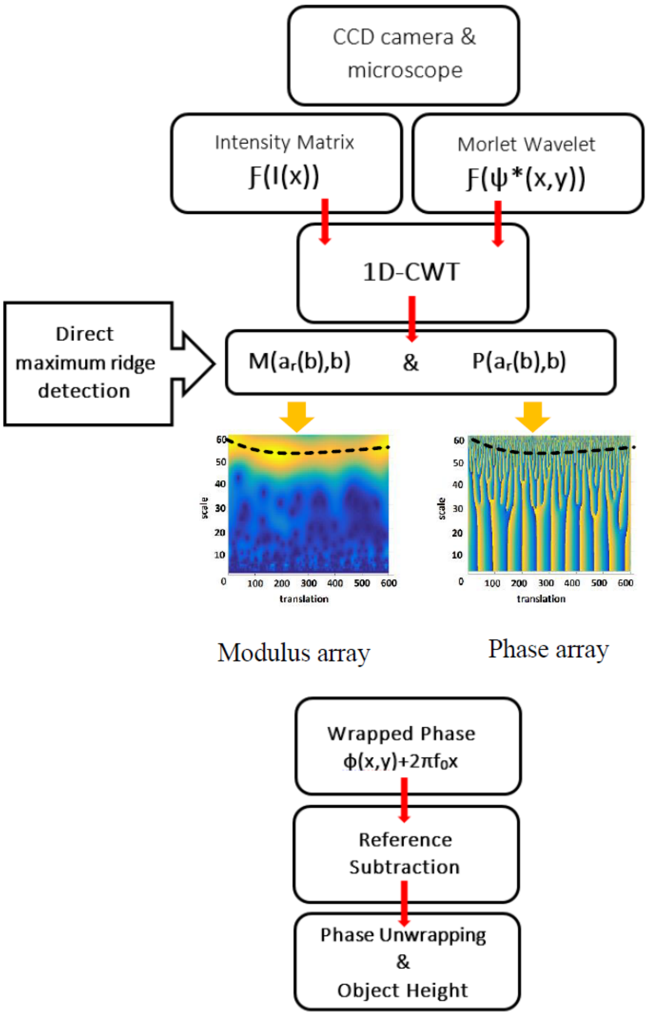

Figure 6.3. Flow chart of the CWT algorithm.

6.3. Experimental Setup for the Continuous Wavelet Transform (CWT)

The experimental setup is redesigned to perform micron-size fringe pattern generation. The Lloyd's mirror is used to generate the fringe pattern but this time the fringe frequency is increased as much as possible for micron-size target area. The setup is not planar to the optical table anymore but vertical and an optical microscope is used to ensure optical path between the camera and the target surface. A He-Ne laser with 632.8 nm wavelength is used and the laser beam is coupled into a single mode optic fiber. The tip of the fiber is placed very close to the mirror surface but not attached to it. The mirror is an Al-coated regular round mirror. The mirror and the fiber optic chuck is placed paralel and positioned above the stage so that the generated fringe pattern can easily illuminate the planar microscope stage. CCD camera is an Optronis CR 600x2 CamRecord High-Speed camera (with monochrome sensor). The detailed sketch of the stage is given in Figure 6.4.

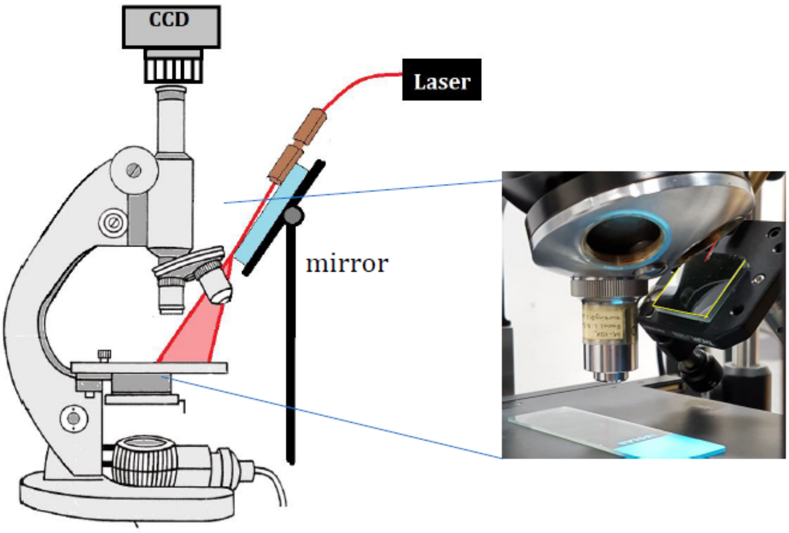

Figure 6.4. Microscope stage and Lloyd′s mirror configuration.

Figure 6.4 illustrates the microscope stage and Lloyd′s mirror configuration. The fringe pattern is projected to a point where the objective of the microscope is focused on. The focal plane of the objective lens on the microscope is chosen 5 cm with 10x magnification and the CCD camera is focused on the vertical eyepiece tube on the top of the microscope. The frames are captured in an optical laboratory under indoor lighting. After the setup construction, the target surfaces and the objects are placed on a microscope slide and positioned under the objective. The position of the microscope stage is adjusted to focus on the fringe patterns and after the highest resolution fringes are observed on the computer screen (that the CCD camera is connected), the frames are captured.

The difference of this study from previous chapters is that it considers micro-scale fringe pattern generation and the fringe frequency is varied and the total area of the projected fringes is minimized as much as possible. The total visible area that the objective is focused on is a circle with a radius of approximately 750 μm. So the total calculated area under the objective that the fringe pattern is visible is approximately 1.77 mm^2. All frames have a 1280 ×1024 pixel resolution.

The main aim is to find the surface topography so the calculated phase map must be converted into a real object dimension matrix for a true description of the target surface. To do so, in general triangulation method is used. This basic technique ensures a true description of the object surface with multiplying the phase matrix with a constant that is derived using setup parameters.

6.3.1. Optical Triangulation

Figure 6.5 indicates the optical triangulation method. The technique is basic and depends on the triangulation of the optical setup and triangle resemblance method. M is the point that the laser beam is projected on the microscope stage and if there is not any target object, the beam coming from the M point would directly reach to the point A'. When a target is placed on the plane surface, this point will shift to the point P and its projection on a plane surface is indicated as A. This is the fringe shift due to the height of the object. $|A'A|$ shift is equal to the distance $|CC'|$. $h(x, y)$ is the surface height at that coordinates and L is the distance between the screen and the CCD camera. θ is the angle between the camera axis and laser beam.

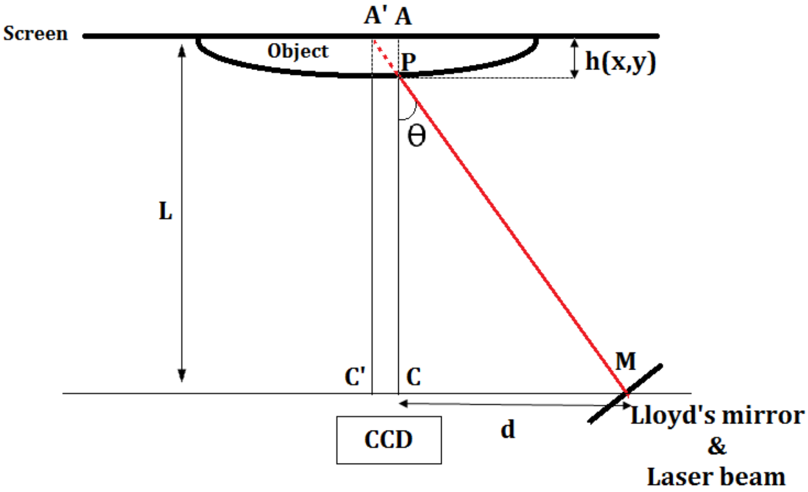

Figure 6.5. Optical Triangulation.

Now considering the small and the big triangles, we can write below formulation through the triangle resemblance of $\triangle(A'AP)$ and $\triangle(MCP)$ as

$$\frac{|A'A|}{|AP|} = \frac{|CM|}{|CP|} \tag{6.19}$$

h(x,y) is $|AP|$, $|CM|$ is d, $|CP|$ is $L - h(x, y)$. Using all these definitions and above formulations we can write basicly,

$$\frac{|A'A|}{|h(x,y)|} = \frac{|d|}{|L - h(x,y)|} \tag{6.20}$$

The height formula can be derived from equation 6.20 as

$$|h(x,y)| = \frac{|A'A||L|}{|A'A| + |d|} \tag{6.21}$$

Here the fringe shift is related to the difference of $|A'A|$. So this parameter can be connected to the amount of phase shifting. Considering fringe pattern, for a length of fringe frequency λ the total phase is 2π.

If we establish a proportion, for a 2π total phase difference, a wavelength of λ is required, so for a $\phi(x)$ phase distribution, a $\triangle x$ spatial distance is required. This spatial distance in our case is $|A'A|$ so $\triangle x = \frac{\phi(x)\lambda}{2\pi}$. Finally the height description of the object is given in below by formula ;

$$|h(x,y)| = \frac{\phi(x,y)L}{2\pi f_0 d} \tag{6.22}$$

We assume that the $d \gg \triangle(x)$ and the wavelength of the fringe pattern is related with the fringe frequency $\lambda = \frac{1}{f}$.

The Equation 6.22 gives the height description of the object. Normally, the variables (L, d) that depend on the experimental setup can be measured and in previous sections they are measured and added in calculations. Now we use an optical microscope system and measuring these parameters in a high precision, which is quite challenging. That is because the camera and the mirror assembly are not placed on the same level as it is indicated in Figure 6.5. The anticipated positioning of the camera and the mirror assembly as in the figure does not let the fringe pattern projected on the focal area of the microscope. Also, the width of the fringes must be very small to ensure that enough number of fringes are projected on the target object.

So an alternative method of the calculation of the setup parameters is investigated here. In fact the used technique does not calculate one by one all the spatial parameters and the constants but it produces a multiplication constant to convert the phase to the real dimensions of the object.

6.3.2. Step Calibration Instead of Optical Triangulation

The used method is step height fitting and basically, the technique includes capturing multiple successive frames where the microscope stage is moved up and down under the objective and so the fringe pattern is shifted on different points at every step. The position of the microscope stage is moved up and down by using coarse and fine adjustment knobs of the microscope. The fine adjustment knob has a 1 μm resolution, which allows to fix our increments by any amount we want.

Before the experiment starts, the microscope stage position is adjusted that it is inside the focal plane of the objective. Therefore, the observed fringe pattern projected on the plane stage is in focus and well-resolved. More than 15 consecutive frames can be captured moving the microscope stage up or down. Inside all these frames, 5 or more successive frames are chosen and then a portion of these images are cropped and copied on one single image. The fringe shift, in other words, the phase shift can be observed directly on this image. The real phase difference between the steps is calculated using a MATLAB code which applies the Heaviside step function to the unified image.

Figure 6.6 represents the fringe pattern which is projected on a microscope lame with blue label field. We used this field because it is smooth, nonreflective and also this label field area is free from sparkles when the light is projected on. In fact, the fringe pattern frames belong to microscope lames are used only to explain the step height calibration procedure, efficiently. The following paragraphs explain how Heaviside step function is applied and the calculations which are required to derive the real object dimensions from the phase map of the object. Then, for all samples this procedure is repeated and individual calibrations are done for each different object.

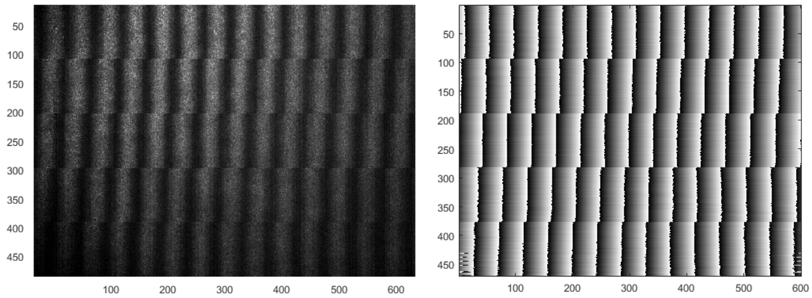

Figure 6.6. Real image and its wrapped phase map of the fringe patterns projected on the microscope lam for 20 μm height steps.

The fringe shift due to the microscope stage positioning is obvious in Figure 6.6. Here, five successive fringe images are chosen and there is 20 μm step heights between each frame. More step height difference results in much more fringe shift. The phase maps of the successive frames is given in Figure 6.6 and 1D–CWT (continuous wavelet transform) algorithm is used to extract the phase distribution of the image. The user can pick different step height values but must keep in mind that if the phase difference between the fringes is equal or greater than the 2π, then the algorithm may have problems about the phase calculation. Because for more than a 2π phase difference the fringe moves on a full period but this total period step variation will not be observed on the fringe pattern because the fringes will be similar to their initial state. One another crucial factor about the phase calculations is the problems about phase ambiguities. The problem depends on the amount of shifting and if this shifting result a phase difference around π, then the algorithm may not recognize if we raise the microscope stage up or lower it. Because the fringes will be shifted by a step that corresponds to π and the camera captures all frames one by one at each position of the stage, the camera can not recognize if the phase is increased or decreased. Thus, sometimes the steps will not be incremented (as it is given in Figure 6.7) but fall to the bottom. Using a much smaller phase increment may solve this problem. A more detailed explanation and relevant figures are given in the thesis study of Inanc, 2017 [100].

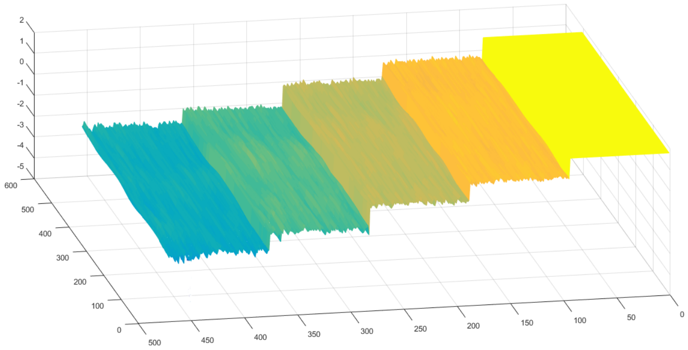

Figure 6.7. 3D constructed phase map of the microscope lam with 20 μm height steps.

All successive frames are taken on the same microscope lame and the unified picture of the cropped fringe patterns are given in Figure 6.6. Now below figure represents the 3D phase map of the unified fringe patterns. The figure clearly shows the phase steps between shifted fringe patterns and these steps are very similar to each other. We used a Heaviside functions to fit these steps. The general definition of Heaviside function that we implement in our calculations is given as

$$\begin{aligned} h(x,y) = {} & a_1 heaviside(y-n) + b_1 heaviside(y-2n) + c_1 heaviside(y-3n) + \\ & d_1 heaviside(y-4n) + f_1 x + g_1 \end{aligned} \tag{6.23}$$

Each consecutive steps has a length which is indicated as a_1, b_1, c_1 and d_1. All the cut frames are unified along y direction so the step height will change along y-axis. Then n variable presents the increment of the step function on y-direction. The amount of n is equal to the length of the y-axis in the cut area of the frame. f_1 is any existing tilt on the image and finally g_1 is a constant that determines the intersection of the yz plane.

To apply fitting on the step heights MATLAB Curve Fitting Tool (cftool) is used. Figure 6.8 presents 3D phase map of the fringe patterns with 20 μm height steps.

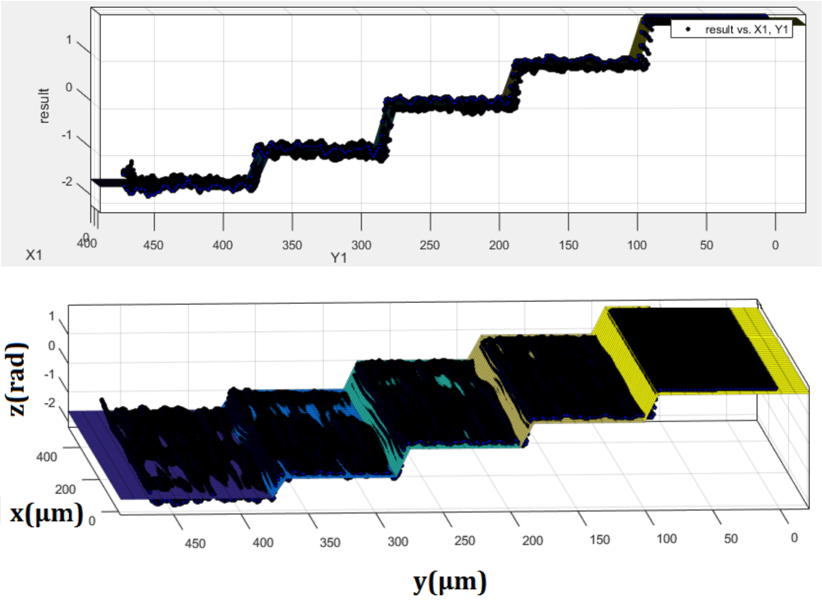

Figure 6.8. 3D phase map of the captured fringe patterns with a 20 μm step height difference between consecutive patterns

The result parameters are given with their corresponding deviations.

$$\begin{aligned}
a_1 &= 0.9385 \pm 0.0013 \quad rad \\
b_1 &= 0.8317 \pm 0.0013 \quad rad \\
c_1 &= 0.9942 \pm 0.0013 \quad rad \\
d_1 &= 0.7049 \pm 0.0013 \quad rad \\
f_1 &= (2.378 \pm 0.284)10^{-5} \\
g_1 &= 1.787 \pm 0.001 \quad rad
\end{aligned} \tag{6.24}$$

The average of the four steps give us the mean phase. The mean phase with the relative error amount is given by

$$\triangle\phi = 0.867 \pm 0.006 \quad rad \tag{6.25}$$

Thus, we can say that for a 20 μm height change will result in a phase of 0.867 rad. Using a basic ratio, user can find a constant c parameter for conversion from the phase

[rad] to the size[meter]. The height matrix can be written basicly as

$$h(x,y) = \frac{\delta(x)}{\phi(x,y)'}\phi(x,y) = c.\phi(x,y) \tag{6.26}$$

where the $\phi(x,y)'$ is the phase which is gained from the calibration process, $\delta(x)$ is the step height value and $\phi(x,y)$ is the phase matrix of the demodulated fringe pattern. For this example, the c constant c is 23.06 [μm/rad]. This conversion is done for every set of the measurement data. Therefore, each time before image capturing of objects is started, the reference fringe patterns are captured and the plane calibration is done.

6.4. Results

6.4.1. Measurement of Microchannel on silicon wafer

A microchannel structure is formed on polished silicon wafer surface with 122 μm depth by ion beam etching. In the middle of the channel there is a small circular area is curved with a diameter of 1500 μm. The diameter is measured under light microscope Leica CTR 6000. Before placing the silicon wafer under the objective, a thin layer of correction fluid is coated on the surface of the wafer and also inside the channel. That is a required step because the surface of the silicon is very reflective and the projected fringe pattern could not be observed on it. After a thin layer of white color coating, the surface is highly visible and the red fringes are easily distinguished on the silicon surface. The major drawback of this step is that the correction fluid has also a thickness. This thickness is studied in A. Inanc's master thesis study [100] and the thickness of the fluid is measured to be 15 μm . This extra thickness is all around the microchannel and also inside the tunnel. The measurement results show that the thickness of the correction fluid increases the thickness at the same amount on every point on the surface of the microchannel so the depth of the tunnel can correctly be measured. After the correction fluid is dried, the microchannel is placed under microscope objective and the fringe pattern is projected onto the surface of the silicon wafer. Figure 6.9 shows the object and the reference fringe frames. We used a reference image to remove the carrier frequency tilt on the phase. First a calibration process is done to extract the constant that is used to convert the phase map to the real dimension matrix, then the reference image and the object images are captured.

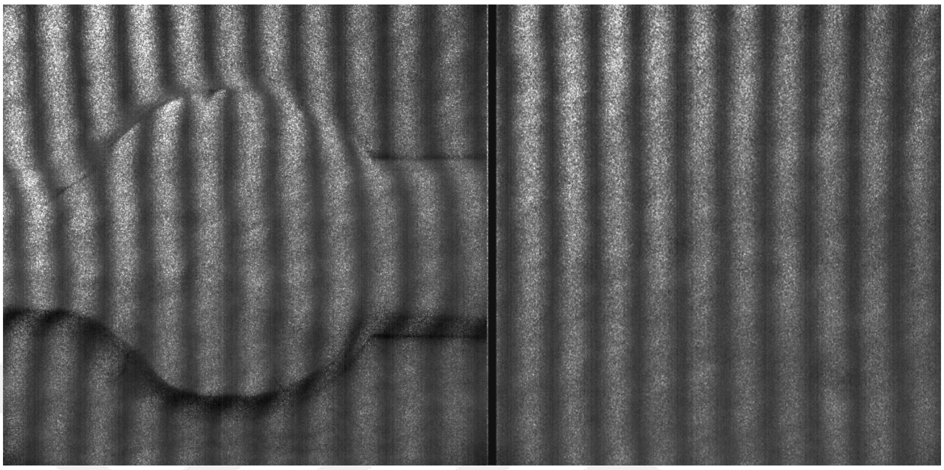

Figure 6.9. Captured fringe patterns projected on the microchannel and the plane surface(image size 1880 $\mu m\times$ 1880 μm).

The dark areas around the circle indicate the areas where the laser light could not illuminate enough. The circular hollow and the tunnel of the microchannel can easily be observed. These are the real images but for image processing, a preprocessing step is applied on each frame and a denoising filter is used to get rid of the sparkles of the frames and to smooth the dark areas. fwt2d˙denoise.m filter can be found in YAWTB directory (Yet Another Wavelet Toolbox) [103]. 1D-CWT algorithm is applied to the images and the wrapped phase maps of the deformed and the reference fringe patterns are given in Figure 6.10.

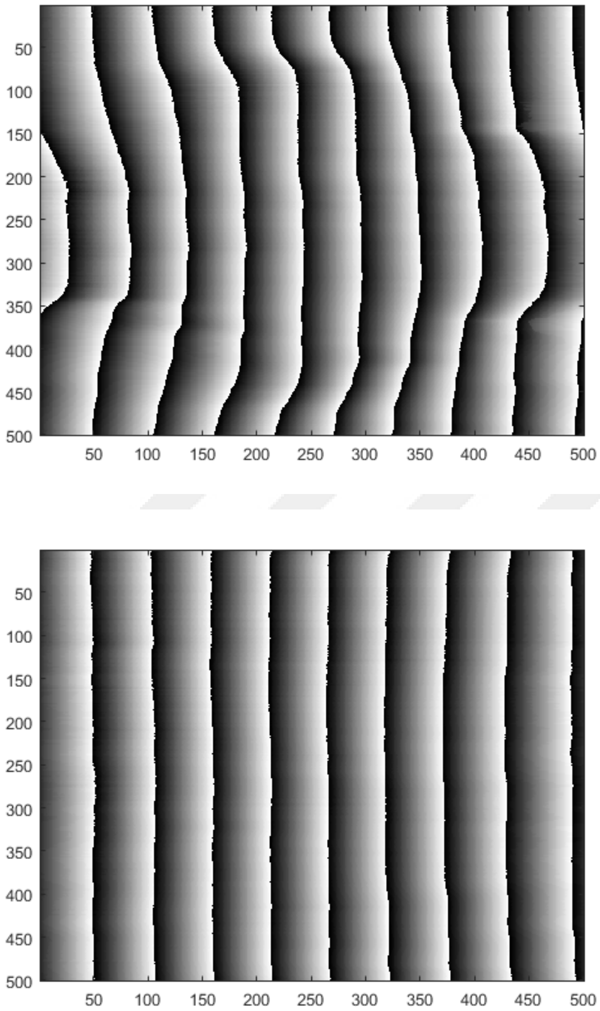

Figure 6.10. Wrapped phases of the deformed and reference fringe patterns for microchannel on silicon wafer (pixel in size)

The wrapped phases are unwrapped by cunwrap.m in YAWTB directory [105] and then the unwrapped phase matrix is converted into real dimensions by multiplying with a constant. This constant value is gained using Heaviside step function that is explained in previous sections. The step height values are given in;

$$\begin{aligned} a_1 &= 1.063 \pm 0.0040 \quad rad \\ b_1 &= 1.31 \pm 0.0040 \quad rad \\ c_1 &= 1.304 \pm 0.0040 \quad rad \\ d_1 &= 1.229 \pm 0.0040 \quad rad \\ f_1 &= 4.641 \pm 10^{-4} \\ g_1 &= 2.21 \pm 0.0040 \quad rad \end{aligned} \tag{6.27}$$

Then the mean phase value ϕ_m is given with its standart deviation error;

$$\triangle\phi = 1.226 \pm 0.115 \quad rad \tag{6.28}$$

The calculation results of the Heaviside step function gives the multiplication constant

$$c = \frac{40 \quad \mu m}{1.2265 \quad rad} \approx 33\mu m/rad \tag{6.29}$$

This ratio defines the multiplication constant c. The error on the calculated multiplication constant depends on the error of the adjustment of stage positioning and the phase calculation.

First error component depends on the adjustment knob of the microscope stage and its precision is about 1 μm. Second component is the error of the phase calculation. If we consider a measurement $A = B.C$, the error on A can be computed through standart error propagation from the individual uncertainities of the measurements of B & C, assuming that those uncertainities are small relative to their central values which are well-behaved (like Gaussian distributed).

$$\sigma_A = \sqrt{(\frac{\partial A}{\partial B}.\sigma_B)^2 + (\frac{\partial A}{\partial C}.\sigma_C)^2} \tag{6.30}$$

The equation 6.31 is written for microchannel multiplication constant and it is given by

$$\begin{aligned}\sigma_c &= \sqrt{(\frac{1 \quad \mu m}{1.226 \quad rad})^2 + (\frac{40 \quad \mu m}{1.226 \quad rad} \times \frac{0.115 \quad rad}{1.226 \quad rad})^2} \\ &\approx 3\mu m/rad.\end{aligned} \tag{6.31}$$

σ_c is the error of the multiplication constant c. Then, we calculate the height description of the object and there will be an error propagation depends on the calculation of c and the phase matrix. Now, using the height formula given in Equation 6.26, the z-profile of the object is calculated with the tolerance of

$$h(x,y) = c \times \phi(x,y) = (33\mu m/rad) \times \phi(x,y) \tag{6.32}$$

The error propagation on every single point of the phase matrix is calculated for height measurement as

$$\sigma_{h(x,y)} = \sqrt{(0.1092 rad \times 33\mu m/rad)^2 + (\phi(x,y) \times 3\mu m/rad)^2} \tag{6.33}$$

Here 0.1092 rad is the $\phi(x,y)$ rmse (root-mean-square-error) value (in rad) for every single point of a phase matrix belong to the area that is cropped at the bottom of the microchannel. That area is used for plane fitting Then, putting the phase matrix into $\phi(x,y)$ in Equation 6.33 gives us the required profile of the target object. Figure 6.11 presents the calibration steps of microchannel where 40 μm height steps are used.

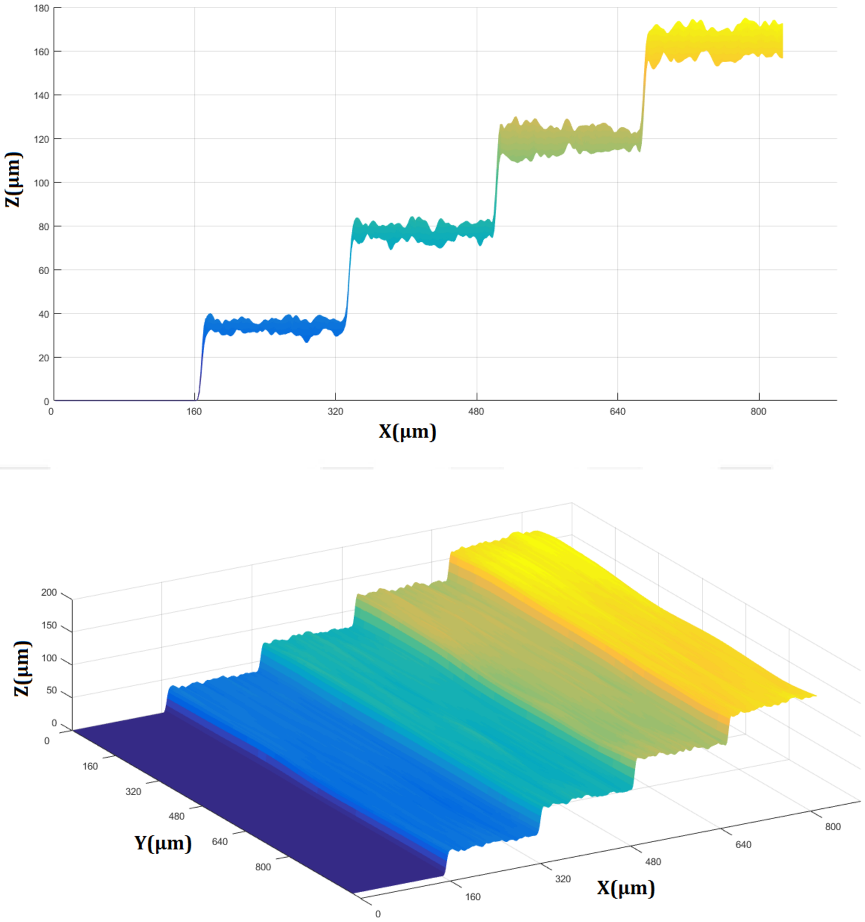

Figure 6.11. Microchannel steps with 40 μm heights for calibration process.

The phase matrix in Figure 6.10 is unwrapped and then multiplied with the coefficient c, and finally, the microchannel height distribution is given in Figure 6.12.

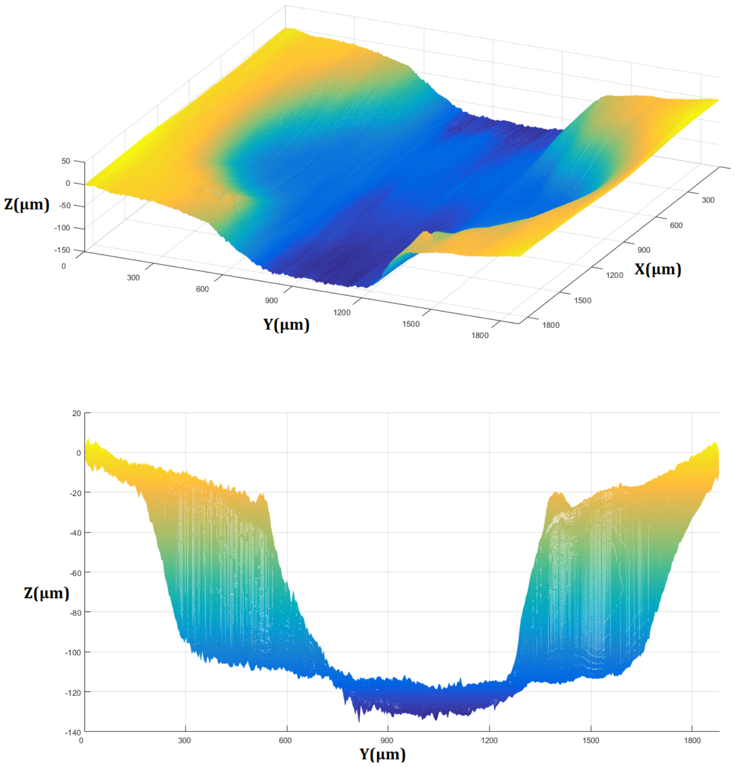

Figure 6.12. 3D surface topography of the microchannel etched on silicon wafer.

The depth of the microchannel is measured for a chosen line on x-axis at 860 μm in the middle of the channel. Figure 6.13 gives the height profile of the channel and the base of the channel is close to 120μm. After plane fitting to the base of the channel, the approximate depth value is given as 119.5μm ±11.6 μm. Here, these fluctuations are very predictable because of the correction fluid on the microchannel. Also, the height variation from the base to the surface is not very sharp because of the fluid accumulation at the edges of the channel. The real depth of the microchannel due to stylus profiler measurement is 122 μm. The depth profile of the microchannel is measured close to the real profile but the correction fluid contribution to the height profile is non-negligible. The fluctuation coming from the correction fluid is not so distinct on the height calibration steps, because the height calibration procedure only considers relative phase changes. And, even though there is an additional coating on the surface, the objective will focus on the same area on the sample so it will not be influenced by the local variations of the sample surface.

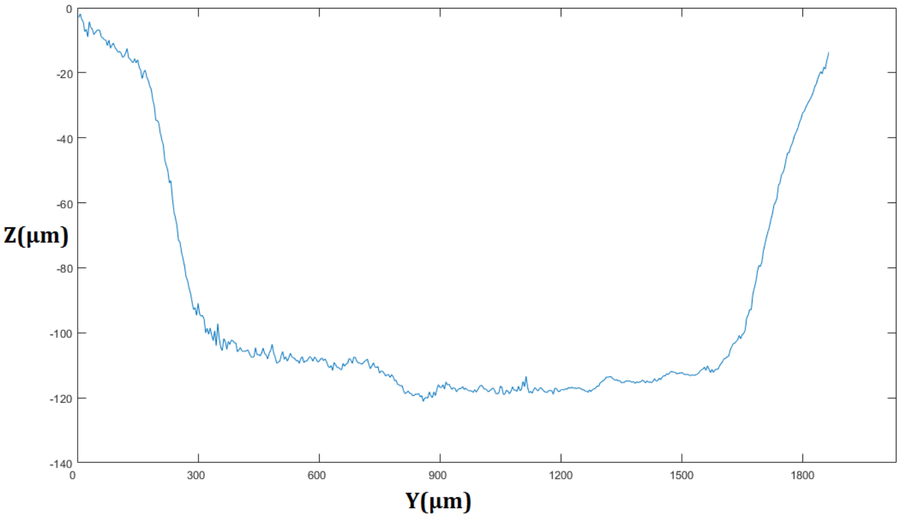

Figure 6.13. Cross-section of the depth of microchannel at X=860 μm.

The vertical calibration procedure is explained for the z-profile in above sections. The step height calibration with consecutive frames gives a reliable and straight-forward conversion from the phase map to the surface profile. For a well defined 3D profile the horizontal axis must also be calibrated and converted into the same scale. For this aim, an image of the microchannel is captured with optical microscope Leica CTR 6000, and then, a pixel to size calibration is done and the ratio derived after this calibration is used as a multiplier for the horizontal profile of the captured images. The captured image of the microchannel is given in Figure 6.14.

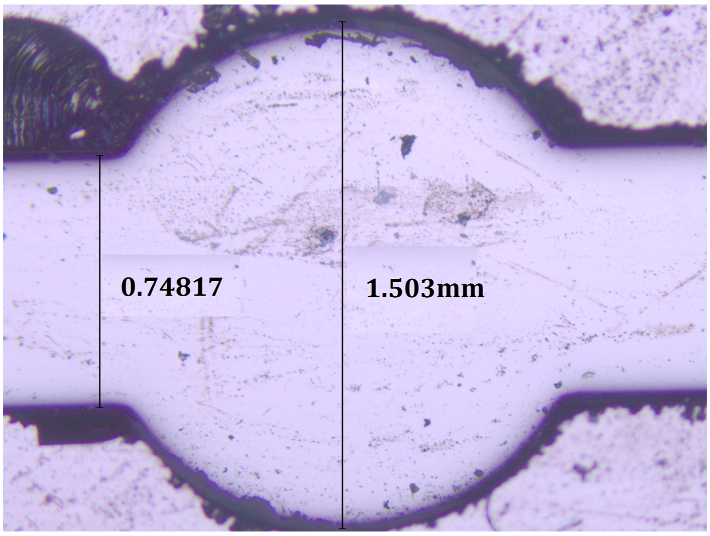

Figure 6.14. Optical microscope image of the microchannel.

6.4.2. Measurement of hydroxyapatite discs

A set of hydroxyapatite discs are delivered from the biology department and the aim of the study is to measure the height differences of all the discs due to a reference one. This procedure is done because all these discs are used in many times for various biological applications. During these previous treatments, the surface of the discs are exposed to many chemicals and rough applications. Biofilm formation and some kind of bacterial growth processes are achieved on the disc surfaces and we want to realize the deformation on these surfaces. If there is a very large amount aberration, it will also affect the thickness of the discs. We would like to find out most damaged discs and pick them out. The surface topograpy is also investigated and the surface is checked if there are cracks or streaks. Lateral calibration is not done because there is not any figure or form on the plane surface.

To this end, the clean and dry hydroxyapatite discs are numbered and placed under the objective of the microscope. The image resolution is the same with the microchannel measurement process but this time apart from the previous study, we do not need any correction fluid because the color of the discs is white. The 4X objective is combined with a NFK 3.3 LD lens and the resolution of the captured frames are the same. The frequency of the fringe pattern is adjusted again and one disc is chosen as a reference one to compare with all others.

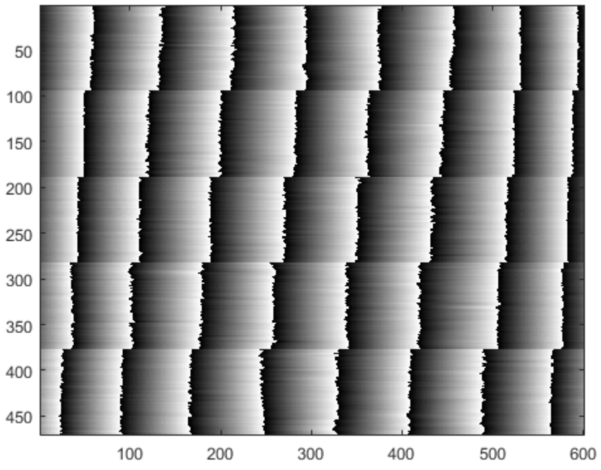

Figure 6.15. Calibration phase map of hydroxyapatite discs with 50 μm height steps.

Table 6.1. The phase difference of all hydroxyapatite discs compared to a reference one and their corresponding height values

#	Phase Difference(rad)	Relative Height(μm)
1	0.688	43.4
2	0.663	41.7
3	0.353	22.2
4	0.610	38.4
5	0.750	47.2
6	0.789	49.6
7	0.713	44.8

Figure 6.15 presents the phase matrix of reference hydroxyapatite disc with 50 μm height step. Heaviside step function is applied to the steps and 0.799 rad phase difference is calculated for a 50 μm height step. Approximately 0.16 rad phase difference occurs for every 10 μm height increase. That value is checked for different step heights and similar results are obtained for 10 μm increments. The relative height differences of each disc with a chosen reference one show that some discs are abraded so much that their thickness is reduced distinctly. These values indicate how much each disc is higher than the reference one, so lower values indicate much higher attrition on the disc surfaces. This comparison procedure is in fact a calibration for the next step of the experiment.

6.5. Discussion

Continuous Wavelet Transform optical profilometry based on Lloyd′s fringe projection method results in an efficient micro-scale optical profilometer. The image capturing procedure is easy to repeat because the fringe frequency is not changed during the procedure, say, even over weeks. The algorithm used for height description of the sample does not depend on the fringe frequency so it would not be a problem even if the fringe pattern changes slightly. On the other hand, that would be a problem when the number of fringes projected on the sample surface change or if the fringe width change. Because very large fringes would cause a rough description of the surface without fine details that the sample has. An easily adjustable fringe pattern helps us very much, especially for fine details or sharp edges of the samples and the user can easily change the fringe width as it is projected on the sample or on the reference surface. After required fringes are gained, the fiber is fixed and the mirror- fiber couples are not disturbed during the image capturing process. In some phase shifting processes, the sample is hung on the screen and the fringe pattern is moved on the object surface. That is the way we did in Phase Stepping Profilometry application. That would not disturb the fringe pattern of the Lloyd′s mirror but needs a delicate treatment to prevent user-based crushes or hits. Unlike, in this setup, after the fringes are adjusted, user hardly touches to the mirror-fiber stage, only moves the microscope stage up or down to form the fringe shift in this assembly.

One important pre-process about the method is the denoising of the captured frames. That is a required process for reducing the sparkles and noise on our images. After denoising, the images become much softer and the errors on the final phase map are reduced so much. The phase of the images can also be calculated using phase˙unwrap.m function [106] but we used cunwrap.m [105] because it does not locate wrapped phase map on the zero-line while plotting. Even though the denoising filter achieves prominent results on the phase map, it should not be ignored that the high-quality images result minor errors. While capturing images, the object and the projection direction of the fringe pattern must be chosen in such a way that there are no shadowing areas or very bright points as much as possible. If this is inevitable, then an enough pre-processing filtering is applied to the captured frames.

The error on the results of the microchannel is relative to the correction fluid and this is a source of error that needs to be removed. The relative error on the result is very approximate to 15 μm which is the height measurement of the correction fluid. The correction fluid fills the edges of the tunnel and it results in a curved shape at the edges of the tunnel instead of a sharp corner shape in Figure 6.13. A different liquid could be used to form a much thinner and homogeneous film on the sample surfaces.

The thickness variations between hydroxyapatite discs are obtained in a very straightforward method. Measurements of degradation, abrasion and diminution on the substrate are major obstacles for successful measurement of the top coatings. If the objective coating is sensitive and vulnerable to rough analyzing methods, then our method becomes much precious as a non-invasive surface topography analysis and profilometry applications.

6.6. Conclusion

The Continuous Wavelet Transform profilometry with fiber optics Lloyd's mirror assembly method has been introduced in this chapter. The experimental setup is easy to configure without the need of any high cost optical apparatus or any kind of optical aligners. The technique is straightforward and the algorithm based on CWT works quite fast. The setup is arranged to measure micro-scale deformations and the profile of the object is measured with an error propagation of $\pm 10\mu$m. This error can be reduced if more height steps are taken into account. However, result graphs indicate that the observed fluctuations on the measured profile are higher than this level of uncertainty because of the correction fluid on the microchannel. This fluid is aimed to be replaced with a smoother and more efficient one in reducing the surface reflection of objects.

7. CONCLUSION

A fiber optical Lloyd′s fringe projection technique has been introduced in optical 3D profilometry, which is applied to three general and leading algorithms. In Chapter 4, it has been demonstrated that our developed fiber optic Lloyd′s mirror assembly enables us to obtain good quality result, which are based on the interference fringes at a relatively low cost and allows to obtain precise 3D topographic measurements combining with the Fourier Transform Profilometry (FTP). These patterns are less sensitive to external disturbing factors such as ambient temperature and vibrations. Using single and double-mirror assemblies introduce a small error in 3D reconstruction of the objects and imply that the proposed technique for the FTP is promising. Pattern improvement may be possible using high-quality mirrors with good reflectivity and better flatness. Since the proposed fringe projection technique is flexible and easy to configure, it enables us to develop unique setups for other specific applications and 3D shapes of more complicated objects.

In Chapter 5, a phase stepping optical profilometry is achieved for the first time using a fiber optic Lloyd′s mirror assembly. The experimental setup has advantages over other existing techniques due to its low cost, practicality, accuracy, and robustness. The constructed light pattern is less sensitive to external factors, such as ambient vibrations and thermal fluctuations, which cause deterioration during sequential image capturing. All results indicate that the fiber optic Lloyd′s mirror assembly can be used as a fringe projection method not only for stationary methods, but is also successfully applicable to shifting related profilometry applications. The proposed fringe projection technique is both practical and easy to construct and can be a promising method for reconstruction of the 3D shape measurements of rigid objects via non-invasive optical profilometry techniques.

In Chapter 6, the Continuous Wavelet Transform profilometry with fiber optics Lloyd′s mirror assembly method is introduced and is combined with CWT method.

Apart from the aforementioned methods in above paragraphs, this setup is arranged to measure micro-scale deformations and the profile of the object in concern is measured with an error of ±11.6 μm. This value can be derived from the Equation 6.33. Plane fitting is applied to the bottom of the microchannel and the depth of the channel is measured approximatelly 119.5 μm. The total error propagation will be a little much while considering phase difference and the contribution of the error in phase to the total phase propagation can be reduced by adding more number of steps to the step height calibration procedure. The total observable area under the objectives is around $1.77mm^2$. The fringe projection technique combined with the optical microscope is a promising method for micron-sized optical profilometry applications. Increasing the fringe frequency means increasing the density of the fringes, which allows to study much finer details on the target objects. All applications, which are mentioned in this thesis have some drawbacks that can be reduced in future studies. The most important and common drawback for each method is the shadowed areas and bright points on the captured frames. To increase the image quality, the position of the target object and the projection angle of the fringe pattern needs to be arranged so that the shadow areas on the captured image are minimum. If it is inevitable to do this, then the user must choose a successful phase unwrapping algorithm that can overcome the broken fringes on the shady areas.

In all sections, the algorithms first extract the phase matrix and then this information is converted into the height description of the target object using a conversion constant. Equation 4.13 in FTP and Equation 5.8 in PSP algorithms carry the experimental setup related constants, which are used for phase to height conversion, while in CWT a calibration procedure is introduced to find the relative conversion constant "c" and to result in a true object profile in meter scale. In all chapters 3D real and the constructed object profiles and the cross-sections of them are given with corresponding errors. The error range in FTP and PSP methods are in millimeter scale while in CWT method the relative error is in micrometer range. All the error values are within the acceptable limits.

Changing the wavelength or combining different laser sources in the fiber optics Lloyd′s mirror assembly may provide an improved and high resolution fringe pattern. As a future work, as it is introduced in CWT section, we have proposed to study the biofilm formation of the bacterial culture on the hydroxyapatite discs and the precise measurements of the biofilms in different proliferation times. The fiber optics Lloyd′s mirror assembly method prove itself for optical profilometry applications from millimeter size objects to a few micrometer scale. To investigate the borders of this introduced fringe pattern on optical profilometry applications is another future aim for our study. Previous studies have shown that there are various nano-lithography and nano-patterning applications, which are based on Lloyd′s mirror method for fringe projection [107–111].

REFERENCES

1. Matthias, S., C. Ohrt, A. Pösch, M. Kästner and E. Reithmeier, "Single image geometry inspection using inverse endoscopic fringe projection", *ACTA IMEKO*, Vol. 4, No. 2, pp. 4–9, 2015.

2. Matthias, S., M. Kästner and E. Reithmeier, "Comparison of LASER and LED illumination for fiber optic fringe projection", *Proceedings of SPIE-The International Society for Optical Engineering 9899 (2016)*, Vol. 9899, p. 989905, 2016.

3. Matthias, S., M. Kästner and E. Reithmeier, "Modeling of imaging fiber bundles and adapted signal processing for fringe projection", *Advanced Optical Technologies*, Vol. 5, No. 5-6, pp. 439–449, 2016.

4. Lilley, F., M. J. Lalor and D. R. Burton, "Robust fringe analysis system for human body shape measurement", *Optical Engineering*, Vol. 39, No. 1, pp. 187–195, 2000.

5. Chen, L., V. Bavigadda, T. Kofidis and R. D. Howe, "Fiber optic projection-imaging system for shape measurement in confined space", *The Scientific World Journal*, Vol. 2014, 2014.

6. Larimer, C., J. D. Suter, G. Bonheyo and R. S. Addleman, "In situ non-destructive measurement of biofilm thickness and topology in an interferometric optical microscope", *Journal of biophotonics*, Vol. 9, No. 6, pp. 656–666, 2016.

7. Tay, C., C. Quan, S. Wang, H. Shang and K. Chan, "Measurement of a microphone membrane deflection profile using an optical fibre and wedge fringe projection", *Measurement Science and Technology*, Vol. 12, No. 3, p. 320, 2001.

8. Huang, X.-f., S.-j. Li, G.-h. Zheng, G.-j. Zhao, J.-r. Xu and W.-c. Wang, "Design and Characteristics of Dual-Core Photonic Crystal Fiber Doppler Differential Velocimeter", *International Journal of Optomechatronics*, Vol. 9, No. 3, pp. 195–210,

2015.

9. Méndez, D., S. Méndez, A. Quezada, H. Rudolph and M. Lehman, "Face recognition system using fringe projection and moiré: characterization with fractal parameters", *International Journal of Computer Science and Network Security*, Vol. 9, No. 7, pp. 78–84, 2009.

10. En, B., D. Fa-jie, L. Chang-rong, F. Fan and F. Xiao, "A surface profile reconstruction system using sinusoidal phase-modulating interferometry and fiber-optic fringe projection", *Optical Fiber Technology*, Vol. 20, No. 3, pp. 294–298, 2014.

11. Tkaczyk, T., R. JoˆA *et al.*, "Influence of optical imaging on phase measurements in fringe projection coherent systems", *Optical Engineering*, Vol. 41, No. 4, pp. 811–821, 2002.

12. Pennington, T. L., H. Xiao, R. May and A. Wang, "Miniaturized 3-D surface profilometer using a fiber optic coupler", *Optics & Laser Technology*, Vol. 33, No. 5, pp. 313–320, 2001.

13. Valera, J., D. Harvey and J. Jones, "Fibre optic electronic speckle pattern interferometry: path length stabilised automatic phase stepping", *Holographic Systems, Components and Applications, 1991., Third International Conference on*, pp. 180–184, IET, 1991.

14. Bulut, K. and M. N. Inci, "Three-dimensional optical profilometry using a four-core optical fibre", *Optics & Laser Technology*, Vol. 37, No. 6, pp. 463–469, 2005.

15. Escamilla, G. A. P., F. Kobayashi and Y. Otani, "Three-dimensional surface measurement based on the projected defocused pattern technique using imaging fiber optics", *Optics Communications*, Vol. 390, pp. 57–60, 2017.

16. Dupont, E., F. Lamarque, C. Prelle, T. Redarce *et al.*, "Tri-dimensional optical inspection based on flexible image guide: first step toward 3d industrial en-

doscopy", *Proc. of the 11th Biennial Conference on Engineering Systems Design and Analysis*, Vol. 19, 2012.

17. Chen, L. and C. Huang, "Miniaturized 3D surface profilometer using digital fringe projection", *Measurement Science and Technology*, Vol. 16, No. 5, p. 1061, 2005.

18. Park, H.-S., C. Shah and R. Shah, "An Enhanced Development of 3D Intra-Oral Scanner Using Fringe-Projection Technique for Dentistry", *ASME 2016 International Mechanical Engineering Congress and Exposition*, p. V002T02A036, American Society of Mechanical Engineers, 2016.

19. Cui, H., N. Dai, W. Liao and X. Cheng, "Intraoral 3D optical measurement system for tooth restoration", *Optik-International Journal for Light and Electron Optics*, Vol. 124, No. 12, pp. 1142–1147, 2013.

20. Berryman, F., P. Pynsent, J. Fairbank and S. Disney, "A new system for measuring three-dimensional back shape in scoliosis", *European Spine Journal*, Vol. 17, No. 5, pp. 663–672, 2008.

21. Zawieska, D., "Topography of surface and spinal deformity", *International Archives of Photogrammetry and Remote Sensing*, Vol. 33, No. B5/2; PART 5, pp. 937–942, 2000.

22. Méndez, D., S. Méndez, A. Quezada, H. Rudolph and M. Lehman, "Face recognition system using fringe projection and moiré: characterization with fractal parameters", *International Journal of Computer Science and Network Security*, Vol. 9, No. 7, pp. 78–84, 2009.

23. Guo, H. and P. Huang, "Face recognition based on fringe pattern analysis", *Optical Engineering*, Vol. 49, No. 3, pp. 037201–037201, 2010.

24. Laloš, J., M. Mrak, U. Pavlovčič and M. Jezeršek, "Handheld optical system for skin topography measurement using Fourier transform profilometry", *Strojniški*

vestnik-Journal of Mechanical Engineering, Vol. 61, No. 5, pp. 285–291, 2015.

25. Lagarde, J., C. Rouvrais, D. Black, S. Diridollou and Y. Gall, “Skin topography measurement by interference fringe projection: a technical validation”, *Skin Research and Technology*, Vol. 7, No. 2, pp. 112–121, 2001.

26. Jiang, C., S. Jia, Y. Xu, Q. Bao, J. Dong and Q. Lian, “The application of multi-frequency fringe projection profilometry on the measurement of biological tissues”, *Bio-medical materials and engineering*, Vol. 26, No. s1, pp. S395–S403, 2015.

27. Quan, C., C. Tay, X. He, X. Kang and H. Shang, “Microscopic surface contouring by fringe projection method”, *Optics & Laser Technology*, Vol. 34, No. 7, pp. 547–552, 2002.

28. Kim, H., H. Jung, D.-H. Lee, K. B. Lee and H. Jeon, “Period-chirped gratings fabricated by laser interference lithography with a concave Lloyds mirror”, *Applied optics*, Vol. 55, No. 2, pp. 354–359, 2016.

29. Wachulak, P., M. Capeluto, M. Marconi, C. Menoni and J. Rocca, “Patterning of nano-scale arrays by table-top extreme ultraviolet laser interferometric lithography”, *Optics Express*, Vol. 15, No. 6, pp. 3465–3469, 2007.

30. Chang, E.-C., Y.-L. Sun, P.-T. Lin, D. G. Mikolas and C.-C. Fu, “Lloyd’s mirror interference lithography using a single mode fiber spatial filter”, *Sensors, 2012 IEEE*, pp. 1–4, IEEE, 2012.

31. Wang, Y., S. Zhang and J. H. Oliver, “3D shape measurement technique for multiple rapidly moving objects”, *Optics express*, Vol. 19, No. 9, pp. 8539–8545, 2011.

32. Zappa, E. and G. Busca, “Static and dynamic features of Fourier transform profilometry: A review”, *Optics and Lasers in Engineering*, Vol. 50, No. 8, pp.

1140–1151, 2012.

33. Zuo, C., Q. Chen, G. Gu, S. Feng, F. Feng, R. Li and G. Shen, “High-speed three-dimensional shape measurement for dynamic scenes using bi-frequency tripolar pulse-width-modulation fringe projection”, *Optics and Lasers in Engineering*, Vol. 51, No. 8, pp. 953–960, 2013.

34. Zhang, Y., J. Y. Hu, J. L. Li, H. Q. Wang *et al.*, “The application of WTP in 3-D reconstruction of train wheel surface and tread defect”, *Optik-International Journal for Light and Electron Optics*, Vol. 131, pp. 749–753, 2017.

35. Zhang, Q.-C. and X.-Y. Su, “An optical measurement of vortex shape at a free surface”, *Optics & Laser Technology*, Vol. 34, No. 2, pp. 107–113, 2002.

36. Cobelli, P. J., A. Maurel, V. Pagneux and P. Petitjeans, “Global measurement of water waves by Fourier transform profilometry”, *Experiments in fluids*, Vol. 46, No. 6, pp. 1037–1047, 2009.

37. Cochard, S. and C. Ancey, “Tracking the free surface of time-dependent flows: image processing for the dam-break problem”, *Experiments in Fluids*, Vol. 44, No. 1, pp. 59–71, 2008.

38. Sansoni, G., M. Trebeschi and F. Docchio, “State-of-the-art and applications of 3D imaging sensors in industry, cultural heritage, medicine, and criminal investigation”, *Sensors*, Vol. 9, No. 1, pp. 568–601, 2009.

39. Moring, I., H. Ailisto, V. Koivunen and R. Myllylä, “Active 3-D vision system for automatic model-based shape inspection”, *Optics and lasers in engineering*, Vol. 10, No. 3-4, pp. 149–160, 1989.

40. Giesko, T., A. Zbrowski and P. Czajka, “Laser profilometers for surface inspection and profile measurement”, *Problemy Eksploatacji*, pp. 97–108, 2007.

41. Wester-Ebbinghaus, W., “Analytics in non-topographic Photogrammetry”, *ISPRS-Congress, Com. V, Kyoto*, Vol. 27, p. B11, 1988.

42. Chen, F., G. M. Brown and M. Song, “Overview of three-dimensional shape measurement using optical methods”, *Optical Engineering*, Vol. 39, No. 1, pp. 10–22, 2000.

43. Li, G. K., F. Gao and Z. G. Wang, “A photogrammetry-based system for 3D surface reconstruction of prosthetics and orthotics”, *Engineering in Medicine and Biology Society, EMBC, 2011 Annual International Conference of the IEEE*, pp. 8459–8462, IEEE, 2011.

44. Liu, W., Y. Cheung, P. Sabouri, T. J. Arai, A. Sawant and D. Ruan, “A continuous surface reconstruction method on point cloud captured from a 3D surface photogrammetry system”, *Medical physics*, Vol. 42, No. 11, pp. 6564–6571, 2015.

45. Liu, Z., X. Li, F. Li and G. Zhang, “Flexible dynamic measurement method of three-dimensional surface profilometry based on multiple vision sensors”, *Optics express*, Vol. 23, No. 1, pp. 384–400, 2015.

46. Walker, C. A., “A historical review of moiré interferometry”, *Experimental mechanics*, Vol. 34, No. 4, pp. 281–299, 1994.

47. Creath, K. and J. Wyant, “Moiré and fringe projection techniques”, *Optical shop testing*, Vol. 2, pp. 653–685, 1992.

48. Czarnek, R., “Three-mirror, four-beam Moiré interferometer and its capabilities”, *Optics and Lasers in Engineering*, Vol. 15, No. 2, pp. 93–101, 1991.

49. Kim, S., Y. Choi, J. Oh and M. Jung, “Phase-shifting grating projection moire topography”, *Transactions of the Korean Society of mechanical engineers (in Korean)*, Vol. 22, No. 4, pp. 850–857, 1998.

50. Hariharan, P., *Basics of interferometry*, Academic Press, 2010.

51. Lai, C.-C. and I.-J. Hsu, “Surface profilometry with composite interferometer”, *Optics express*, Vol. 15, No. 21, pp. 13949–13956, 2007.

52. Suzuki, T., M. Shirai and O. Sasaki, “Phase-shifting laser diode Sagnac interferometer for surface profile measurement”, *Proceedings of SPIE-The International Society for Optical Engineering (2007)*, Vol. 6829, p. 68290A, 2007.

53. Abdelsalam, D. G. and B. Yao, “Interferometry and its Applications in Surface Metrology”, *Optical Interferometry*, InTech, 2017.

54. Abdelsalam, D., B. J. Baek, F. Abdel-Aziz, W. Chegal and D. Kim, “Highly accurate film thickness measurement based on automatic fringe analysis”, *Optik-International Journal for Light and Electron Optics*, Vol. 123, No. 16, pp. 1444–1449, 2012.

55. Lin, S.-T., S.-L. Yeh, Y.-C. Wang and M.-Z. Chen, “Laser profilometer using a Fabry–Perot etalon and an objective”, *Sensors and Actuators A: Physical*, Vol. 203, pp. 47–51, 2013.

56. Geng, J., “Structured-light 3D surface imaging: a tutorial”, *Advances in Optics and Photonics*, Vol. 3, No. 2, pp. 128–160, 2011.

57. Baker, M. J., J. F. Chicharo, J. Xi and E. Li, “Accuracy limitations introduced by digital projection sources in profilometric optical metrology systems”, *Optoelectronic and Microelectronic Materials and Devices, 2004 Conference on*, pp. 261–264, IEEE, 2004.

58. Jia, P., J. Kofman and C. English, “Error compensation in two-step triangular-pattern phase-shifting profilometry”, *Optics and Lasers in Engineering*, Vol. 46, No. 4, pp. 311–320, 2008.

59. Fang, Q. and S. Zheng, “Linearly coded profilometry”, *Applied optics*, Vol. 36, No. 11, pp. 2401–2407, 1997.

60. Chen, L., C. Quan, C. J. Tay and Y. Fu, “Shape measurement using one frame projected sawtooth fringe pattern”, *Optics communications*, Vol. 246, No. 4, pp. 275–284, 2005.

61. Lu, C. and L. Xiang, “Optimal intensity-modulation projection technique for three-dimensional shape measurement”, *Applied optics*, Vol. 42, No. 23, pp. 4649–4657, 2003.

62. Gorthi, S. S. and P. Rastogi, “Fringe projection techniques: whither we are?”, *Optics and lasers in engineering*, Vol. 48, No. IMAC-REVIEW-2009-001, pp. 133–140, 2010.

63. Naci nci, M. and K. Bulut, “Fourier transform profilometry with a four-core optical fibre”, *Proceedings of SPIE, the International Society for Optical Engineering*, pp. 643–646, Society of Photo-Optical Instrumentation Engineers, 2005.

64. Duan, F.-j., C. Zhang, C. Zhang and H. Xiao, “Fourier transform profilometry based on fiber-optic interferometric projection”, *Image and Signal Processing, 2009. CISP’09. 2nd International Congress on*, pp. 1–5, IEEE, 2009.

65. Yuan, L., J. Yang, C. Guan, Q. Dai and F. Tian, “Three-core fiber-based shape-sensing application”, *Optics letters*, Vol. 33, No. 6, pp. 578–580, 2008.

66. Lloyd, H., “On a new case of interference of the rays of light”, *The Transactions of the Royal Irish Academy*, pp. 171–177, 1831.

67. Kim, J., I. G. Jeong, S. H. Lee, K. T. Kang and S. H. Lee, “Fabrication of large-area periodic nanostructures using two-mirror laser interference lithography”, *Electronic Materials Letters*, Vol. 9, No. 6, pp. 879–882, 2013.

68. Wathuthanthri, I., W. Mao and C.-H. Choi, "Two degrees-of-freedom Lloyd–mirror interferometer for superior pattern coverage area", *Optics letters*, Vol. 36, No. 9, pp. 1593–1595, 2011.

69. Li, X., W. Gao, Y. Shimizu and S. Ito, "A two-axis Lloyd's mirror interferometer for fabrication of two-dimensional diffraction gratings", *CIRP Annals-Manufacturing Technology*, Vol. 63, No. 1, pp. 461–464, 2014.

70. Korre, H., C. P. Fucetola, J. A. Johnson and K. K. Berggren, "Development of a simple, compact, low-cost interference lithography system", *Journal of Vacuum Science & Technology B, Nanotechnology and Microelectronics: Materials, Processing, Measurement, and Phenomena*, Vol. 28, No. 6, pp. C6Q20–C6Q24, 2010.

71. Liu, Y., *Accuracy improvement of 3D measurement using digital fringe projection*, Master's Thesis, University of Wollongong, 2011.

72. Van der Jeught, S. and J. J. Dirckx, "Real-time structured light profilometry: a review", *Optics and lasers in engineering.-Barking*, pp. 1–31, 2016.

73. Qu, G., C. Huang, Y. Fu, B. Qian and F. Wang, "3D shape measurement method based on the triangle pattern", *Selected Papers of the Chinese Society for Optical Engineering Conferences held October and November 2016*, pp. 102550Q–102550Q, International Society for Optics and Photonics, 2017.

74. Ma, S., C. Quan, C. J. Tay, R. Zhu and B. Li, "Phase error correction for digital fringe projection profilometry", *Physics Procedia*, Vol. 19, pp. 227–232, 2011.

75. Gåsvik, K. J., *Optical metrology*, John Wiley & Sons, 2003.

76. Takeda, M., H. Ina and S. Kobayashi, "Fourier-transform method of fringe-pattern analysis for computer-based topography and interferometry", *JosA*, Vol. 72, No. 1, pp. 156–160, 1982.

77. Takeda, M. and K. Mutoh, “Fourier transform profilometry for the automatic measurement of 3-D object shapes”, *Applied optics*, Vol. 22, No. 24, pp. 3977–3982, 1983.

78. Carlos, P. O. J., G. H. Efren, A. F. M. Antonio, S. O. Artemio, R. A. J. Manuel, T. A. Saul and V. S. J. Emilio, “Three Dimensional Reconstruction Strategies Using a Profilometrical Approach based on Fourier Transform”, *Fourier Transforms-Approach to Scientific Principles*, InTech, 2011.

79. Lally, E. M., *Fourier transform interferometry for 3D mapping of rough and discontinuous surfaces*, Ph.D. Thesis, 2010.

80. Abdul-Rahman, H., *Three-dimensional Fourier fringe analysis and phase unwrapping*, Ph.D. Thesis, Liverpool John Moores University, 2007.

81. Lin, J. F. and X. Y. Su, “Two-dimensional Fourier transform profilometry for the automatic measurement of three-dimensional object shapes”, *Opt. Eng*, Vol. 34, No. 11, pp. 3297–3302, 1995.

82. Kart, T., G. Kösoğlu, H. Yüksel and M. N. İnci, “Fourier transform optical profilometry using fiber optic Lloyds mirrors”, *Applied optics*, Vol. 53, No. 35, pp. 8175–8181, 2014.

83. Hovorov, V., *A new method for the measurement of large objects using a moving sensor*, Ph.D. Thesis, Liverpool John Moores University, 2008.

84. Romaniuk, R. and J. Dorosz, “Temperature sensor based on double core optical fibre”, *Proc. SPIE*, Vol. 4887, pp. 55–66, 2002.

85. Novák, J., P. Novák and A. Mikš, “Multi-step phase-shifting algorithms insensitive to linear phase shift errors”, *Optics Communications*, Vol. 281, No. 21, pp. 5302–5309, 2008.

86. Novak, J., “Five-step phase-shifting algorithms with unknown values of phase shift”, *Optik-International Journal for Light and Electron Optics*, Vol. 114, No. 2, pp. 63–68, 2003.

87. Takahashi, T., Y. Ishii and R. Onodera, “Phase-shifting interferometric profilometry with a wavelength-tunable diode source”, *Optical Review*, Vol. 21, No. 3, pp. 410–414, 2014.

88. Abdelsalam, D., B. Yao, P. Gao, J. Min and R. Guo, “Single-shot parallel four-step phase shifting using on-axis Fizeau interferometry”, *Applied optics*, Vol. 51, No. 20, pp. 4891–4895, 2012.

89. Fan, J., X. Lu, X. Xu and L. Zhong, “Simultaneous multi-wavelength phase-shifting interferometry based on principal component analysis with a color CMOS”, *Journal of Optics*, Vol. 18, No. 5, p. 055703, 2016.

90. Xing, S., P. Chen and Y. Xiao, “Single-shot color fringe projection profilometry using two-step phase shifting and centerline marker”, *Fifth International Conference on Optical and Photonics Engineering*, pp. 1044922–1044922, International Society for Optics and Photonics, 2017.

91. Lewis, A. J., “Absolute length measurement using multiple-wavelength phase-stepping interferometry”, *Doktora Tezi*, 1993.

92. Novack, A., D. DAnnunzio, E. D. Çubuk, N. Inci and L. Molter, “Three-dimensional phase step profilometry with a multicore optical fiber”, *Applied optics*, Vol. 51, No. 8, pp. 1045–1048, 2012.

93. Deng, J., K. Wang, D. Wu, X. Lv, C. Li, J. Hao, J. Qin and W. Chen, “Advanced principal component analysis method for phase reconstruction”, *Optics express*, Vol. 23, No. 9, pp. 12222–12231, 2015.

94. Wang, H., C. Luo, L. Zhong, S. Ma and X. Lu, “Phase retrieval approach based

on the normalized difference maps induced by three interferograms with unknown phase shifts", *Optics express*, Vol. 22, No. 5, pp. 5147–5154, 2014.

95. Daubechies, I., *Ten Lectures on Wavelets*, Society for Industrial and Applied Mathematics, 1992.

96. Jiang, C., S. Jia, J. Dong, Q. Lian and D. Li, "Multi-frequency fringe projection profilometry based on wavelet transform", *Optics express*, Vol. 24, No. 11, pp. 11323–11333, 2016.

97. Kijewski-Correa, T. and A. Kareem, "Efficacy of Hilbert and wavelet transforms for time-frequency analysis", *Journal of engineering mechanics*, Vol. 132, No. 10, pp. 1037–1049, 2006.

98. Li, S., X. Su and W. Chen, "Wavelet ridge techniques in optical fringe pattern analysis", *Journal of Optical Society of America A*, Vol. 27, No. 6, pp. 1245–1254, 2010.

99. Farge, M., "Wavelet transforms and their applications to turbulence", *Annual review of fluid mechanics*, Vol. 24, No. 1, pp. 395–458, 1992.

100. Inanc, A., *3-D Optical profilometry at micron scale with modified fiber optic Lloyd's mirror technique*, Master's Thesis, Bogazici University, 2017.

101. Addison, P. S., "Wavelet transforms and the ECG: a review", *Physiological measurement*, Vol. 26, No. 5, p. R155, 2005.

102. Chew, W. C. and W. C. Chew, *Waves and fields in inhomogeneous media*, Vol. 522, IEEE press New York, 1995.

103. Jacques, L., A. Coron, P. Vandergheynst and A. Rivoldini, "*The YAWTb toolbox: Yet another wavelet toolbox*, 2007", `http://rhea.tele.ucl.ac.be/yawtb`, accessed at October 2017.

104. Gdeisat, M. A., A. Abid, D. R. Burton, M. J. Lalor, F. Lilley, C. Moore and M. Qudeisat, “Spatial and temporal carrier fringe pattern demodulation using the one-dimensional continuous wavelet transform: recent progress, challenges, and suggested developments”, *Optics and Lasers in Engineering*, Vol. 47, No. 12, pp. 1348–1361, 2009.

105. Luong, B., “Costantini phase unwrapping - File Exchange - MATLAB Central,2009”, Accessed at June 2017.

106. Kasim, F., M, “2D Weighted Phase Unwrapping - File Exchange - MATLAB Central, 2016”, Accessed at June 2017.

107. Lee, C.-L., “Self-Interference Lloyd’s Fiber Interferometer”, *CLEO:2011 - Laser Applications to Photonic Applications*, p. JWA37, Optical Society of America, 2011.

108. van Rijn, C. J. M., W. Nijdam, S. Kuiper, G. J. Veldhuis, H. van Wolferen and M. Elwenspoek, “Microsieves made with laser interference lithography for microfiltration applications”, *Journal of Micromechanics and Microengineering*, Vol. 9, No. 2, p. 170, 1999.

109. Choi, C.-H. and C.-J. Kim, “Fabrication of a dense array of tall nanostructures over a large sample area with sidewall profile and tip sharpness control”, *Nanotechnology*, Vol. 17, No. 21, p. 5326, 2006.

110. Wathuthanthri, I., W. Mao and C.-H. Choi, “Two degrees-of-freedom Lloyd–mirror interferometer for superior pattern coverage area”, *Opt. Lett.*, Vol. 36, No. 9, pp. 1593–1595, May 2011.

111. Kim, J., I. G. Jeong, S. H. Lee, K. T. Kang and S. H. Lee, “Fabrication of large-area periodic nanostructures using two-mirror laser interference lithography”, *Electronic Materials Letters*, Vol. 9, No. 6, pp. 879–882, Nov 2013.